

Towards Faster and More Precise MR Spectroscopy at 7 T

Dissertation

zur Erlangung des akademischen Grades

Doktoringenieurin

(Dr.-Ing.)

von

M. Sc. Layla Tabea Riemann

geboren am 28. Juli 1994 in Berlin, Deutschland

genehmigt durch die Fakultät Elektro- und Informationstechnik
der Otto-von-Guericke-Universität Magdeburg

Gutachter:

Prof. Georg Rose

Prof. Oliver Speck

Prof. Itamar Ronen

Einreichung am 15. September 2022

Promotionskolloquium am 23. März 2023

Contents

Abstract	I
Zusammenfassung	III
List of Publications	V
List of Figures	VIII
List of Tables	IX
Acronyms	XI
1 Introduction and Theory	1
1.1 Motivation	1
1.2 Basics of MR Spectroscopy and MR Imaging	2
1.2.1 Nuclear Magnetic Resonance Principle	3
1.2.2 Signal Encoding and MR Image Reconstruction	5
1.2.3 Chemical Shift and Chemical Shift Displacement	6
1.2.4 Generation and Properties of MR Spectra	7
1.3 Pulses and Pulse Sequences for MR Spectroscopy	9
1.3.1 Adiabatic Pulses	10
1.3.2 Multi-banded Pulses	11
1.3.3 SPECIAL	12
1.4 Image Reconstruction Techniques	14
1.4.1 SENSE	14
1.4.2 GRAPPA and split-slice GRAPPA	15
1.5 Outline	17
2 Assessment of Measurement Precision in SVS at 7 T: Determining Minimal Detectable Changes of In Vivo Metabolite Concentrations in the Human Brain	19
2.1 Introduction	19
2.2 Methods	21
2.2.1 MR Hardware	21

2.2.2	Inversion Pulse Implementation	22
2.2.3	Phantom Acquisition	23
2.2.4	In Vivo Experiments	23
2.2.5	Spectral Post-Processing	26
2.2.6	Metabolite Quantification	26
2.2.7	Segmentation and Tissue Fraction Correction	27
2.2.8	Statistical Analysis	27
2.3	Results	31
2.3.1	Inversion Pulse Implementation	31
2.3.2	Phantom Acquisition	33
2.3.3	In Vivo Measurements	34
2.3.4	Precision Evaluation	39
2.4	Discussion	42
3	Fourier-based technique to decompose two simultaneously acquired MRS voxels with 2SPECIAL	49
3.1	Introduction	49
3.2	Methods	51
3.2.1	Pulse Design and Sequence Implementation	51
3.2.2	MR Protocol and Data Acquisition	52
3.2.3	vGRAPPA Decomposition	52
3.2.4	SENSE-based decomposition	53
3.2.5	Phantom Experiments	54
3.2.6	In Vivo Acquisition	54
3.2.7	Spectral Post-Processing	55
3.2.8	Leakage Determination	56
3.2.9	Quantification, Segmentation, Concentration Correction	56
3.2.10	Statistical Evaluation	56
3.3	Results	57
3.3.1	Simulations	57
3.3.2	Phantom Acquisition	60
3.3.3	In Vivo Acquisition	60
3.3.4	Influence of Shim Adjustments	61
3.3.5	SVS _{comb} vs. sMVS	62
3.3.6	SVS _{ind} vs. sMVS	64
3.3.7	Comparison of Decomposition Algorithms	66
3.4	Discussion	70
4	Conclusion & Outlook	75

Abstract

In vivo magnetic resonance spectroscopy (MRS) is an important research tool to gain a deeper understanding of the biochemical processes underlying neurodegenerative or psychiatric diseases such as the Alzheimer's disease or depression, respectively. However, it is not yet integrated into the clinical routine as a diagnostic tool since there are still some obstacles to overcome, such as 1) missing estimation of measurement uncertainties, and a lack of understanding of the influence of acquisition parameters on the precision, as well as 2) a difficult and time-consuming application which causes patient discomfort, high costs and limits the possible range of applications, e.g., for functional MRS questions. The focus of this thesis will be to address the two aforementioned challenges.

To tackle the first challenge, different contributions of reproducibility and repeatability on the measurement uncertainty were evaluated by introducing a study design and statistical analysis framework to determine the minimally detectable changes (MDCs) of the investigated brain metabolites. These MDCs were then compared to the commonly used stand-in for measurement uncertainties, the Cramér-Rao lower bounds (CRLBs), which only represent a fraction of the full measurement uncertainty. As an example of a potential influence on the precision by acquisition parameters, the impact of the choice of a specific pulse within the employed sequence was investigated. Details on the determination of the measurement uncertainty and influences thereupon can be found in chapter 2.

In chapter 3, the second challenge was addressed by the extension and thereby acceleration of single-voxel spectroscopy (SVS) to simultaneously obtain the spectroscopic signal of multiple spatially distinct regions by the introduction of the two spin-echo, full intensity acquired localized (2SPECIAL) sequence. To simultaneously acquire two voxels, the multi-band (MB) technique was applied, which allows the simultaneous excitation or inversion of two spatially distinct frequency bands. Here, the results from the investigation on the influence of the choice of the radio-frequency pulse from chapter 2 were utilized, and a pulse was chosen that was shown to not negatively affect the precision of the measurement but provides optimized properties regarding the MB requirements. Part of this challenge is to retrospectively decompose and reassign the

acquired signals to their region of origin. To this end, a new decomposition algorithm – voxel generalized autocalibrating partial parallel acquisition (vGRAPPA) – was introduced and its performance was rigorously compared to a previously existing decomposition algorithm based on the sensitivity encoding (SENSE) technique.

Both parts of this work are important pieces on the way of understanding and overcoming issues to make in vivo brain MRS faster and more precise to ultimately allow the transition of this high potential research tool towards clinical diagnostic application.

Zusammenfassung

Die in vivo-Magnetresonananzspektroskopie (MRS) ist ein wichtiges Forschungsinstrument, um ein tieferes Verständnis der biochemischen Prozesse zu erlangen, die neurodegenerativen oder psychiatrischen Erkrankungen wie Alzheimer oder Depression zugrunde liegen. Sie ist jedoch noch nicht in die klinische Routine als Diagnoseinstrument integriert, da es immernoch einige Hindernisse zu überwinden gilt, wie 1) fehlende Quantifizierung von Messunsicherheiten sowie ein unvollständiges Verständnis des Einflusses von Aufnahmeparametern auf die Präzision, sowie 2) eine schwierige und zeitaufwändige Anwendung, die für die Patient:innen unangenehm ist, hohe Kosten verursacht und den möglichen Anwendungsbereich einschränkt. Das Adressieren der beiden vorgenannten Herausforderungen steht im Mittelpunkt dieser Arbeit.

Um die erste Herausforderung anzugehen, wurden die verschiedenen Beiträge von Reproduzierbarkeit und Wiederholbarkeit zur Messunsicherheit evaluiert, indem ein Studiendesign und ein statistischer Analyserahmen eingeführt wurden, um die minimal nachweisbaren Veränderungen (MDCs¹) der untersuchten Hirnmetaboliten zu bestimmen. Diese MDCs wurden dann mit dem üblicherweise verwendeten Ersatz für die genauen Messunsicherheiten, den *Cramér-Rao lower bounds* (CRLBs), verglichen, die nur einen Teil der gesamten Messunsicherheit darstellen. Als Beispiel für einen möglichen Einfluss auf die Präzision durch Aufnahmeparameter wurde die Auswirkung der Wahl eines bestimmten Pulses innerhalb der verwendeten Sequenz untersucht, während durch verschiedene Wiederholungsmessungen ein Maß für die Reproduzierbarkeit und damit für die Absolutgenauigkeit der Messungen gewonnen wurde. Details dazu sind in Kapitel 2 zu finden.

In Kapitel 3 wurde die zweite Fragestellung durch die Erweiterung und damit Beschleunigung der Einzel-Voxel-Spektroskopie (SVS²) zur gleichzeitigen Erfassung des spektroskopischen Signals mehrerer räumlich getrennter Regionen adressiert. Dazu

¹Englisch: *minimal detectable changes*

²Englisch: *single-voxel spectroscopy*

wurde die *two spin-echo, full intensity acquired localized* (2SPECIAL) Sequenz eingeführt. Zur gleichzeitigen Erfassung von zwei Voxeln wurde die Multibandtechnik (MB) angewandt, die die gleichzeitige Anregung oder Inversion des Signals von zwei räumlich getrennten Frequenzbändern ermöglicht. Hier wurden die Ergebnisse der Untersuchung zum Einfluss der Wahl des Hochfrequenzpulses aus Kapitel 2 verwendet, und es wurde ein Puls gewählt, der nachweislich die Präzision der Messung nicht negativ beeinflusst, aber optimale Eigenschaften hinsichtlich der MB-Anforderungen bietet. Ein Teil dieser Fragestellung besteht darin, die erfassten Signale rückwirkend zu zerlegen und wieder ihrer Ursprungsregion zuzuordnen. Zu diesem Zweck wurde ein neuer Dekompositionsalgorithmus - *voxel generalized autocalibrating partial parallel acquisition* (vGRAPPA) - eingeführt und seine Leistungsfähigkeit mit einem bereits existierenden Dekompositionsalgorithmus verglichen, der auf der Sensitivitätsskodierungstechnik (SENSE³) basiert.

Beide Teile dieser Arbeit sind wichtige Bausteine auf dem Weg zum Verständnis und zur Überwindung von Hürden, um die *in vivo* Gehirn-MRS schneller und präziser zu machen und damit letztendlich den Übergang dieses Forschungsinstruments mit hohem Potential zur klinischen diagnostischen Anwendung zu ermöglichen.

³Englisch: *sensitivity encoding*

List of Publications

- 09/2022 *Simultaneous 2voxel 1H brain MRS at 7T and its limitations; [L.T. Riemann](#), C.S. Aigner, R. Mекle, B. Ittermann, S. Schmitter, A. Fillmer; 13th Annual Berlin Ultrahigh Field Magnetic Resonance Symposium*
- 06/2022 *Fourier-based decomposition for simultaneous two-voxel MRS acquisition with 2SPECIAL; [L.T. Riemann](#), C.S. Aigner, R. Mекle, O. Speck, G. Rose, B. Ittermann, S. Schmitter, A. Fillmer; Magnetic Resonance in Medicine; 10.1002/mrm.29369*
- 05/2022 *Macromolecule modelling for improved metabolite quantification using very short echo time MRS at 3T: The PRaMM model; A. Dell’Orco, [L.T. Riemann](#), S. Aydin, M. Scheel, B. Ittermann, A. Fillmer; Proceedings of the 30th Annual Meeting ISMRM*
- 05/2022 *Impact of the B0 and B1+-adjustments on the in vivo metabolite quantification accuracy of simultaneous 2voxel 1H brain MRS at 7T; [L.T. Riemann](#), C.S. Aigner, R. Mекle, S. Schmitter, B. Ittermann, A. Fillmer; Proceedings of the 30th Annual Meeting ISMRM*
- 11/2021 *Assessment of measurement precision in single-voxel spectroscopy at 7 T: Toward minimal detectable changes of metabolite concentrations in the human brain in vivo; [L.T. Riemann](#), C.S. Aigner, S.L.R. Ellison, R. Brühl, R. Mекle, S. Schmitter, O. Speck, G. Rose, B. Ittermann, A. Fillmer; Magnetic Resonance in Medicine; 10.1002/mrm.29034*
- 07/2021 *B0-Shimming Methodology for Affordable and Compact Low-Field Magnetic Resonance Imaging Magnets; K. Wenzel, H. Alhamwey, T. O’Reilly, [L.T. Riemann](#), B. Silemek, L. Winter; Frontiers in Physics - Medical Physics and Imaging, 10.3389/fphy.2021.704566*
- 05/2021 *Fourier-based decomposition approach for simultaneous acquisition of 1H spectra from two voxels in vivo at short echo times; [L.T. Riemann](#), C.S. Aigner, R. Mекle, S. Schmitter, B. Ittermann, A. Fillmer; Proceedings of the 29th Annual Meeting ISMRM*
- 05/2021 *On the repeatability and reproducibility of SPECIAL-based in-vivo spectroscopy with different adiabatic inversion pulses; [L.T. Riemann](#), C.S. Aigner, R. Mекle, S. Schmitter, B. Ittermann, A. Fillmer; Proceedings of the 29th Annual Meeting ISMRM*

-
- 05/2021 *B0-shimming methodology for affordable, compact, and homogeneous low-field MR magnets*; K. Wenzel, H. Alhamwey, T. O'Reilly, L.T. Riemann, L. Winter; Proceedings of the 29th Annual Meeting ISMRM
- 09/2020 *In-vivo repeatability of SPECIAL-based single-voxel spectroscopy using different adiabatic inversion pulses*; L.T. Riemann, C.S. Aigner, R. Mekanle, S. Schmitter, B. Ittermann, A. Fillmer; 11th Annual Berlin Ultrahigh Field Magnetic Resonance Symposium
- 08/2020 *Adiabatic multiband inversion for simultaneous acquisition of 1H MR spectra from two voxels in-vivo at very short echo times*; L.T. Riemann, C.S. Aigner, R. Brühl, S. Aydin, R. Mekanle, S. Schmitter, B. Ittermann, A. Fillmer; Proceedings of the 28th Annual Meeting ISMRM
- 04/2019 *Influence of beamline and scanning magnets on the magnetic fringe field at a proton PBS nozzle*; S. Gantz, L.T. Riemann, J. Smeets, J. Pawelke, A. Hoffmann; Radiotherapy and Oncology; 10.1016/S0167-8140(19)31441-0

List of Figures

1.1	Example Brain Spectrum	9
1.2	Explanation of the Adiabatic Principle	11
1.3	SPECIAL Sequence Diagram	13
1.4	SENSE Algorithm for Image Reconstruction	15
1.5	GRAPPA Algorithm for Image Reconstruction	16
2.1	7 T MR Scanner and Head Coil	22
2.2	Pulse Sequence, In Vivo Protocol and Post-Process Pipeline	25
2.3	Implementation Adiabatic Inversion Pulses	32
2.4	Phantom Acquisitions Adiabatic Inversion Pulses	33
2.5	Voxel Overlap	34
2.6	Spectra and BA Plots	36
2.7	BA Plots of Concentrations	37
2.8	Metabolite Concentrations, CRLBs, and CVs	38
2.9	R_0 Correlation for High-Concentration Metabolites	39
2.10	Pulse-wise SDs and Correlation between BA, CRLBs and REML	40
3.1	WURST-2SPECIAL Pulse Generation and Sequence Diagram	51
3.2	Explanation of vGRAPPA	53
3.3	Bloch Simulations of the MB WURST Pulse	58
3.4	Bloch Simulations of the MB HS and the MB WURST Pulse	59
3.5	Bloch Simulations of the Differently Optimized MB WURST Pulses	59
3.6	Phantom Acquisition and Leakage	60
3.7	Positioning and Concentrations in the Motor Cortices	61
3.8	Concentrations in the Motor Cortices for Lower-Intensity Metabolites	62
3.9	CRLBs for SVS and Decomposition in the Motor Cortices	63
3.10	CRLBs in the Motor Cortices for Lower-Intensity Metabolites	63
3.11	CRLB's Cutoffs and Performance Measure for all Algorithms	64
3.12	SVS and Decomposed Spectra	65
3.13	In Vivo Leakage over Distance	67
3.14	Phantom Leakage over Distance and Number of ACS	67
3.15	BA Plots for Decomposition	68

3.16 SVS and Decomposition Spectra from ACC/PCC	69
3.17 SVS _{comb} and SVS _{ind} Spectra from ACC/PCC	70

List of Tables

2.1	Explanation of Statistical Measurement Parameters	20
2.2	Explanation of Different SDs	28
2.3	Adiabatic Inversion Pulse Parameters	31
2.4	Spectral Quality Results	34
2.5	Tissue Fractions and Voxel Overlap	35
2.6	Results REML, BA, CRLB Analyses	41
2.7	Minimal Detectable Changes	42
3.1	Order of Spectral Acquisitions for In Vivo Acquisitions	54
3.2	Time Comparison between SVS and both sMVS Approaches	55
3.3	Impact Transients on Leakage	66
3.4	Concentrations in Other Brain Regions	69

Acronyms

(2)/(s)SPECIAL	(two)/(semi-)spin echo, full intensity acquired localized
(f)MRS	(functional) magnetic resonance spectroscopy
(s)LASER	(semi) localization by adiabatic selective refocusing
(t)Cr	(total) creatine
(v)GRAPPA	(voxel) GeneRalized Autocalibrating Partial Parallel Acquisition
1D/2D/3D	one/two/three-dimensional(ly)
ACC/PCC	anterior/posterior cingulate cortex
ACS	auto-calibration signal
Ala	alanine
Asc	ascorbate
Asp	aspartate
BA	Bland-Altman
BW	bandwidth
CRLB	Cramér-Rao lower bound
CS(D)	chemical shift (displacement)
CSF	cerebrospinal fluid
CT	computed tomography
CV	coefficient of variation
FID	free induction decay
FOCI	frequency offset corrected inversion
FOV	field of view
FWHM	full width at half maximum
GABA	γ -aminobutyric acid
Glc	glucose
Gln	glutamine
Glu	glutamate
GM/WM	gray/white matter
GOIA	gradient offset independent adiabaticity
GPC	glycerophosphocholine
GSH	glutathione
HS	hyperbolic secant
Ins	myo-inositol

ISIS	image-selected in vivo spectroscopy
Lac	lactate
MDC	minimal detectable change
MP2RAGE	magnetization prepared two rapid gradient echo
MRI	magnetic resonance imaging
MRSI	magnetic resonance spectroscopic imaging
NAA	N-acetylaspartate
NAAG	N-acetylaspartylglutamate
OVS	outer volume saturation
PE	phosphoethanolamine
PET	positron emission tomography
ppm	parts per million
PRESS	point resolved spectroscopy
REML	restricted maximum likelihood
RF	radio-frequency
SAR	specific absorption rate
SB/MB	single-/multi-banded
Scyllo	scyllo-inositol
SD	standard deviation
SE	spin-echo
SENSE	sensitivity encoding
SMS	simultaneous multislice
sMVS	simultaneous multi-voxel spectroscopy
SNR	signal-to-noise ratio
STEAM	stimulated echo acquisition mode
SVS	single-voxel spectroscopy
Tau	taurine
tCho	total choline
TE/TR/TI	echo/repetition/inversion time
TMS	tetramethylsilane
UHF	ultra-high field
VAPOR	variable power RF pulses with optimized relaxation delays
VERSE	variable-rate selective excitation
VOI	volume of interest
WS	water suppression
WURST	wideband, uniform rate, smooth truncation

1 Introduction and Theory

1.1 Motivation

The technique of magnetic resonance imaging (MRI) underwent huge development steps in the past decades and is now a fundamental part of clinical *in vivo* diagnostics and therapy planning for various diseases in multiple body regions [1, 2]. It provides excellent soft tissue contrast without the need for contrast agents or emitting ionizing radiation as in computed tomography (CT) or positron emission tomography (PET). This gives rise to the opportunity to repeat examinations without a health risk for the subjects – as long as the safety requirements are met – which makes MRI an important tool for studies to investigate the anatomy, functions, or – in case of diseases – dysfunctions, e.g., in the brain.

Another relevant technique, that is based on the same physical principles as MRI, is magnetic resonance spectroscopy (MRS). It allows non-invasively investigating and quantifying various biochemical compounds within a certain tissue environment, e.g., brain metabolites in the brain, and can thus give valuable insights into biochemical processes underlying metabolic alterations. This technique can be applied in two different ways: In single-voxel spectroscopy (SVS), the signal of one small volume is acquired, while in magnetic resonance spectroscopic imaging (MRSI), an extended region can be examined, which, however, comes with the cost of a degraded point spread function. Both MRS techniques are clinically established for the diagnosis and staging of cancer, as the tissue differences are very pronounced [3, 4].

MRS also showed promising results for diseases exhibiting subtle changes in the brain tissue, which are seen in neurodegenerative disorders, such as in Alzheimer's disease [5] or in psychiatric ones, such as schizophrenia [6]. For these diseases, however, MRS is not integrated into a standard clinical routine yet for a multitude of reasons: MRS is an inherently slow technique that additionally requires a lot of adjustment measurements. During an MRS scan, it is technically challenging and in most settings not possible to re-evaluate the patient's position which makes it prone to motion artifacts, especially for non-compliant patients. Furthermore, a small linewidth and a large signal-to-noise ratio (SNR) are required for an accurate

quantification. Higher B_0 field strengths can be applied to increase the SNR, however, this results in a higher technical effort, e.g., in the homogenization of the B_0 field which is mainly responsible for the linewidth. Another class of difficulties is the inaccuracies that are a result of approximations or simplifications utilized to quantify the metabolite concentrations, such as imperfections in the fitting model. But even if the acquisition and quantification work well, it is difficult to determine measurement uncertainties on a single-subject basis due to long measurement times, patient discomfort, and high costs that make repeated measurements on the same patient unfeasible. As a result of the unknown measurement uncertainty and due to the fact that the concentration differences are subtle, the determination of standard values of metabolite concentrations, corrected for the specific population group, is difficult. The missing standard values and measurement uncertainties limit the possibility to use single measurements for diagnostics.

The aim of this thesis is twofold and addresses the aforementioned issues: 1) To establish a model to determine the full measurement uncertainty and to apply it to evaluate the impact of a specific radio-frequency (RF) pulse within a pulse sequence on the quantification precision. 2) To accelerate the acquisition by the simultaneous acquisition of two spatially distant voxels. Both steps aim to provide a contribution toward clinical implementation of this high-potential technique that would ultimately allow to diagnose and ideally treat diseases such as the Alzheimer's disease earlier.

The following theory part aims to provide a short overview of the physical principles and the technical state of the art that is relevant to this thesis. It is split into three parts. Firstly, a general overview of the fundamentals of MRS and a brief explanation of MRI is given. Subsequently, the relevant RF pulses and MRS pulse sequences, on which this work is built, are explained. Then, two image reconstruction techniques are described in more detail as they become relevant for MRS during this thesis. Lastly, an outline for this thesis is presented.

1.2 Basics of MR Spectroscopy and MR Imaging

This section aims to give a short insight into the physical principles relevant to this thesis. It starts with the basic nuclear magnetic resonance principle underlying both MRI, as well as MRS. Then, a very brief introduction to MRI and image reconstruction is given, while the main focus of this section is on explaining the fundamentals of MRS and motivating the need for sophisticated RF pulses and pulse sequences. If not stated differently, the following sections are based on the explanations given in [1].

1.2.1 Nuclear Magnetic Resonance Principle

Human tissue consists of 60-80% of water in which macromolecules and metabolites are suspended. Macromolecules, metabolites, and water possess many protons, as the molecules contain hydrogen. As protons, i.e., hydrogen nuclei, are spin 1/2 particles, they can assume two energetically different states in an external magnetic field and any transitions between these states involve the absorption or emission of electromagnetic radiation. Both MRS, as well as MRI cannot only be performed for hydrogen (^1H) but also for a number of other nuclei, such as phosphorus (^{31}P), helium (^3He), or carbon (^{13}C), among others. Note that throughout the whole thesis, everything is exclusively described for and applied to ^1H .

To acquire MR images or MR spectra, three magnetic fields are required: a static magnetic field B_0 , a rotating RF field B_1^+ , and a gradient field dB_z/dx_i which is along all three spatial directions x_i , G_x , G_y , and G_z . The gradient fields are switched on and off in a particular order and altered in their strength. Note that B_1^+ refers to the “transmit active” component of the RF magnetic field B_1 , i.e., the circular polarization component that rotates in phase with the spin precession, whereas B_1^- refers to the counter-rotating “receive active” B_1 component. Typical field strengths of B_0 range from 0.2 T to 14.1 T for in vivo applications.

When a sample containing protons, e.g., a phantom or a human body, is exposed to B_0 , the proton spins (partially) align with the external magnetic field and a net magnetization \mathbf{M} is induced as the vector sum of the microscopic magnetic moments of the ^1H nuclei. \mathbf{M} is a *macroscopic* quantity made up of a large number of magnetic moments and can thus be described by the concepts of classical physics [7]. The direction of the B_0 field is conventionally denoted as the z -axis. Thus, \mathbf{M} has a longitudinal M_z component, as well as a transverse one, M_{xy} . In thermal equilibrium, M_z assumes a finite value M_0 whose value depends on B_0 , among others, while $M_{xy} = 0$. If \mathbf{M} is displaced out of its equilibrium state by an external injection of energy, i.e., the second magnetic field B_1^+ , \mathbf{M} begins to precess both in the z -direction as well as the xy -plane with the Larmor frequency ω_0 :

$$\omega_0 = \gamma B_0, \quad (1.1)$$

where γ represents the gyromagnetic ratio, which is 42.576 MHz T $^{-1}$ for protons. Additionally to the precession, \mathbf{M} can be tipped out of its z -axis alignment if the B_1^+ field is applied perpendicular to B_0 and if it rotates near ω_0 . Under the action of an RF pulse, the motion of \mathbf{M} is a superposition of its fast precession around B_0 and the much slower, perpendicular precession around B_1^+ , if observed in a co-rotating coordinate system. If \mathbf{M} is tipped out of the equilibrium towards the xy -plane by a

$\leq 90^\circ$ RF pulse, it is called excitation, if it is tipped towards $-z$ by a 180° RF pulse, it is called inversion.

After the excitation or inversion, \mathbf{M} returns to thermal equilibrium - its initial condition - by relaxation processes. There are two main components of the relaxation which are described by their relaxation times: Firstly, longitudinal relaxation, T_1 , where $M_z(t)$, which was flipped either towards the xy -plane or inverted by 180° , returns to the lower energy state M_0 :

$$M_z(t) = M_0 \cdot (1 - \exp(-t/T_1)). \quad (1.2)$$

T_1 relaxation thus requires the exchange of energy between the spin system and its external environment. If \mathbf{M} is tipped towards the xy -plane, a macroscopic transversal magnetization vector M_{xy} (with $|M_{xy}| \leq M_0$) is created. This can be visualized as a phase-coherent precession of a bundle of aligned spins around B_0 . Over time, this phase coherence is destroyed by interactions within the spins or, again, with the environment. This is described by the transversal relaxation, T_2 :

$$M_{xy}(t) = M_0 \cdot \exp(-t/T_2). \quad (1.3)$$

Microscopically, a “ T_2 process”, i.e., an interaction leading to transversal relaxation, changes the phase of a given spin but not its energy, while a “ T_1 process” always changes energy and phase. Any “ T_1 process” induces both longitudinal and transversal relaxation. Consequently, T_1 can never be shorter than T_2 , for a given system. It should be noted that there are several chemical and physical mechanisms on an inter- and intramolecular level that contribute to T_1 and T_2 relaxation but are not explained in further detail here.

In addition to T_2 relaxation, there is T_2^* relaxation which includes both the actual T_2 , as well as the loss of phase coherence caused by inhomogeneities of the main magnetic field B_0 , $T_{2,\text{inh}}$:

$$\frac{1}{T_2^*} = \frac{1}{T_2} + \frac{1}{T_{2,\text{inh}}}. \quad (1.4)$$

T_2^* thus reflects the observed signal decay in the xy -plane and is always shorter than T_2 ⁴. The different relaxation processes represent the main contrast mechanisms of

⁴It should be noted that the loss of phase coherence caused by locally different precession frequencies is in principle reversible and therefore not relaxation in the thermodynamical sense. Therefore, $T_{2,\text{inh}}$ and T_2^* should be called de-coherence times. In this work, the notion of “ T_2^* relaxation” is adopted, however, as it is commonly done in the MR community.

MRI. The choice of the acquisition times (repetition time (TR) and echo time (TE)) determines which relaxation process is more pronounced.

1.2.2 Signal Encoding and MR Image Reconstruction

As stated in section 1.2.1, the MR signal is obtained as a response to externally applied RF pulses. To acquire information about how the magnetization is distributed in the body, the MR signal is encoded spatially. Therefore, the aforementioned third type of magnetic field is required: field gradients along all three spatial directions, which conventionally increase linearly to locally change the Larmor frequency. If an RF pulse is then applied, only protons at a certain position are affected. For a two-dimensional (2D) sequence, the slice is selected by the first gradient in one direction and the slice thickness is determined by the bandwidth of the RF pulse and the steepness of the gradient.

Then, the spatial localization is typically completed by a frequency and a phase encoding gradient, whereas one frequency and two phase encoding gradients are applied if a 3D sequence is used. For frequency encoding, a gradient, e.g., in x -direction, G_x , forces the spins, dependent on their position x , to precess at different frequencies:

$$\omega(x) = \gamma(B_0 + xG_x). \quad (1.5)$$

Hence, the MR signal does not only consist of one Larmor frequency but of a frequency spectrum. After the excitation, a phase encoding gradient, e.g., in y -direction, G_y , is applied for a time t_{ph} . As the local Larmor frequency is temporarily changed by this gradient, each y -coordinate accrues a different phase offset during t_{ph} . After the gradient has been switched off, a spatially dependent phase angle $\Phi(y)$ remains:

$$\Phi(y) = \gamma y G_y t_{\text{ph}}. \quad (1.6)$$

To generate an image of the scanned object or person, a mathematical construct, called k-space, is used to represent spatial frequencies. Each point in the k-space contains the magnitude and phase of a given 2D or 3D set of spatial frequencies of the object. The periphery of the k-space contains information of high spatial frequencies, i.e., details and edges, while the center of the k-space consists of low spatial frequency information, determining general shapes. The straightforward way to fill the k-space during acquisition is to collect the data line by line to obtain a 2D or 3D grid. A host of other strategies to sample k-space exist, however, providing advantages with regard to motion sensitivity or acquisition acceleration. To derive the real image

information from k-space data, the spatial frequencies are inversely 2D or 3D Fourier transformed. Thus, the k-space and the image space are geometrically connected: The field-of-view (FOV) in the image space is inversely proportional to the k-space resolution, i.e., the distance between two neighboring points, in the same direction; the image resolution is inversely proportional to the extent of covered k-space. As a consequence, the resolution and FOV of an MR image can be manipulated by altering the number of points and their respective spacing and extent spanned in k-space. Note that the here introduced k-space refers to the acquisition k-space, i.e., the k-space in which the resulting image is stored after excitation, as there is also the concept of excitation k-space.

1.2.3 Chemical Shift and Chemical Shift Displacement

As already stated in section 1.2.1, the resonance frequency depends not only on B_0 and the gyromagnetic ratio but also on the molecular environment that impacts the nucleus. Electrons surrounding the nucleus shield it against the external magnetic field by interacting with it and thereby inducing a local magnetic field B_{loc} . This field builds up proportional to the external one but with an opposed orientation (in diamagnetic organic tissue). This leads to a reduced effective field amplitude at the nucleus with a reduction factor characteristic for the locally induced electronic spin density and thus for the chemical environment of a given proton species. The local resonance frequency is then given by:

$$\nu = \frac{\gamma}{2\pi}(B_0 - B_{\text{loc}}). \quad (1.7)$$

To make MRS comparable for all applied external magnetic field strengths, resonance frequencies are reported as a relative shift δ , stated in parts per million (ppm), vs. an arbitrarily chosen reference substance. For protons, the reference substance is conventionally tetramethylsilane (TMS) and the resulting resonance frequency for proton spectroscopy is defined as:

$$\delta = \frac{\nu - \nu_{\text{ref}}}{\nu_{\text{ref}}} \cdot 10^6, \quad (1.8)$$

which is a dimensionless scalar constant for isotopic fluids. For water, it results in a chemical shift of 4.7 ppm.

This CS is of fundamental relevance for MRS since it is the basic prerequisite for separating and identifying the different metabolites from each other. A necessary consequence of this effect, however, is that frequency differences between different

chemical environments at the same location cannot be distinguished from gradient-induced frequency differences between two identical molecules at different locations. As a result, in image reconstruction, different resonance frequencies are erroneously assigned to different locations. This undesired side effect of frequency-based localization techniques is called chemical shift displacement (CSD). It implies that simultaneously acquired signals from metabolites with different resonance frequencies necessarily originate from different volumes. The effect can be minimized by using high-bandwidth RF pulses but cannot be entirely avoided.

In contrast to MR imaging, which was described in section 1.2.2, the localization of the volume of interest (VOI) in single-voxel MRS is conventionally obtained by simultaneously applying an orthogonal, frequency-selective RF pulse and a spatially linear gradient, consecutively in all three spatial directions. The spatial position of the VOI is thus linearly influenced by the average pulse frequency, the gradient, as well as position of the proton of the investigated metabolite molecule, as already stated in Equation (1.5) and (1.7). The difference $\Delta\omega$ in the Larmor frequency of two different metabolites thus results in the spatial shift Δz of the selected slice of the VOI for these metabolites:

$$\Delta z = \frac{\Delta\omega}{\gamma G_z} \propto \frac{\Delta\nu}{\text{BW}} d_z. \quad (1.9)$$

The proportionality is based on the fact that for any given gradient strength the slice of thickness d_z of the selected slice is proportional to the bandwidth BW of the RF pulse, while the CSD Δz is proportional to the frequency separation $\Delta\nu$. Since the absolute frequency shift $\Delta\omega$ is proportional to B_0 , the spatial shift increases with increasing B_0 , given the same slice thickness and BW of the pulse. To maintain both Δz and d_z for different field strengths, it is necessary to adapt the BW, which is usually anti-proportional to the pulse duration. One possibility to decrease the CSD is thus to shorten the pulse duration which, however, requires a proportional increase in B_1^+ to achieve the same flip angle. This then comes at the cost of other limitations, such as reaching the hardware limits of the RF amplifier or exceeding the specific absorption rate (SAR). A way to fix the BW, while not decreasing the flip angle nor reaching hardware limits, is the use of adiabatic pulses, which is described in more detail in section 1.3.1.

1.2.4 Generation and Properties of MR Spectra

Once a VOI is selected and the RF pulses and gradients are applied, half an echo is acquired which has the shape and the mathematical properties of a free induction

decay (FID) signal, i.e., exhibiting a T_2^* envelope decay. Throughout this thesis, this second half of an echo with FID properties will be referred to as FID⁵. The relevant spectroscopic information is obtained by a one-dimensional (1D) Fourier transformation of the FID. The frequency information is then visible, revealing one or multiple spectral peaks, as shown in Figure 1.1. Both the shape of the peaks, as well as their position on the x -axis, i.e., the CS difference, is unique for every metabolite. These fingerprint-like properties of the metabolites enable to fit the individual metabolite spectral signatures mathematically. To obtain the corresponding metabolite concentrations then, firstly, the relative area under the peak is determined as it is approximately proportional to the number of active nuclei in each molecule. Active nuclei chemically equivalent thereby refers to the protons in the molecule that are bound at positions in the molecule. Secondly, the prior result is normalized to the integral of the pure water signal.

It should be noted that not all peaks visible in the spectrum originate from different metabolites. Some metabolites show split peaks, resulting in doublets, triplets, or higher-order multiplets. Some even just have multiple singlets, or singlets and different multiplets. This phenomenon is a consequence of an electron-mediated interaction of two nuclear spins on the same molecule and is known as J-coupling or scalar coupling. In short, the spin of one nucleus polarizes its valence and thus all covalent bonds it is involved in. The polarized bonds then create an additional small magnetic field at the neighboring nucleus. J-coupling interactions are independent of B_0 .

⁵Conventionally, the first half of the echo is not utilized, as this part is usually not symmetrical and affected by the crusher gradients that are used to decrease the impact of spurious signals. Moreover, starting with the echo maximum as first time domain sampling point simplifies the analysis of J-coupled metabolites, as it eliminates the necessity of first-order phase correction.

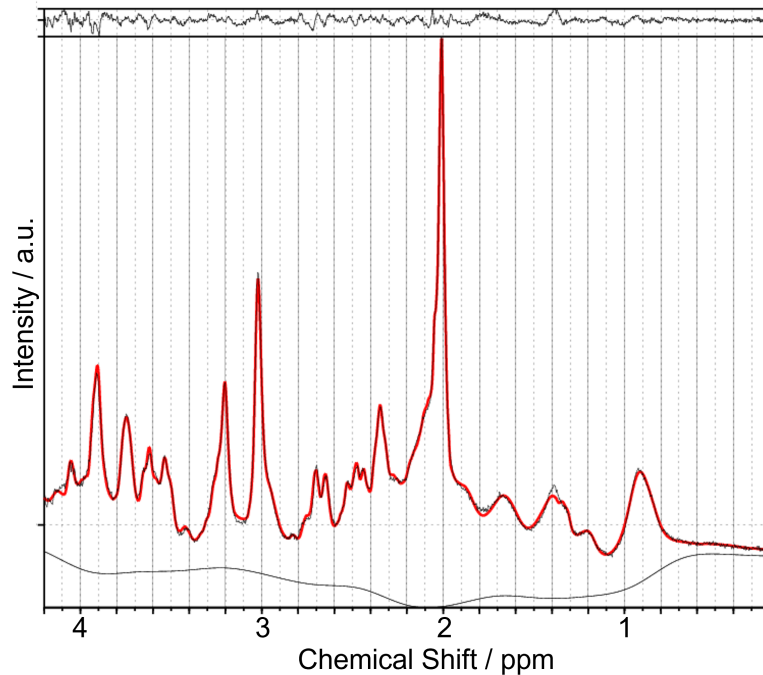


Figure 1.1: Exemplary ^1H brain MR spectrum: The red line indicates the fitted curve for the measured, Fourier transformed spectral signal, which is shown in black. The fit function is composed of basis spectra for each metabolite where each basis spectrum can already contain multiple peaks. Their relationships to each other are fixed as the chemical composition of each metabolite molecule is known. The black thin line under the curve indicates the baseline that remains and cannot be explained by the fit model. The noise signal on the top could also not be fitted. Ideally, it represents only high-frequency noise, in contrast to the low-frequency baseline signal, which is normally assigned to quickly relaxing, and thus spectrally broad, unidentified macromolecules. By convention, the CS axis is plotted from right to left.

1.3 Pulses and Pulse Sequences for MR Spectroscopy

In this section, the state of the art of RF pulses and pulse sequences, which are important for this thesis, is described. Firstly, two different classes of pulses, adiabatic inversion pulses, as well as multi-banded (MB) pulses, are explained. Then, the spin-echo, full intensity acquired localized (SPECIAL) pulse sequence that was utilized, modified, and extended throughout this thesis is presented in the way it was originally introduced. Note that the following explanations focus exclusively on SVS since this MRS technique is the only important one in this work.

1.3.1 Adiabatic Pulses

Adiabatic pulses are a class of RF pulses that can be used for excitation, refocusing or inversion. The common feature for all three applications is that adiabatic pulses are both amplitude- and frequency-modulated pulses that show 1) a high B_1^+ insensitivity, i.e., allow an accurate magnetization over a wide range of RF power levels, and 2) high robustness against B_0 inhomogeneities, as long as their frequency sweep is wide enough. These advantages are a result of the adiabatic principle: The net magnetization \mathbf{M} is altered by a slow sweep of the B_1^+ frequency through the resonance. As a result, adiabatic pulses invert or alter the spins with different resonance frequencies at different times, which makes them different from “conventional” pulses. Another difference in behavior is that the flip angle they produce is not simply proportional to the integral of the pulse duration and B_1^+ magnitude. It depends on how the B_1^+ field changes in frequency and amplitude throughout the pulse.

The physical principles behind adiabatic pulses will be briefly explained in the following paragraph. For a more detailed theory of adiabatic pulses, the reader is referred to Tannús et al. [8]. Note that, in the following, B_0 and B_1^+ describe vectors and are thus depicted in bold letters. If a sample is placed in \mathbf{B}_0 and a 90° pulse is applied, the transverse magnetization starts to precess at ω_0 . To facilitate the understanding of the adiabatic principle, conventionally the rotating frame concept is used, which describes a transformed coordinate system, where the observer rotates with ω_0 , i.e., the motion of the precession around \mathbf{B}_0 is “frozen”. The new “fixed” coordinates are now x' , y' , and z' . Staying in this frame, \mathbf{M} will precess around the direction of an effective magnetic field \mathbf{B}_{eff} . The transverse field \mathbf{B}_1^+ is then applied in a gradual way, where its magnitude can be kept constant but its frequency gradually increases from below resonance ($\omega_1 < \omega_0$) to resonance ($\omega_1 = \omega_0$) and ultimately beyond resonance ($\omega_1 > \omega_0$). If the \mathbf{B}_1^+ field is both strong and slow enough, which is defined by the adiabatic condition, \mathbf{M} gradually follows \mathbf{B}_{eff} during the \mathbf{B}_1^+ frequency sweep, which is called adiabatic following. A more graphical explanation of the adiabatic principle is depicted in Figure 1.2.

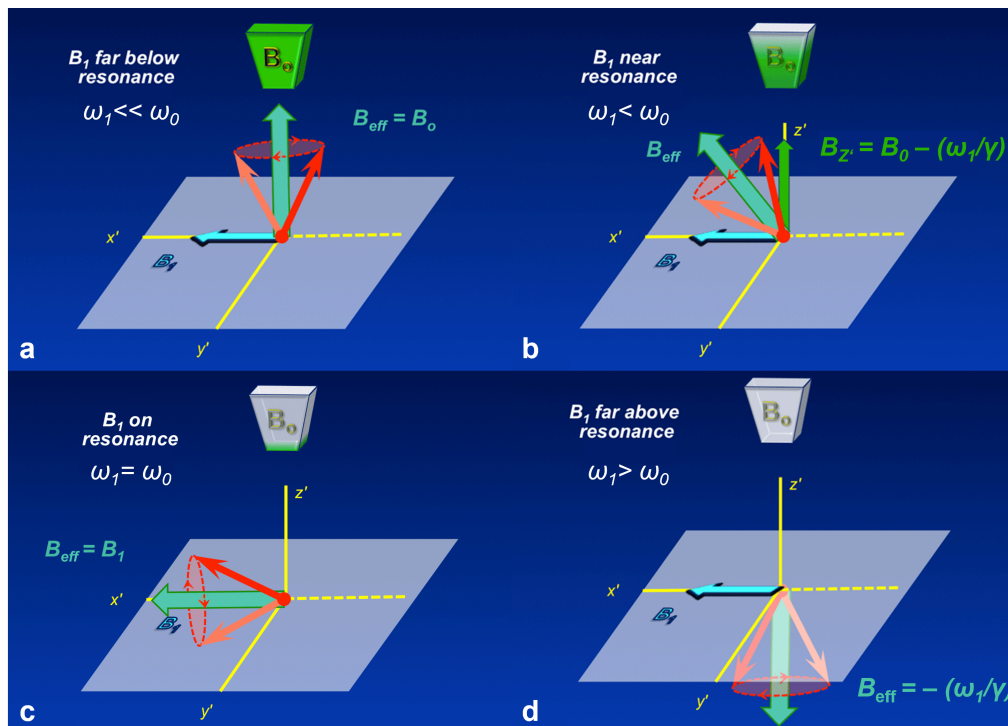


Figure 1.2: *Explanation of the adiabatic principle. a) Starting from far below resonance, $\mathbf{B}_{\text{eff}} = \mathbf{B}_0$; b) With increasing ω_1 , \mathbf{B}_{eff} is the vectorial sum between \mathbf{B}_1^+ and $\mathbf{B}_{z'}$, with $\mathbf{B}_{z'} = \mathbf{B}_0 - (\omega_1/\gamma)$. c) When $\omega_1 = \omega_0$, $\mathbf{B}_{\text{eff}} = \mathbf{B}_1^+$. d) Far above resonance ($\omega_1 \gg \omega_0$), $\mathbf{B}_{\text{eff}} = -(\omega_1/\gamma)$, which is called adiabatic inversion. Note that the red arrows indicate \mathbf{M} precessing around \mathbf{B}_{eff} . Courtesy of Allen D. Elster, *MRIquestions.com* (adapted)*

There are different types of adiabatic fast passage pulses, i.e., pulses producing a 180° flip angle, that can be used for adiabatic inversion. The easiest and most common implementations are pulses with a constant, slice-selective gradient, e.g., the hyperbolic secant (HS) pulse, whereas gradient-modulated pulses, such as the gradient-offset independent adiabaticity (GOIA) or wideband, uniform range, smooth truncation (WURST) pulse, are more complex to implement but provide some advantages, which will be described in more detail in chapter 2.

1.3.2 Multi-banded Pulses

This section aims to provide a general introduction to MB pulses enabling the reader to understand the concept of MB adiabatic pulses, which will be important throughout this thesis. If deeper insights into the general concept of simultaneous multislice (SMS) excitation, reconstruction, and application are requested, the reader is referred to [9], while a detailed description of MB adiabatic pulses can be found in [10].

For certain applications, it can be beneficial to simultaneously excite two or more slices. One way to obtain this SMS excitation is to use MB pulses. To obtain an MB pulse $B_{1,\text{MB}}^+(t)$ that allows to simultaneously invert two slices with an inter-slice distance Δz , two SB pulses $B_{1,\text{SB}}^+(t)$ can be superimposed:

$$B_{1,\text{MB}}^+(t) = B_{1,\text{SB}}^+(t) \cdot (1 + \exp(i\Delta z k(t))), \quad (1.10)$$

where $k(t)$ represents the excitation k-space trajectory. For most common situations, the magnitude of the SB pulse remains unchanged as the same slice profile and flip angle are required for all slices. There are two main technical challenges in the MB RF pulse design: 1) The increased peak amplitude can exceed the capabilities of the RF amplifier as well as the short-term SAR, i.e., the SAR obtained 10 seconds after the application of the RF pulse, and 2) the total applied power of the RF pulse in combination with short TRs can exceed long-term SAR limitations, i.e., the accumulated 6 minutes SAR. Increasing the pulse duration, while fixing the bandwidth-time-product and flip angle to ensure identical slice profiles, reduces both peak amplitude and SAR. However, this time stretching may lead to impaired robustness against off-resonance effects, as well as in prolonged sequence timings, resulting in non-negligible T_2^* effects. A method to simultaneously reduce peak power and SAR is the use of MB gradient-modulated adiabatic pulses, which will be described in chapter 3. More details on the reconstruction of SMS data can be found in section 1.4.

1.3.3 SPECIAL

This section will exclusively describe the SPECIAL sequence which was first introduced by Mlynárik et al. [11] and adapted for human in vivo measurements by Mekle et al. [12].

The sequence is a combination of a 1D image-selected in vivo spectroscopy (ISIS)[13] prior to the excitation, which enables the short TEs, and a slice-selective spin-echo (SE), as illustrated in Figure 1.3. The short TE is possible due to the fact that the first slice inversion occurs before the excitation of transversal magnetization and thus does not contribute to TE, because T_2 relaxation is not yet present. The pulse, that is used for the ISIS add-subtract scheme in the original implementation, is an adiabatic HS inversion pulse ($\text{BW}_{\text{inv}} = 2.1$ kHz, $T_{\text{inv}} = 5.12$ ms), which is applied in alternating scans together with a 180° phase shift in the receive phase. To obtain a 2D localized spin-echo in the other spatial directions, an asymmetric 90° excitation [14] and a 180° Mao refocusing pulse [15] ($\text{BW}_{\text{exc}} = 5.3$ kHz, $T_{\text{exc}} = 1.28$ ms; $\text{BW}_{\text{ref}} = 1.8$ kHz, $T_{\text{ref}} = 3.2$ ms) are used. A 3D outer volume saturation (OVS) to saturate the fat

signal interleaved with a variable power RF pulses with optimized relaxation delays (VAPOR) water suppression (WS) [14] is utilized prior to the actual acquisition, as both signals are several orders of magnitude larger than the metabolite signal and would thus completely overlay it. The OVS bands were individually adjusted for every subject by positioning them 5 mm adjacent to the VOI, ensuring that every part of the subject's head, except the voxel, is fully covered. To destroy any spurious signals, spoiling gradients are applied before and after the 90° excitation pulse, as well as after the 180° refocusing pulse. The spectroscopic signal is acquired after the last spoiling gradient.

Compared to other MRS sequences, e.g., localization by adiabatic selective refocusing (LASER) or point-resolved spectroscopy (PRESS), SPECIAL allows for shorter TEs (< 10 ms) and thus minimizes T_2/T_2^* relaxation and J-coupling effects. In contrast to other short TE sequences, e.g., stimulated echo acquisition mode (STEAM), SPECIAL keeps the full signal intensity [16, 17].

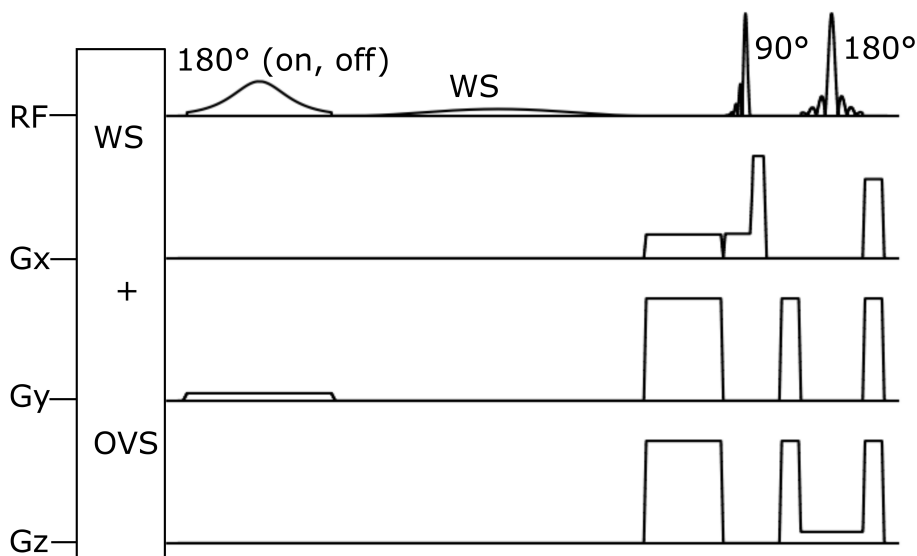


Figure 1.3: Sequence diagram of the SPECIAL sequence. Prior to the actual spectroscopic acquisition, an interleaved OVS and WS scheme is applied. The top panel shows the RF pulses, starting with the HS adiabatic inversion pulse, which is played out in alternating transients. The HS pulse is followed by the asymmetric 90° excitation pulse and the 180° Mao refocusing pulse. Between the inversion and the excitation pulse, there is an additional WS pulse. In the next three rows, the slice selective gradients for each direction, as well as the spoiling gradients are shown. The figure is adapted from [12].

1.4 Image Reconstruction Techniques

This section aims to give a brief overview of the two image reconstruction techniques that were used throughout this thesis. Both techniques were adapted to be applicable to spectroscopic questions but in this part, they are presented as initially introduced for MR imaging. To gain deeper insights into the basic principles of accelerated image reconstruction, especially SMS imaging techniques, the reader is referred to [18, 9].

Both of the presented techniques have in common that they are parallel imaging techniques aiming to accelerate MR imaging by reducing the time-consuming phase encoding steps. A requirement for both techniques is the use of multichannel receiver coils. One single receiver coil arranged in a coil array covers only a limited spatial region and can be characterized by its coil sensitivity map, indicating how sensitive a particular coil element is to a specific point in space. The main idea for the acceleration is that a reduced amount of k-space data is required if an array of receiver coils is used and the spatial information contained in the different coil-element sensitivities is properly exploited. These undersampled data sets are obtained more quickly but result in aliasing, i.e., multiple shifted replicas of the original image overlap in the reconstructed image. To retrospectively obtain the unaliased images from the reduced data, the sensitivity information of the differently located, multiple coils is used to reconstruct the images in the image space. If real-space coil sensitivity maps are utilized for this purpose, this is called sensitivity encoding (SENSE)[19]. If a few additionally acquired k-space lines are acquired to derive this information, this is called generalized autocalibrating partial parallel acquisition (GRAPPA)[20]. The reader is referred to [21] if they are interested in a comparison between the presented and other parallel imaging techniques.

The sensitivity maps have to be individually determined for every subject in the MR scanner as it depends on the tissue distribution in the receiver coil. The individual coils are arranged to form an array such that the coil sensitivity profiles cover the full anticipated FOV.

1.4.1 SENSE

The SENSE algorithm can be divided into four steps: 1) Generation of coil sensitivity maps which is usually done as a low resolution prescan to the actual MR imaging sequence or derived from other imaging data; 2) Acquisition of the undersampled k-space data; 3) Reconstruction of partial FOV images each derived from an individual coil; 4) Combination of the partial FOV images by matrix inversion. Figure 1.4 aims to illustrate the aforementioned four steps of the SENSE algorithm. For a more

profound understanding of the SENSE algorithm, the reader is referred to the original publication by Pruessmann et al. [19].

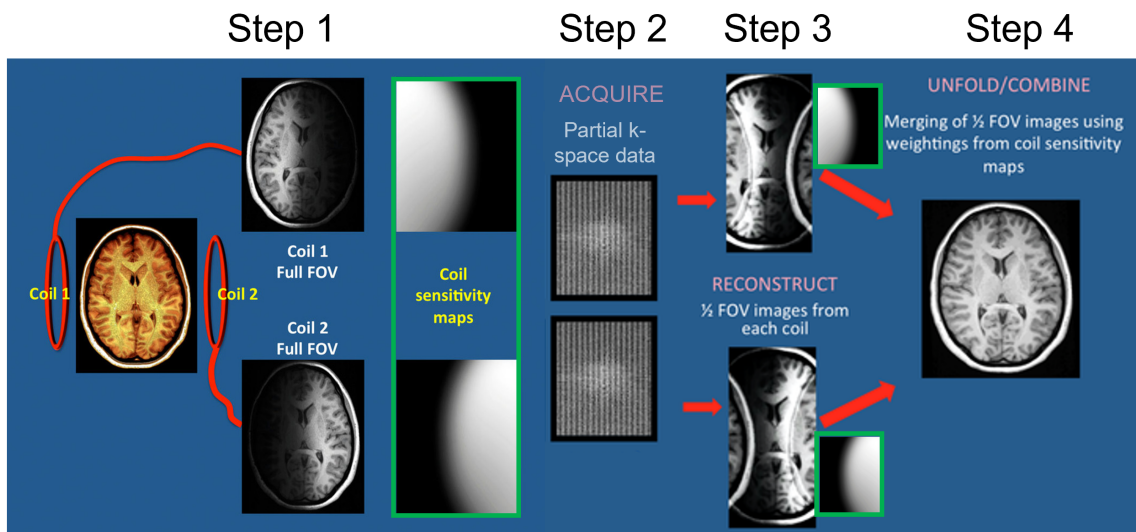


Figure 1.4: *The four steps of the SENSE algorithm to reconstruct aliased images that were obtained by parallel imaging. Coil sensitivities are obtained (step 1), partial k-space data is acquired (step 2), the partial image of each coil is reconstructed (step 3) and lastly the images obtained in step 3 are unfolded utilizing the coil sensitivities determined in step 1 to obtain the image of the full FOV (step 4). Note that the coil sensitivities and the unfolding process are performed in the image space. Courtesy of Allen D. Elster, MRIquestions.com (adapted)*

1.4.2 GRAPPA and split-slice GRAPPA

The GRAPPA algorithm can also be divided into four main steps: 1) Data acquisition: The acquired, undersampled MR signal is utilized to coilwise fill the k-space matrix. Since several phase encoding steps have been omitted, multiple k-space lines are missing. Lines through the k-space center though are fully sampled as they constitute the autocalibration signal (ACS) region. 2) Calculation of the missing k-space lines: The acquired ACSs are utilized to calculate weighting factors for every coil reflecting how each coil smears, distorts, as well as displaces spatial frequencies within the k-space data of the whole FOV. Missing k-space points are then estimated iteratively utilizing these global weighting factors in combination with locally known data for each of the small regions, which are referred to as a block or kernel. Thus, weighting factors, as well as known data from all coils are necessary to determine missing data for every individual coil. 3) Determining individual coil images: As the missing lines are filled, the data is Fourier transformed to obtain the individual images from every coil. In contrast to the coil images in SENSE, the here generated images are already free from aliasing. 4) Lastly, the coil images are combined by applying the sum of

squares method to obtain the final magnitude image. Figure 1.5 aims to illustrate all the steps and the estimation of the missing k-space data.

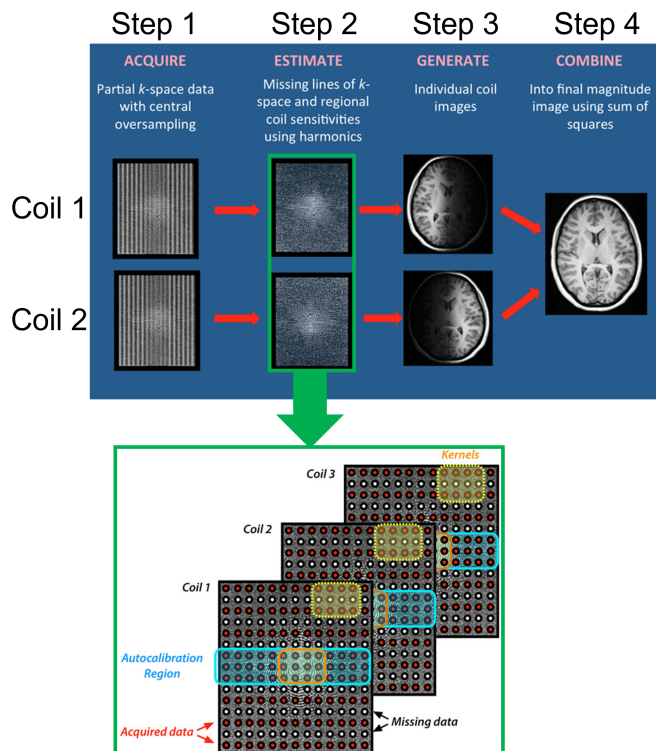


Figure 1.5: The four steps of the GRAPPA algorithm to reconstruct aliased images that were obtained by parallel imaging. Partial k-space data with oversampling in the center are obtained (step 1). The missing k-space lines are estimated by using the fully sampled center (ACS) to calculate coilwise weighing factors (step 2). The individual, aliasing free coil images are obtained (step 3) and lastly, the coil images are combined to obtain the final image (step 4). Steps 1 and 2 are performed in k-space, whereas steps 3 and 4 are done in the image space. Courtesy of Allen D. Elster, *MRIquestions.com* (adapted)

Here, the very basic principle behind slice-GRAPPA and the general idea behind split-slice-GRAPPA are explained. A more detailed and profound description of slice-GRAPPA is found in [22], while for split-slice GRAPPA, the reader is referred to [23, 24, 25]. Both techniques are built on the GRAPPA principle but instead of accelerating the image acquisition through parallel imaging, these techniques aim to increase the temporal efficiency of SMS acquisitions for diffusion-weighted imaging and functional MRI studies. Slice-GRAPPA thereby describes the main concept of unaliasing multiple simultaneously acquired slices, whereas split-slice GRAPPA is an enhancement of the original implementation providing a decreased inter-slice leakage.

In slice-GRAPPA, the image $I(x,y)$ at the location (x,y) from slice z and coil element j can be determined by the product of the true magnetization $\rho_z(x,y)$ and the coil

sensitivities $C_{j,z}(x,y)$ of that slice.

$$\begin{aligned} I_{j,z}(x,y) &= C_{j,z}(x,y) \cdot \rho_z(x,y) \\ &\approx \sum_{\ell=1}^L \left(\sum_{s=1}^S I_{\ell,s}(x,y) \right) K_{\ell,j,z}(x,y), \end{aligned} \quad (1.11)$$

where S describes the total number of SMS slices, L is the number of channels, and $K_{\ell,j,z}(x,y)$ is the kernel. This kernel thereby describes how the aliased image of all SMS slices of each channel has an impact on the individual image of the slice z and coil element j . These fitting parameters can be calculated most efficiently by transforming (1.11) into k-space. The aliased SMS slices can be rewritten by introducing the convolution matrices CM_z for a given z across all channels:

$$I_{j,z} = (CM_1 + CM_2 + \dots + CM_S) \cdot K_{j,z}(x,y). \quad (1.12)$$

Then, an explicit least squared solution of Equation (1.12) can be found to determine the kernels. To save computer memory, the best way is to apply the kernels in k-space which can be done by forming new 2D convolution matrices and then performing the matrix-vector multiplication as shown in Equation (1.12).

The idea behind split-slice GRAPPA is then to robustly optimize the slice-GRAPPA algorithm to ensure accurate image reconstruction by a reduction of leakage artifacts between and within the slices [23].

1.5 Outline

This work is split into two parts. The major aim of the first one is to determine the minimal detectable changes (MDCs) of 13 quantified metabolites for healthy subjects measured with a distinct repetition scheme on a 7 T scanner. Therefore, a nested unbalanced study design and a statistical framework, called restricted maximum likelihood (REML) analysis are presented that allow determining the measurement uncertainties accounting for all possible influences. The derived measurement uncertainties for all metabolites are compared to the conventionally utilized Cramér-Rao Lower Bounds (CRLBs). To apply the study design and statistical framework, the impact of the choice of the adiabatic inversion pulse within the SPECIAL sequence on the repeatability and reproducibility is determined. To that end, the originally implemented inversion pulse - the HS pulse - is replaced by two gradient-modulated pulses, namely the GOIA and the WURST pulse. The first part is adapted from the paper: *Assessment of measurement precision in single-voxel spectroscopy at 7 T: Toward minimal detectable changes of metabolite concentrations in the human*

brain in vivo; [L.T. Riemann](#), C.S. Aigner, S.L.R. Ellison, R. Brühl, R. Mekte, S. Schmitter, O. Speck, G. Rose, B. Ittermann, A. Fillmer; *Magnetic Resonance in Medicine*; 10.1002/mrm.29034 [26].

In the second part, the main goal is to accelerate SVS by the simultaneous acquisition of two spatially distant voxels and the retrospective signal decomposition to their respective regions. This is beneficial for patient comfort and saves costs. Moreover, it allows for answering functional MRS (fMRS) questions, where actual simultaneous acquisitions are the least error-prone. To achieve the acceleration, the SPECIAL sequence was modified to simultaneously acquire the signal of two spatially distinct voxels by multi-banding the inversion pulse that is played out prior to the excitation part. Throughout this work, this modified SPECIAL sequence will be referred to as 2SPECIAL. After the simultaneous acquisition, the signal needs to be disentangled and reallocated to its original spatial region. For this purpose, a decomposition technique, which is known from MR imaging, the split-slice GRAPPA algorithm, was adapted for the given spectroscopic question and will be referred to as voxel-GRAPPA (vGRAPPA). This newly introduced algorithm is then compared to the well-established SENSE-based decomposition, as well as to the SVS acquisitions with identical B_0 and B_1^+ shims for both voxels and, ultimately, to the gold standard, the individually optimized adjustments. The second part is adapted from the paper: *Fourier-based decomposition for simultaneous two-voxel MRS acquisition with 2SPECIAL*; [L.T. Riemann](#), C.S. Aigner, R. Mekte, O. Speck, G. Rose, B. Ittermann, S. Schmitter, A. Fillmer; *Magnetic Resonance in Medicine*; 10.1002/mrm.29369 [27].

Finally, the last chapter concludes the main results of this work and gives an outlook on future research topics to overcome the remaining challenges with respect to a more precise and accelerated MRS acquisition and evaluation.

2 Assessment of Measurement Precision in SVS at 7 T: Determining Minimal Detectable Changes of In Vivo Metabolite Concentrations in the Human Brain

2.1 Introduction

One way to obtain an improved distinction between overlapping metabolites is to use ultra-high field (UHF) strength since it offers an increased SNR and CS dispersion [2], given an adequate B_0 shimming. In contrast to lower field strengths, UHF-MRS has the potential to measure an increased number of metabolites more reliably which would enable an accurate examination of disease-related changes in the metabolite concentration levels. Despite this, so far UHF-MRS remains mainly a research tool focusing on comparisons between control and patient cohorts [28], not providing the option for individual diagnosis. The main reasons are presumably: 1) the ranges of metabolite concentrations of patients overlap substantially with the ones measured in healthy controls, and 2) reliable MRS measurement uncertainties are only available if in vivo acquisitions are repeated several times which is not feasible in a clinical context [29]. Therefore, CRLBs, as described by Cassavila et al. [30, 31], are utilized most of the time to assess the reliability of the measured concentrations.

In other experimental fields, measurement uncertainties can often be determined by comparing own results to a “ground truth” value. More often than not, however, such “ground truth” values are not available. The next best thing is then to repeat a measurement multiple times under identical conditions to learn about its repeatability and precision (but not about its accuracy). For in-vivo MRS, both approaches are not

normally feasible, however. Utilizing phantoms with known metabolite concentrations for repeated measurements has limited potential since they fail to mimic several technical acquisition aspects, as well as the complex interaction between measured concentrations, partial volume effects, tissue structure, and differences in the micro-environment of tissue. Table 2.1 aims to provide a clear distinction between the different terms describing the measurement uncertainty and associated statistical parameters, which are used in the following chapter.

Table 2.1: *Explanation of different statistical parameters describing the measurement uncertainty and associated parameters [32].*

Name	Explanation
Accuracy	Degree of agreement between a reference value and a measured value of a measurand.
Error	Measured value - reference value
Precision	Agreement of measured values or indications obtained by repeated measurements on the same or similar objects under certain conditions.
Repeatability	Measurement precision under the condition that all parameters, including procedure, operator, measuring system, etc., are fixed during the execution of two or more measurements over a short period of time.
Reproducibility	Measurement precision from a range of conditions involving different locations, operators, and measurement systems, and repeated measurements on the same or similar objects.
Uncertainty	Parameter that characterizes the dispersion of the values assigned to a measurand, based on the utilized information; Part of the measurement result.

T_2 relaxation as well as complicated signal signatures in the frequency domain caused by long J-coupling evolution result in a decreased SNR that increases CRLBs. To circumvent this, sequences providing short TEs (≤ 10 ms) are preferable [33, 34] to facilitate the reliable quantification of partially overlapping metabolites, such as γ -aminobutyric acid (GABA), glutamate (Glu), and glutamine (Gln)⁶ [35]. The RF pulses, that are utilized in these sequences for localization, should be insensitive to B_0 and B_1^+ inhomogeneities to ensure a robust application. They should also provide a small CSD since it has to be ensured that signals from the various metabolites originate from the same location. Additionally, the pulses should exhibit low peak power and pulse energy to prevent limitations caused by hardware capabilities or SAR.

⁶However, there are certain cases where a long TE is chosen to investigate one specific metabolite multiplet that is most pronounced with this TE.

The SPECIAL [11, 12] spectroscopy sequence can be used to achieve high SNR and reasonably short TEs, as introduced in section 1.3.3. Moreover, a low sensitivity to B_1^+ inhomogeneity and a small CSD can be obtained by using an adiabatic inversion pulse in SPECIAL for the localization in one dimension [8]. Nevertheless, the HS pulse [36] that is proposed in the original implementation of SPECIAL for inversion prior to the excitation and which was used in several subsequent studies [37, 38, 39, 40, 41, 42], requires a high peak power in order to reach adiabaticity. There are UHF applications, e.g., in the hippocampus or other deeper brain structures, where sufficient peak power is simply not available with normally available hardware. To adapt the pulse to the insufficient B_1^+ peak amplitude, it can be either prolonged which sacrifices bandwidth to preserve the adiabaticity condition or run with lower peak amplitude, which sacrifices inversion efficiency and robustness to preserve bandwidth.

Lately, gradient-modulated pulses, such as the WURST [43] and the GOIA [44] pulse were introduced to MRS [45]. Compared to the HS pulse of equally chosen total pulse energy and duration, these pulses allow a sharper pulse profile and a significantly decreased CSD for the same inversion BW [46, 45]. These properties are expected to lead to improved measurement precision.

Even though all the aforementioned conditions are met and the CRLBs were successfully minimized for a certain *in vivo* acquisition, the CRLBs cannot provide information on the achievable precision of metabolite concentrations within a given experimental setting [47]. Hence, this part of the thesis aims to estimate the reproducibility and repeatability of *in vivo* metabolite concentrations obtained at 7 T with the SPECIAL sequence. Moreover, the impact of three different adiabatic inversion pulses, implemented in SPECIAL, on the measurement precision was determined. Out of these results, the achievable measurement precision of 13 human brain metabolites was derived; in contrast to the CRLBs, not only accounting for the smallest possible bound of the SDs of the model fit but as well for most of the operational and instrumental factors affecting the spectral data. Finally, for the given experimental setup, the MDCs [48] of 13 *in vivo* measured metabolites were determined.

2.2 Methods

2.2.1 MR Hardware

All phantom and *in vivo* acquisitions throughout this thesis were performed on a 7 T MR scanner (MAGNETOM 7 T, Siemens Healthineers, Erlangen, Germany) with

a head coil (NOVA Medical Inc., Wilmington, USA) consisting of a single-channel transmit birdcage and a 32-channel receive array. Both are shown in Figure 2.1.



Figure 2.1: Utilized 7 T Siemens MAGNETOM MR scanner with NOVA Medical head coil.

2.2.2 Inversion Pulse Implementation

The HS, WURST, and GOIA pulses were implemented [36, 43, 44] in MATLAB (The MathWorks, Natick, MA, USA) to obtain identical inversion slice thickness, pulse duration, and pulse energy. Bloch simulations with varying B_1^+ and B_0 were performed [49]. The three aforementioned adiabatic inversion pulses were inserted into the SPECIAL sequence, resulting in three different SPECIAL variants exhibiting otherwise identical timings and scan parameters. These three versions will be referred to as HS-SPECIAL, WURST-SPECIAL, as well as GOIA-SPECIAL, respectively, throughout this part of the thesis. The obtained pulse sequence scheme can be found in Figure 2.2a.

2.2.3 Phantom Acquisition

Phantom measurements were performed on eight different days in order to estimate the reproducibility of the three different SPECIAL variants containing the three different inversion pulses, i.e., HS, GOIA, and WURST, without biological influences. On five out of the eight days, two acquisitions were performed with repositioning the phantom in between. Thus, 13 data sets were obtained in total. To perform the experiments, an in-house built, homogeneous 10-cm diameter phantom with the following ingredients was used: Glu, N-acetyl aspartate (NAA), Gln, GABA, myo-inositol (Ins), aspartate (Asp), glutathione (GSH), the sum of glycerophosphocholine and phosphocholine (total choline - tCho), and the sum of creatine and phosphocreatine (total creatine - tCr), dissolved in agarose gel. To assure a more brain-like appearance of the phantom spectra, the pH was adjusted to 7.2 and microscopic monospheres were added that induce microscopic B_0 inhomogeneities and tune the T_2 to the physiological range.

The phantom was put in a phantom holder in the head coil to ensure a reproducible placement. Moreover, the target voxel was placed in the center of the phantom at an identical position for each acquisition. The statistical analysis was conducted in Python. Coefficients of variation (CVs) were calculated metabolite-wise for each sequence variant over all sessions by dividing the concentration's standard deviation (SD) by its arithmetic mean. The statistical differences between the three SPECIAL variants were determined by a Wilcoxon signed-rank test [50]. To allow an unbiased evaluation, Bonferroni correction was applied. It included the three different adiabatic inversion pulses, as well as the seven quantified metabolites. Thus, the significance level was shifted from p -value < 0.05 to p -value < 0.002 .

2.2.4 In Vivo Experiments

Nine healthy subjects (aged between 21 and 55 years, 7:1:1 female:male:nonbinary) were scanned after giving written informed consent according to local ethical regulations to estimate the measurement precision and the impact of the three pulse sequence variants of in vivo acquisitions thereupon. Therefore, an unbalanced nested study design⁷ was chosen, which is shown in Figure 2.2c. Every subject was scanned on two different days which were approximately one week apart (six to eight days). Both sessions included two measurements (M1-M2, and M3-M4), each of them consisting of the three SPECIAL variants. During the first session, the subject was

⁷Nested design occurs when each level of a factor is combined with only one level of another factor in the design.

repositioned between M1 and M2, while in the second session, M3 and M4 were obtained without repositioning in between. Since there were limitations on the total scan time due to the ethics regulations, the repeatability acquisitions in the second session were split into two respective scan blocks with two SPECIAL variants, e.g., HS- and GOIA-SPECIAL, investigated in scan block one and the third SPECIAL variant, e.g., WURST-SPECIAL, examined in the second. Note that the volunteer was not repositioned between consecutive acquisitions, e.g., WURST-SPECIAL and WURST-SPECIAL but between two sequence variants, e.g., WURST-SPECIAL and HS-SPECIAL. A schematic of the different acquisitions, sessions, and scan blocks is depicted in Figure 2.2d. The chronology of the three SPECIAL variants was cyclically permuted between different subjects to ensure that the pulse-performance assessments are not biased due to changing conditions over the duration of the protocol, e.g., an increased likelihood of subject movement towards the end of each scan block. This study design allows to distinguish between three scenarios: 1) two consecutive acquisitions without repositioning the volunteer, R_0 ; 2) two acquisitions obtained on the same day including new calibration and repositioning, $R_{1,M}$ (for minutes in-between); and 3) two acquisitions approximately one week apart, $R_{1,W}$, (for week in-between). Scenario 1) means the repetition of measurement under nominally identical conditions; it is thus a *repeatability* scenario. For scenarios 2) and even more so for scenario 3), some measurement conditions like shim settings or voxel positioning were no longer fully identical in both runs; these are consequently referred to as two different *reproducibility*⁸ scenarios [32]. If it was not possible to exclusively assess the individual reproducibility scenarios, the index was extended by a “c” for combined.

Within every scan block, the measurement protocol was the following: magnetization prepared - two rapid gradient echo (MP2RAGE) [51] images for tissue segmentation and voxel positioning were acquired with following parameters: TR = 5000 ms, TE = 2.51 ms, inversion time (TI) = 900 ms, isotropic voxel size = 0.75 mm. The VOI was positioned in the posterior cingulate cortex (PCC). To that end, the VOI was firstly placed in the middle between both hemispheres. Then, three layers to the right of the center, the VOI was angulated in the sagittal plane such that its lower edge coincided with the virtual line between the corpus callosum and the outer end of the parieto-occipital fissure, as shown in Figure 2.2b.

⁸It should be noted that the here described repetition scheme is, by the strict definition, not a reproducibility scenario, as not all parameters, e.g., the operators, are changed between acquisitions. Nevertheless, this term is used 1) in the absence of another term, and 2) to create a distinction from repeatability.

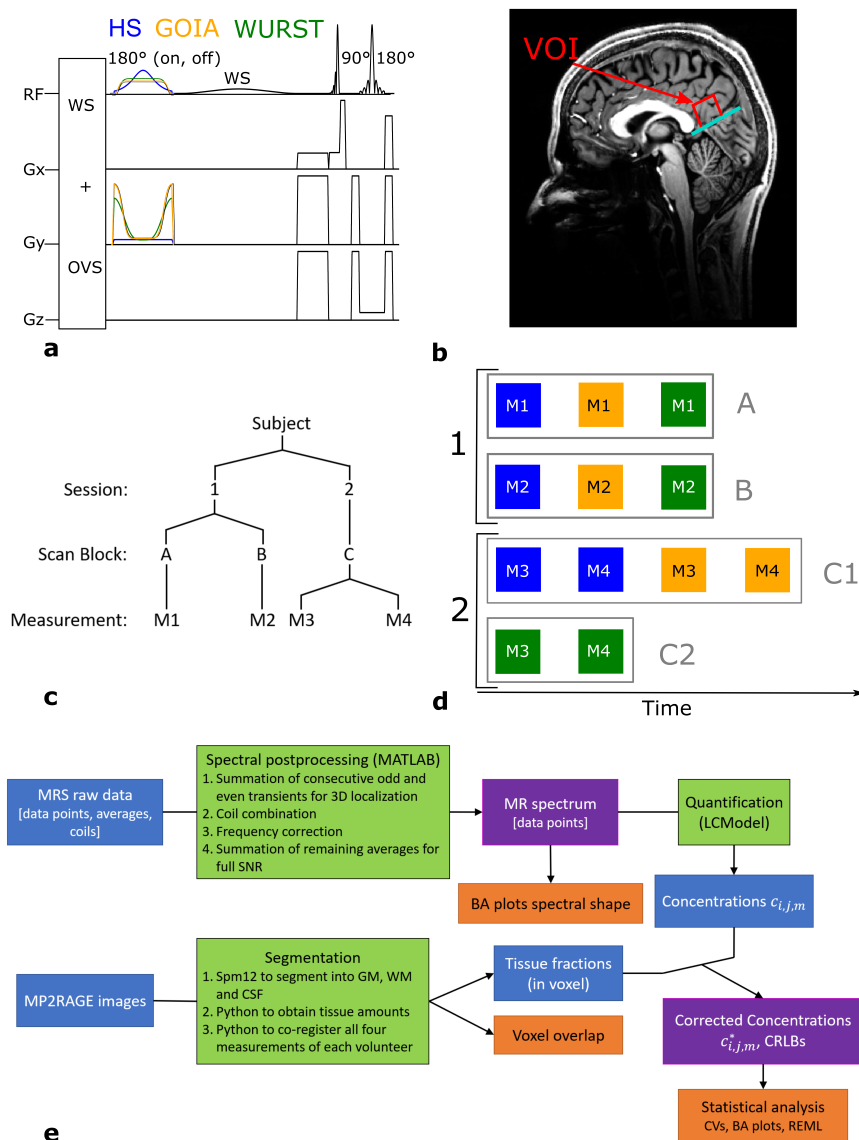


Figure 2.2: a) Pulse sequence diagram of the here used SPECIAL sequence with three distinct adiabatic inversion pulses: GOIA (orange), HS (blue), and WURST (green). b) Exemplary voxel position in the PCC of one volunteer. The turquoise line indicates the connection between the lower edge of the corpus callosum and the outer edge of the parieto-occipital fissure. c) For each pulse sequence variant, an unbalanced nested study design was performed: The subject-wise repeatability (M3 and M4), the between-positioning reproducibility (M1 and M2), as well as the between-session reproducibility (M1 and M3) were assessed by repeating this scheme for every measurement. d) Scan scheme (exemplary for the first three subjects): On the first scan day in the first session (M1), SPECIAL employing HS, GOIA, and WURST was measured. After repositioning the subject (M2), all three sequence variants were measured in the same order as in M1. On the second scan day approximately one week later, in the first session, GOIA-SPECIAL and HS-SPECIAL were measured twice without repositioning in-between (M3 and M4). Then, the WURST-SPECIAL sequence was measured twice without repositioning. It was necessary to split the repeatability measurements into two scan blocks due to time restrictions in the ethical regulations of the institute. e) Flow chart of the statistical analysis steps. The blue boxes indicate the measured or post-processed data, while the purple boxes refer to the resulting data, which were then used for different statistical analyses (indicated by the orange boxes). The necessary processing steps are listed in the green boxes. Reprinted from [26].

First- and second-order B_0 shim configurations were optimized for the voxel with a MATLAB-based shim tool [52, 53], utilizing a B_0 map acquired with the following parameters: TE1 = 6.02 ms, TE2 = 7.04 ms, TR = 620 ms, 3 mm isotropic resolution. The voxel-based B_1^+ calibration was obtained by varying the voltage of the pulse and fitting the resulting water peak amplitude in dependence of the applied voltage to obtain a 90° flip angle (fitting function: $V = a(\sin(x - b) \cdot \frac{\pi}{180})^3 + c$ [54]). Afterwards, SVS spectra with the respective SPECIAL variants were acquired, utilizing following scan parameters: TR = 6500 ms, TE = 9 ms, VOI = (20 mm)³, spectral width = 4 kHz, number of averages = 64, delta frequency = -2.3 ppm, and vector size = 2048. The obtained spectra were put into reference to an acquisition of four averages without water suppression that was performed after every metabolite spectrum measurement using the respective SPECIAL variant.

2.2.5 Spectral Post-Processing

The obtained metabolite and water spectra were post-processed with an in-house written MATLAB tool which included the summation of even and odd transient pairs, that were acquired with a phase shift of 180° in the receive phase to get the full localization. Subsequently, weighted and phase-corrected coil combination [55], frequency correction on the basis of the NAA peak at approximately 2 ppm, as well as averaging were performed. The quality of the acquired spectra was examined for every volunteer and SPECIAL variant by calculating the SNR and width of the unsuppressed water line.

2.2.6 Metabolite Quantification

The data were quantitatively analyzed utilizing LCModel [56] in the range of 0.2 and 4.2 ppm. A basis set for LCModel fitting containing signatures of alanine (Ala), aspartate (Asp), ascorbate (Asc), tCho, tCr, GABA, glucose, Gln, Glu, GSH, Ins, lactate (Lac), NAA, N-acetylaspartylglutamate (NAAG), phosphoethanolamine (PE), scyllo-inositol, and taurine (Tau) was simulated in Vespa [57]. To take the macromolecules into consideration, colleagues at the institute performed a metabolite-nulled in vivo measurement in one healthy volunteer. Then, the macromolecules were modeled in one basis function, as recommended by a recent consensus paper [58].

2.2.7 Segmentation and Tissue Fraction Correction

To enable a comparison of the measured metabolite concentrations among the subjects, the MP2RAGE images for each volunteer and session were segmented into cerebrospinal fluid (CSF), white and gray matter (WM and GM, respectively) with SPM12 [59]. Afterward, an in-house written python tool was used to determine the WM, GM, and CSF fraction for each voxel. The output concentration obtained by LCModel was then corrected, $c_{i,j,m}^*$, to account for the session- and subject-specific CSF fraction, as well as for relaxation processes [60]:

$$c_{i,j,m}^* = \frac{c_{i,j,m}}{\exp(-\frac{TE}{T_{2,m}})(1 - \exp(-\frac{TR}{T_{1,m}}))(1 - f_{CSF,i,j})}. \quad (2.1)$$

$c_{i,j,m}$ refers to the concentration of the metabolite m for subject i , and session j . $T_{1,m}$ and $T_{2,m}$ describe the metabolic specific relaxation times and f_{CSF} indicates the CSF fraction for subject i and session j . Note that the correction of the metabolite relaxation times assumes that the voxel mostly consists of GM. However, the averaged WM and GM tissue fractions are taken into account for the T_2 effect of water. They were used to determine the attenuation factor for the water scaling in LCModel. T_2 relaxation times of 37 ms and 45 ms for WM and GM were used, respectively [61], resulting in a water attenuation factor of 0.8111.

The reproducibility of the voxel position was determined by calculating the WM, GM, and CSF fraction for all four sessions and by evaluating the intra-subject CV for the CSF fraction. Additionally, an in-house written python tool was utilized to assess the voxel overlap between two sessions by co-registering two MP2RAGE images. A flow chart that gives an overview of all post-processing steps, the obtained data, and the resulting analysis is depicted in Figure 2.2e.

2.2.8 Statistical Analysis

Intra-subject CVs were determined for each pulse sequence variant, metabolite, and subject [62] to evaluate the test-retest reproducibility quantitatively. Statistical differences of the paired mean for every volunteer were assessed between the three inversion RF pulse types, CRLBs, and CVs by using a non-parametric Wilcoxon signed-rank test [50]. As a result of Bonferroni correction, the significance level of $p < 0.05$ was shifted to $p < 0.001$, including the 13 quantified metabolites and the three different adiabatic inversion pulses.

A summary and short explanation of all the differently determined SDs, which will be introduced in the following, is shown in Table 2.2.

Table 2.2: Explanation of the different indices and symbols used for different SDs, σ , throughout this work. The symbols for the SD, $\sigma_{\text{scenario}}^{\text{method}}$, indicate the utilized method with the upper index while indicating the investigated scenario with the lower index. Note that the “c” within the scenario description indicates that the variance components of the respective scenario are evaluated combined and not individually. For the BA analysis of both, the concentrations and the spectral shape, only combined components are considered since it is not possible to disentangle the individual components separately. Table is adapted from [26].

	Index symbol	Explanation
method (upper index)	S	SD of the BA analysis obtained by the evaluation of the spectral shape as indicated by Equation (2.2) and (2.3)
	BA	SD of the BA analysis for the corrected metabolite concentrations, c_m^*
	REML	SD derived by the REML analysis from the corrected metabolite concentrations, c_m^*
scenario (lower index)	R_0	repeatability scenario; two acquisitions performed consecutively without any recalibration or repositioning within one scan block
	$R_{1,M}$	reproducibility scenario: “minutes between acquisitions”; two acquisitions with recalibration and repositioning within one session
	$R_{1,W}$	reproducibility scenario: “week between acquisitions”; two acquisitions performed in two sessions approximately one week apart
	$R_{1,Mc}$	$= \sqrt{(\sigma_{R_0})^2 + (\sigma_{R_{1,M}})^2}$, combined SD of the R_0 and $R_{1,M}$ scenario; SD effectively observed within the $R_{1,Mc}$ scenario
	$R_{1,Wc}$	$= \sqrt{(\sigma_{R_0})^2 + (\sigma_{R_{1,M}})^2 + (\sigma_{R_{1,W}})^2}$, combined SD of the R_0 , $R_{1,M}$, and $R_{1,W}$ scenario; SD effectively observed within the $R_{1,Wc}$ scenario

Bland-Altman (BA) plots [63] of the spectral shape of the metabolite acquisitions were calculated as follows: In the first step, the real parts of the spectra that should be compared with each other were normalized to the intensity of the NAA peak. Then, to obtain the y -value of one data point, $BA_{i,y}$, for the i th volunteer, the absolute of the real part of the compared spectra, $|x(f)_{i,Ma}|$, was subtracted for every frequency f , and the integral with a frequency range from $f_{\min} = 0.2$ ppm to $f_{\max} = 4.2$ ppm was taken:

$$BA_{i,y} = \int_{f_{\min}}^{f_{\max}} |x(f)_{i,Ma}| - |x(f)_{i,Mb}| df. \quad (2.2)$$

Note that Ma and Mb here refer to the measurements M1-M4. To obtain the x -value, $BA_{i,x}$, the integral of the absolute of the averaged real parts of the compared spectra,

$|\overline{x(f)}_i|$, was calculated over the same frequency range:

$$BA_{i,x} = \int_{f_{\min}}^{f_{\max}} |\overline{x(f)}_i| df. \quad (2.3)$$

A measure for the precision of the spectral shapes derived by the BA analysis within the scenarios R_0 , $R_{1,Mc}$, and $R_{1,Wc}$ is given by the SDs $\sigma_{R_0}^S$, $\sigma_{R_{1,Mc}}^S$, and $\sigma_{R_{1,Wc}}^S$, respectively. Note that the reproducibility SDs $\sigma_{R_{1,Mc}}^S$ and $\sigma_{R_{1,Wc}}^S$ could only be obtained as a combined effect since it was not possible to robustly separate the individual contributions. In addition to the spectral BA analysis, a BA analysis of the metabolite concentrations, σ^{BA} , was also performed. Therefore, the concentration difference between the two acquisitions was plotted over their arithmetic mean.

Moreover, the measurement precision of the individual metabolite concentrations derived from the three different SPECIAL versions was quantified. To this end, the variance components for each pulse/metabolite combination were extracted separately by a restricted REML [64] analysis, carried out in R version 3.6.3 [65], utilizing the nlme package [66]. The statistical model which was applied for the variance component extraction can be described as follows:

$$c_m^* = \mu_m + P + S + \delta_{R_0}^{\text{REML}} + \delta_{R_{1,M}}^{\text{REML}} + \delta_{R_{1,W}}^{\text{REML}}, \quad (2.4)$$

where c_m^* describes the relaxation-corrected concentration of the metabolite m ; μ_m stands for the general metabolite concentration mean for every pulse sequence variant; P is the effect of the individual adiabatic inversion pulses (HS, GOIA, or WURST); S refers to the subject effect; while the three $\delta_{R_x}^{\text{REML}}$ are random between-session effects, exhibiting each a mean of 0 and a variance $(\sigma_{R_x}^{\text{REML}})^2$. $\delta_{R_0}^{\text{REML}}$, which is the residual, reflects the measurement precision of back-to-back acquisitions, and thereby the repeatability scenario R_0 . $\delta_{R_{1,M}}^{\text{REML}}$ is a result of small differences in calibration and positioning; $\delta_{R_0}^{\text{REML}} + \delta_{R_{1,M}}^{\text{REML}}$ describes the combined repeatability and reproducibility scenario $R_{1,Mc}$ after the repositioning of the volunteer. $\delta_{R_{1,M}}^{\text{REML}}$ is a consequence of additional, e.g., physiological, random effects between two sessions one week apart; $\delta_{R_0}^{\text{REML}} + \delta_{R_{1,M}}^{\text{REML}} + \delta_{R_{1,W}}^{\text{REML}}$ represents then the repeatability and all combined reproducibility scenarios $R_{1,Wc}$. Subject and pulse are considered fixed throughout this analysis; conventionally, subject and pulse effect comparisons are the target quantity of a study, while the variances only have to be considered for the evaluation of the result's certainty. All the here described variances were assumed constant for every pulse/metabolite combination; in addition, the REML fit assumed normality for all the random effects and restricted the derived SDs to the range of natural numbers. As every variance in the chosen nested design impacts the next level

“up”, the interpretation and analysis will be restricted to the within-group SDs of the repeatability $\sigma_{R0}^{\text{REML}}$ - which are not affected by any other estimates - and the combination of all individual variances $(\sigma_{R1,Wc}^{\text{REML}})^2 = (\sigma_{R0}^{\text{REML}})^2 + (\sigma_{R1,M}^{\text{REML}})^2 + (\sigma_{R1,W}^{\text{REML}})^2$. Since no significant differences within the application of the three adiabatic inversion pulses were found, both SDs could be combined over all three respective pulses to evaluate the measurement precision of every quantified metabolite concentration. The obtained SDs were correlated to the CRLBs and to σ^{BA} . From the results of the REML analysis, it was possible to calculate the MDCs, utilizing the standard error of measurement SEM, as follows [67, 48, 68]:

$$\begin{aligned} \text{MDC} &= 1.96 \cdot \sqrt{2} \cdot \text{SEM}, \\ \text{SEM} &= \sqrt{\frac{(\sigma_{R1,W}^{\text{REML}}(\text{HS}))^2 + (\sigma_{R1,W}^{\text{REML}}(\text{GOIA}))^2 + (\sigma_{R1,W}^{\text{REML}}(\text{WURST}))^2}{3}} \end{aligned} \quad (2.5)$$

The code that was utilized to generate the BA plots for the spectral shape, as well as the one used for the REML analysis are publicly available at https://gitlab1.ptb.de/LRiemann/repeatability_reproducibility.git.

2.3 Results

2.3.1 Inversion Pulse Implementation

A detailed description of the used pulse parameters can be found in Table 2.3. The phases, magnitudes, and gradients of the three adiabatic inversion pulses are depicted in Figure 2.3. The inversion slice thickness, total pulse power, and duration for all three pulses were fixed and chosen such that the following conditions were met: 1) fulfilled adiabatic condition employing a reasonable safety margin while not exceeding peak power limitations, and 2) an inversion BW with a minimum of 1.2 kHz.

Table 2.3: *The parameters, derived from Bloch simulations, for the HS, GOIA, and WURST pulse, are shown. It is indicated in bold numbers which parameters were fixed during the process of the pulse design in order to obtain comparable results. The table is adapted from [26].*

		HS	GOIA	WURST
Duration	/ ms	7.50	7.50	7.50
$B_{1,\max}$	/ μT	24.78	16.10	16.51
Slice thickness	/ mm	20.10	20.06	20.02
G_{\max}	/ (mT m^{-1})	1.44	23.10	18.53
Averaged pulse energy	/ ($\mu\text{T}^2 \text{ ms}$)	15.27	15.26	15.24
BW	/ kHz	1.25	12.45	14.22
CSD	/ (mm ppm^{-1})	4.85	0.48	0.42

The BW of both gradient-modulated pulses is approximately ten times higher than the BW of the HS pulse provided that the slice thickness, pulse duration, and energy are fixed. A substantial reduction in CSD by 90% compared to the HS pulse is a consequence (Table 2.3), while also reducing the maximum RF amplitude by 33%, which led to a difference in peak voltage of approximately 100 V.

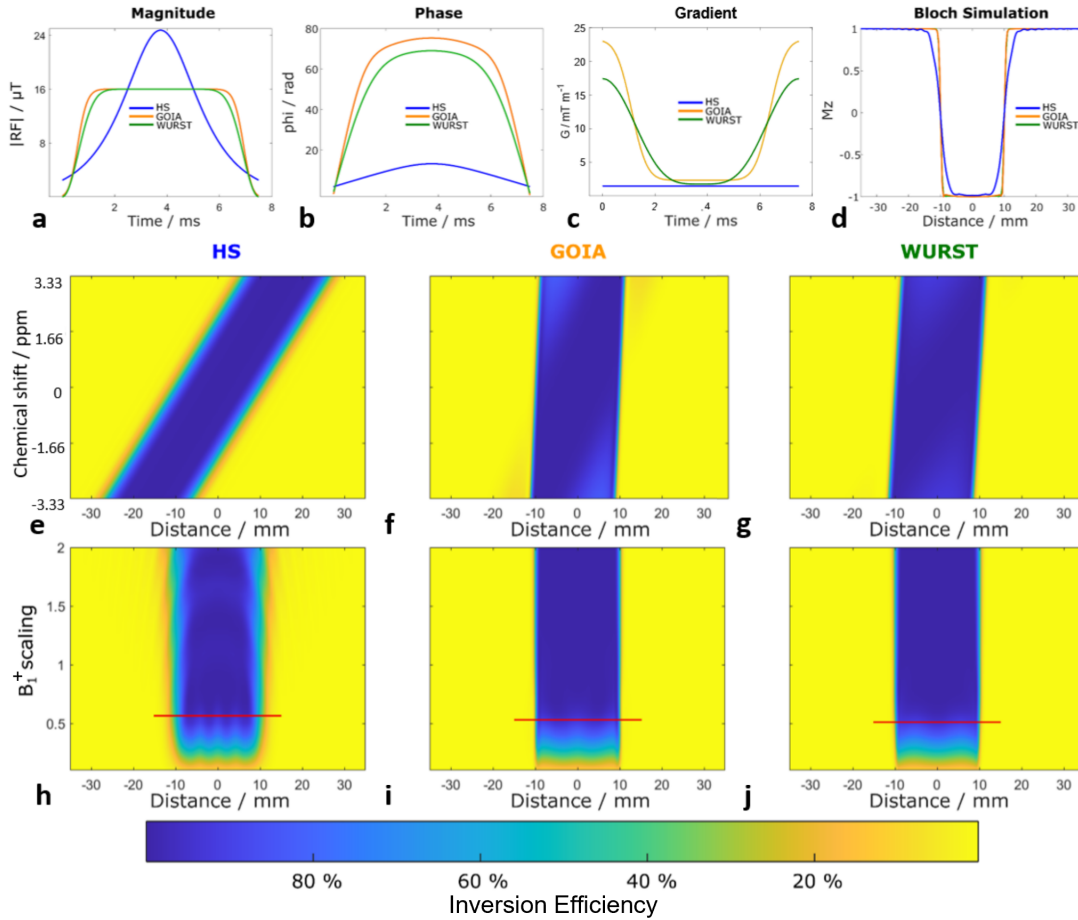


Figure 2.3: Results of pulse scaling (a-c) and Bloch simulations (d-j). The pulse energy and duration were fixed. a) RF amplitude, b) phase, and c) gradients of the three investigated adiabatic inversion pulses. d) The inversion profile of GOIA (orange), HS (blue), and WURST (green) have the same full width at half maximum (FWHM). The edges of the HS pulse profile are less steep and the profile shows small oscillations compared to the ones obtained by the gradient-modulated pulses. e-g) Inversion efficiency as a function of position and off-resonance frequency. CSD, i.e., a shift of the voxel position with frequency, exists for all three inversion pulses but is most pronounced for the HS pulse. h-j) Inversion efficiency as a function of position and scaled B_1^+ . The latter is normalized to the actually applied amplitude for each pulse, i.e., a value of 1 refers to the respective $B_{1,\text{max}}$, as stated in Table 2.3. The red lines indicate that the adiabatic condition is met for the entire voxel region, i.e., 100% inversion efficiency. To fulfill the adiabatic condition at resonance, approximately half of the applied amplitude would have been sufficient. The safety margin was introduced to ensure the fulfillment of the adiabatic condition even in regions of high B_1^+ inhomogeneity and prevent performance impairment under off-resonance conditions. Reprinted from [26].

2.3.2 Phantom Acquisition

It can be seen that the SNR and the width of the water line are similar for the three sequence variants in both mean and SD, whereas the required pulse voltage is significantly higher for the HS pulse than for the gradient-modulated ones ($p < 0.001$; Table 2.4). The obtained CVs, concentrations, and CRLBs exhibit similar values, and the concentrations and CRLBs show a small SD, as depicted in Figure 2.4. Neither the concentrations nor the CRLBs of the three SPECIAL variants showed significant differences. The CVs for the phantom acquisitions are $< 8\%$ for every metabolite.

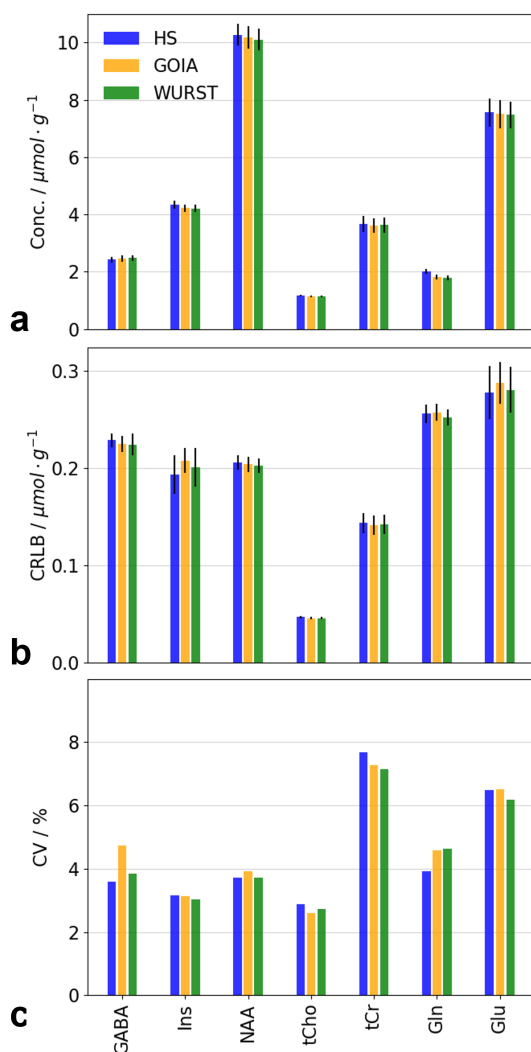


Figure 2.4: Comparison of a) quantified metabolite concentrations, b) CRLBs, and c) CVs for the metabolites measured in the phantom utilizing either HS-SPECIAL (blue), GOIA-SPECIAL (orange), or WURST-SPECIAL (green). The black error bars indicate the SD. As $CV = SD/\text{mean}$, there is no error bar for the CV plot. Reprinted from [26].

Table 2.4: Necessary transmit voltage U_{inv} , Water linewidth, and SNR_{water} for the three pulse sequence variants. The upper part shows the results for the phantom acquisition, where 13 spectra for each SPECIAL version were taken into account. In the lower part of the table, the in vivo results are depicted. 36 spectra for each sequence variant were taken into account. The table is adapted from [26].

	HS	GOIA	WURST
Phantom			
Water linewidth / Hz	10.3 ± 0.4	10.4 ± 0.5	10.4 ± 0.5
U_{inv} / V	128 ± 8	83 ± 5	86 ± 5
SNR_{water}	260 ± 10	261 ± 11	259 ± 11
In Vivo			
Water linewidth / Hz	13.7 ± 1.2	13.5 ± 0.9	13.5 ± 1.6
U_{inv}^a / V	284 ± 28	182 ± 18	189 ± 19
SNR_{water}	202 ± 15	199 ± 15	202 ± 17

^anumber of spectra = 27 as the voltage for the repeatability remained constant

2.3.3 In Vivo Measurements

It could be observed that the voxel overlap between different acquisitions across all subjects was $> 81\%$ in all cases, as depicted in Figure 2.5 and Table 2.5. The intra-subject CSF CV, i.e., the CV was determined over the four repeated acquisitions of each subject and then averaged over all nine subjects, was $(6.6 \pm 4.9)\%$.

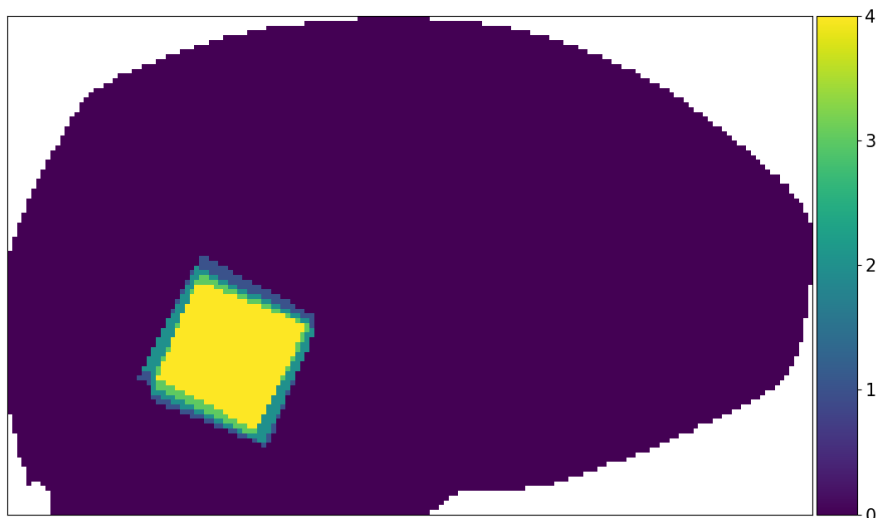


Figure 2.5: Voxel overlap for subject 6 in the sagittal view. The color map refers to the number of overlapping voxels, i.e., the overlap of all four voxels is indicated in yellow. Reprinted from [26].

Table 2.5: *Intra-subject WM, GM, and CSF fraction with the SDs averaged over all four repeated sessions and the voxel overlap averaged over the six possibilities ($M1/M2$, $M1/M3$, $M1/M4$, $M2/M3$, $M2/M4$, $M3/M4$) for each subject. The table is adapted from [26].*

Subject	1	2	3	4	5	6	7	8	9
Voxel Overlap / %	83.2	83.9	83.6	82.7	85.4	90.6	88.8	81.4	87.4
	± 4.0	± 4.7	± 4.2	± 4.5	± 7.7	± 1.0	± 4.9	± 9.4	± 3.4
CSF fraction / %	1.9	1.7	2.2	1.3	1.9	2.2	0.4	7.1	2.3
	± 0.7	± 0.1	± 0.5	± 0.2	± 0.7	± 0.3	± 0.1	± 0.4	± 1.0
GM fraction / %	78.0	74.8	77.7	75.4	69.2	75.5	78.3	72.5	78.1
	± 1.2	± 2.2	± 0.9	± 1.3	± 1.0	± 0.6	± 0.9	± 3.8	± 0.5
WM fraction / %	20.1	23.4	20.1	23.4	28.8	22.2	21.2	19.2	19.6
	± 1.8	± 2.2	± 0.7	± 1.2	± 0.6	± 0.7	± 1.0	± 3.4	± 0.8

As shown in Table 2.4 for phantom and in vivo measurements, the SNR and width of the water peak do not exhibit significant differences between the three different adiabatic inversion pulses implemented in SPECIAL.

It can be seen from Figure 2.6 that the spectral quality of the obtained spectra with all different sequence variants is high and no clear visual differences were observed. The BA plots of the spectral differences reveal a smaller dispersion for the gradient-modulated pulses than for the HS adiabatic inversion pulse for the R_0 scenario (repeatability). However, for the reproducibility scenarios $R_{1,Mc}$ and $R_{1,Wc}$, these differences in dispersion vanish: WURST- and HS-SPECIAL are on a par now with GOIA-SPECIAL performing slightly behind. Comparing among the three different scenarios, the following order of SDs was observed: $\sigma_{R_0}^S < \sigma_{R_{1,Mc}}^S < \sigma_{R_{1,Wc}}^S$. The BA plots derived from the quantified concentrations can be found in Figure 2.7. For most quantified metabolites, similar concentration variations were observed for all three SPECIAL variants, which is shown in Figure 2.8a. However, the concentrations from WURST- and GOIA-SPECIAL exhibit a significantly higher concentration for tCr and Glu (both $p < 0.001$). For HS-SPECIAL, 14 of the individual metabolite concentrations (out of 468: 9 subjects x 13 metabolites x 4 sessions) were discarded since they could not be quantified by LCModel, but only four and five concentrations for WURST- and GOIA-SPECIAL, respectively. In Figure 2.8b, it can be seen that the CRLBs for tCr, Asp, and NAA are significantly increased for the acquisitions with HS-SPECIAL compared to the SPECIAL variants employing gradient-modulated pulses. For both the concentration and the CRLBs, no significant differences between both gradient-modulated pulse sequence variants were observed. The highest intra-subject CVs for most metabolites were found for HS-SPECIAL, except for Lac, PE, and GABA, as depicted in Figure 2.8c. Correlation plots for the repeatability scenario

(M3 and M4) for the metabolites with the highest absolute concentration (NAA, tCr, Glu, and tCho) are displayed in Figure 2.9 and reveal that almost all points are within the confidence interval.

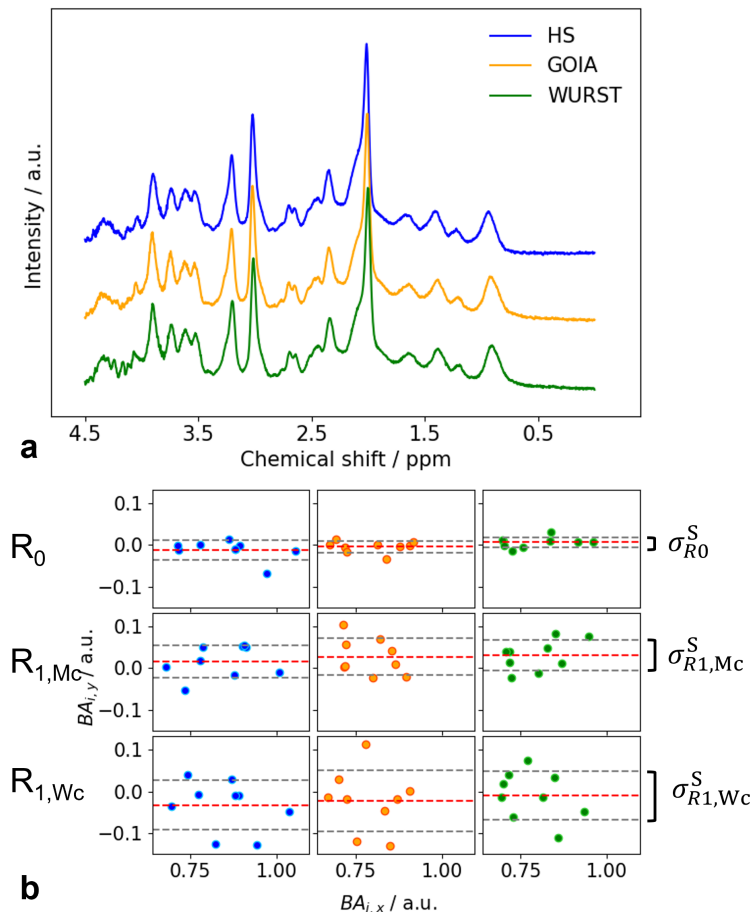


Figure 2.6: a) Exemplary spectra of M1 acquired with all three SPECIAL sequence variants (HS: blue, GOIA: orange, and WURST: green). b) BA plots of the spectral shape for the scenario R_0 (top), $R_{1,Mc}$ (middle), and $R_{1,Wc}$ (bottom). Every point in the BA plots is generated using Equations (2.2) and (2.3). The first acquisitions of the respective session were used to obtain $R_{1,Wc}$. The red line here indicates the arithmetic mean, while the gray ones refer to $1.96 \pm SD$, reflecting the confidence interval. The plots show the difference between the first observations in sessions approximately one week apart $R_{1,Wc}$, within a session with repositioning $R_{1,Mc}$ or between replicate observations within a session without any repositioning R_0 , plotted against the arithmetic mean of the two observations. Reprinted from [26].

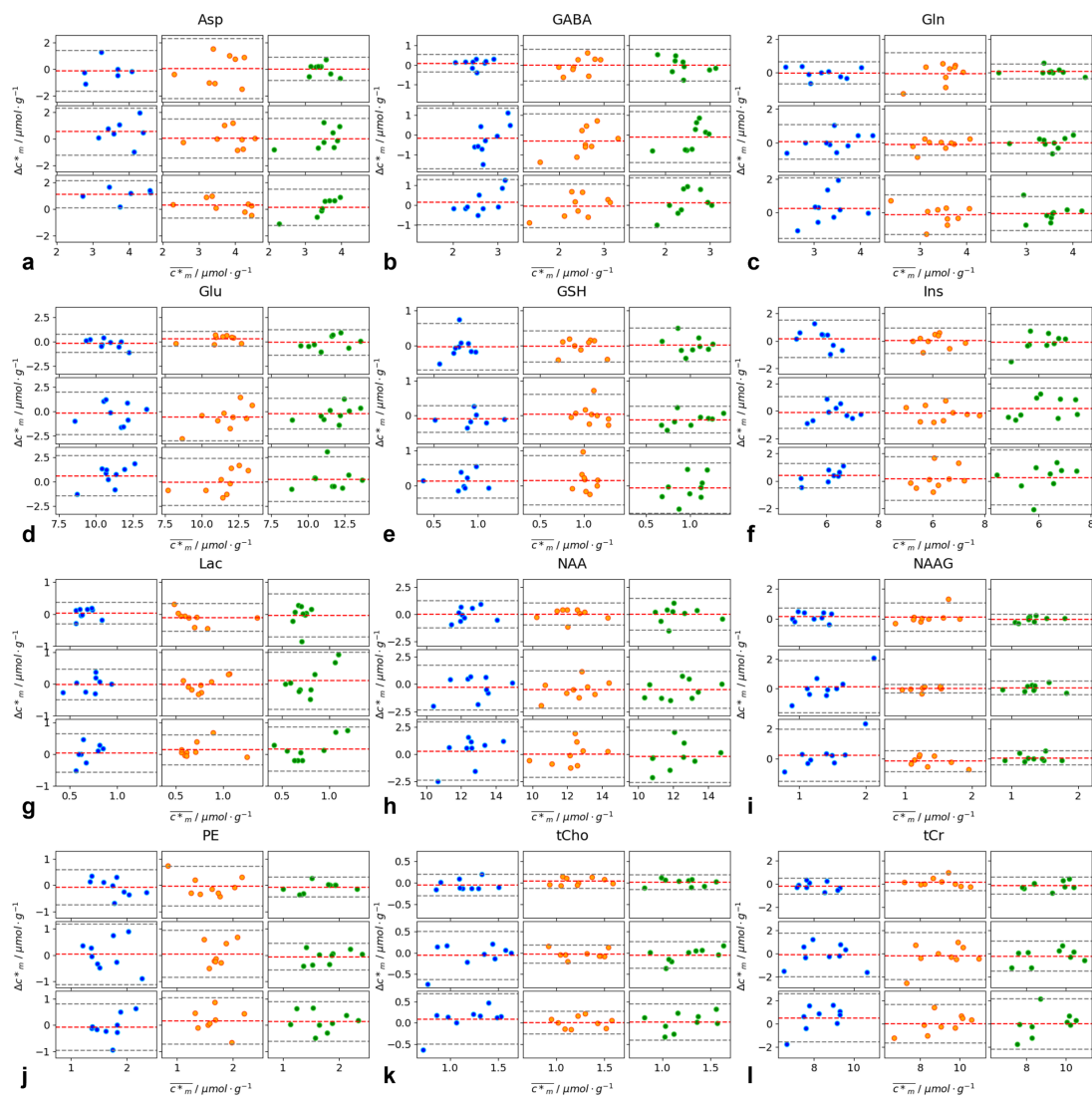


Figure 2.7: BA plots for each repeatability and reproducibility scenario for every pulse sequence variant (HS = blue, GOIA = orange, WURST = green) for the metabolite concentrations of a) Asp, b) GABA, c) Gln, d) Glu, e) GSH, f) Ins, g) Lac, h) NAA, i) NAAG, j) PE, k) tCho, and l) tCr. Reprinted from [26].

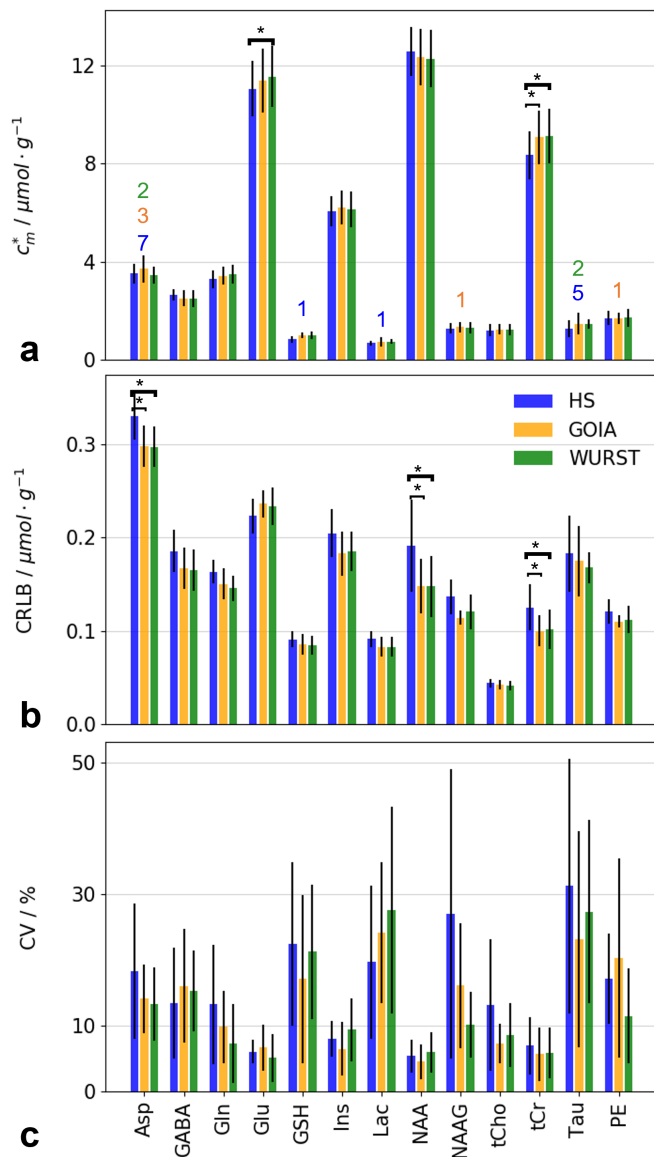


Figure 2.8: Metabolite quantification parameters for all three pulse sequence variants. a) Absolute metabolite concentrations c_m^* and b) absolute CRLBs averaged over all subjects and acquisitions, and c) intra-subject CVs averaged across all volunteers. The black error bars indicate the \pm SD of the quantified concentrations, CRLBs, and CVs across all volunteers. The SDs of CVs are not expected to be normally distributed due to their low degree of freedom. The error bars here only serve as a rough indicator of the distribution width. The CVs were first determined for each volunteer with respect to the four scan sessions and then averaged over all volunteers. 36 data sets, i.e., 9 subjects \times 4 sessions, were included for every metabolite and each of the three pulse sequence variants unless specific data sets could not be quantified by LCModel. The numbers above the averaged metabolite concentrations refer to the number of acquisitions that were discarded as it was not possible to quantify them. The asterisks indicate significant differences between HS and WURST or between HS and GOIA. Reprinted from [26].

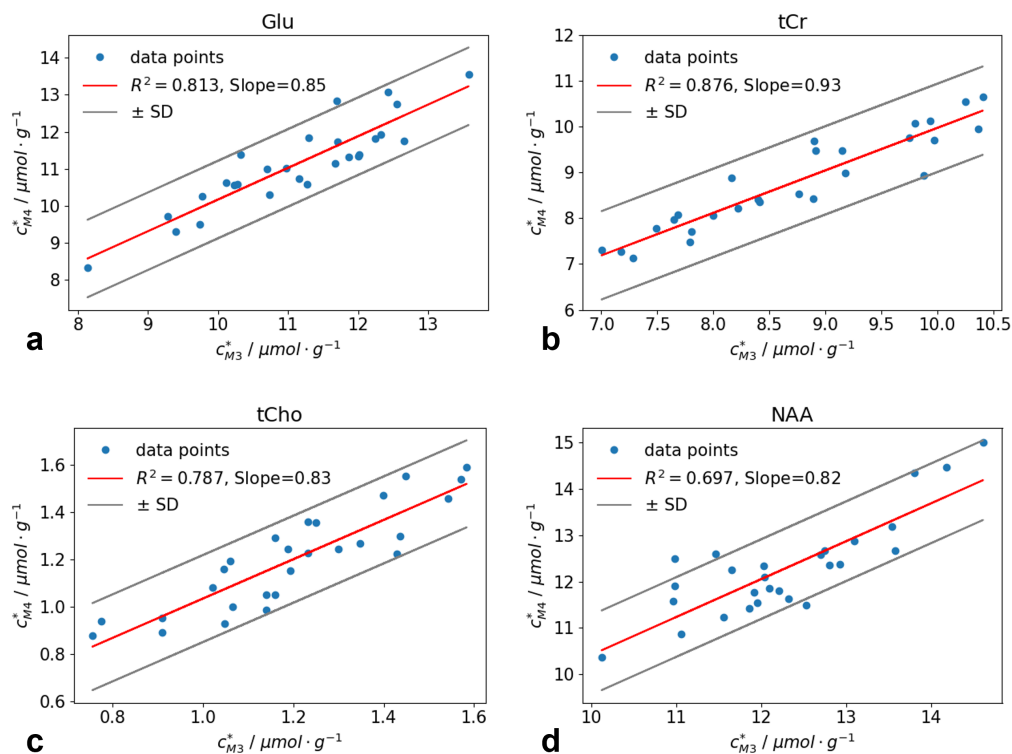


Figure 2.9: R_0 correlation plots over all subjects and adiabatic inversion pulses for a) tCr, b) Glu, c) tCho, and d) NAA. The red line refers to the fitted curve with its R^2 value and slope, while the gray lines indicate the confidence interval. Reprinted from [26].

2.3.4 Precision Evaluation

For both the $R_{1,Wc}$ and R_0 scenario, the pulse-wise σ^{REML} for all metabolites are shown in Figure 2.10a. Neither $\sigma_{R_{1,Wc}}^{\text{REML}}$ nor $\sigma_{R_0}^{\text{REML}}$ exhibited a consistent trend, favoring one of the investigated adiabatic inversion pulses. The individual results derived from the REML analysis, the BA analysis, and the CRLBs are displayed in Table 2.6. MDCs, that were calculated for each metabolite and the given setup, are shown in Figure 2.10b and Table 2.7.

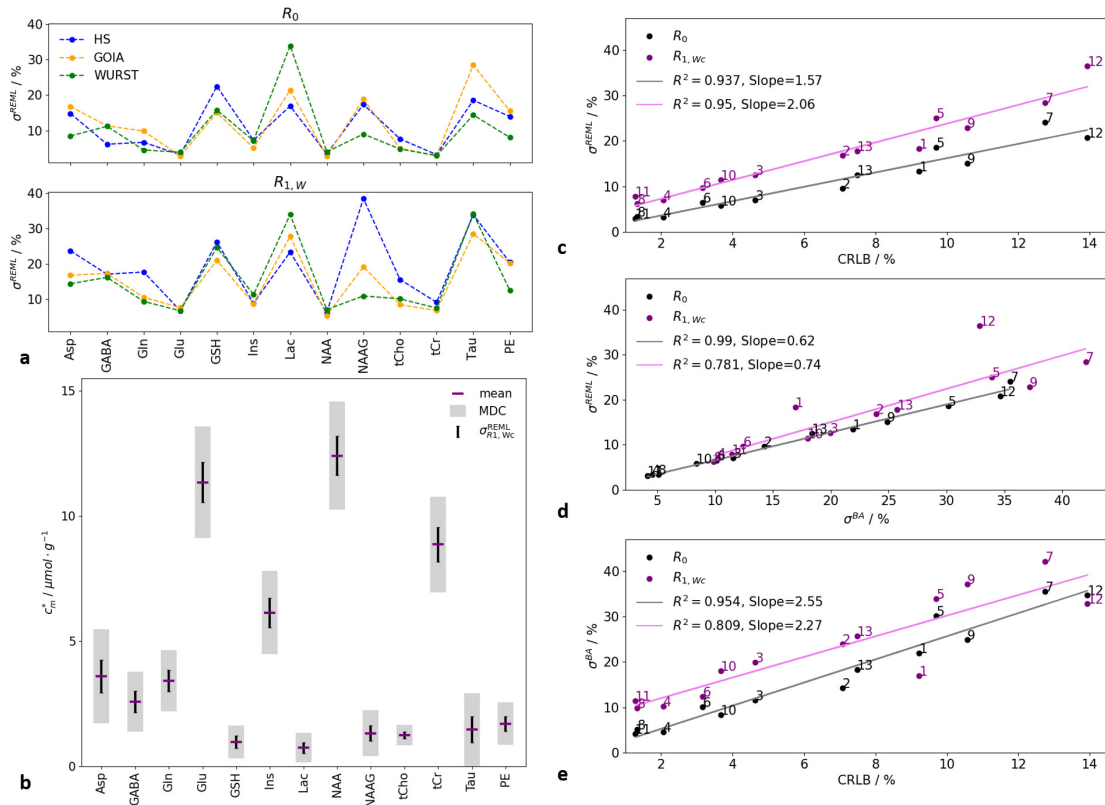


Figure 2.10: a) Pulse-wise relative SDs, i.e., the CVs, averaged over the volunteers, obtained by the REML analysis, for R_0 (upper plot) and $R_{1,wc}$ (lower plot) of all quantified metabolites. As no pulse sequence variant substantially outperforms another one, the data of all three were subsequently pooled to enhance the statistical analysis with regard to σ^{REML} and MDC. b) Mean concentrations (purple horizontal bars), $\pm \sigma_{1,wc}^{REML}$ (black vertical bars), and \pm MDC, (gray box) of metabolites. Correlation plots between c) σ^{REML} and relative CRLBs, d) σ^{REML} and σ^{BA} , and e) σ^{BA} and relative CRLBs averaged over all three pulse sequence variants and all volunteers. The $R_{1,wc}$ scenario is denoted in purple, while the R_0 scenario is indicated in black. Each point represents one metabolite: 1: Asp, 2: GABA, 3: Gln, 4: Glu, 5: GSH, 6: Ins, 7: Lac, 8: NAA, 9: NAAG, 10: tCho, 11: tCr, 12: Tau, 13: PE. Reprinted from [26].

Table 2.6: Values resulting from the REML analysis for every inversion pulse type for all metabolites: The SDs of the combined reproducibility $\sigma_{R1,Wc}^{REML}$, both reproducibility scenarios $\sigma_{R1,M}^{REML}$ and $\sigma_{R1,W}^{REML}$, as well as the repeatability scenario σ_{R0}^{REML} are depicted. N refers to the number of observations included in REML analysis for each group. To compare the obtained values, the CRLBs, as well as $\sigma_{R1,Wc}^{BA}$ are also given. Adapted from [26].

Pulse	M	Mean	N	$\sigma_{R1,W}^{REML}$	$\sigma_{R1,M}^{REML}$	σ_{R0}^{REML}	$\sigma_{R1,Wc}^{REML}$	$\sigma_{R1,Wc}^{BA}$	CRLBs
		/ $\mu\text{mol g}^{-1}$		/ $\mu\text{mol g}^{-1}$					
HS	Asp	3.570	29	0.468	0.465	0.529	0.846	0.520	0.377
	GABA	2.654	36	0.000	0.424	0.163	0.454	0.588	0.188
	Gln	3.302	36	0.469	0.271	0.221	0.585	0.914	0.170
	Glu	11.052	36	0.000	0.667	0.350	0.753	1.054	0.224
	GSH	0.845	35	0.131	0.000	0.211	0.248	0.245	0.098
	Ins	6.051	36	0.312	0.000	0.440	0.540	0.459	0.207
	Lac	0.685	35	0.028	0.106	0.116	0.160	0.311	0.097
	NAA	12.571	36	0.296	0.589	0.426	0.785	1.357	0.196
	NAAG	1.295	36	0.000	0.444	0.225	0.498	0.890	0.156
	tCho	1.204	36	0.000	0.164	0.092	0.188	0.300	0.048
	tCr	8.344	36	0.405	0.588	0.267	0.763	1.056	0.130
	Tau	1.360	30	0.411	0.396	0.254	0.624	0.390	0.206
PE	1.707	36	0.000	0.256	0.238	0.349	0.452	0.127	
GOIA	Asp	3.743	33	0.000	0.000	0.629	0.629	0.485	0.311
	GABA	2.516	36	0.000	0.331	0.285	0.436	0.566	0.182
	Gln	3.440	36	0.135	0.000	0.339	0.364	0.601	0.155
	Glu	11.395	36	0.000	0.810	0.320	0.871	1.231	0.241
	GSH	1.022	36	0.089	0.120	0.154	0.215	0.360	0.090
	Ins	6.207	36	0.376	0.233	0.316	0.544	0.814	0.186
	Lac	0.752	36	0.134	0.000	0.161	0.209	0.243	0.091
	NAA	12.341	36	0.000	0.573	0.342	0.667	1.062	0.151
	NAAG	1.310	35	0.047	0.000	0.247	0.252	0.358	0.132
	tCho	1.248	36	0.076	0.041	0.062	0.106	0.135	0.044
	tCr	9.073	36	0.000	0.559	0.268	0.620	0.841	0.103
	Tau	1.527	35	0.000	0.000	0.447	0.447	0.557	0.213
PE	1.649	35	0.051	0.208	0.256	0.334	0.453	0.134	
WURST	Asp	3.471	34	0.000	0.405	0.294	0.500	0.695	0.306
	GABA	2.500	36	0.000	0.292	0.280	0.405	0.646	0.173
	Gln	3.493	36	0.244	0.155	0.158	0.329	0.511	0.148
	Glu	11.555	36	0.558	0.320	0.449	0.784	1.176	0.234
	GSH	1.008	36	0.191	0.000	0.159	0.249	0.367	0.090
	Ins	6.138	36	0.457	0.287	0.438	0.695	1.017	0.189
	Lac	0.748	36	0.000	0.001	0.254	0.254	0.359	0.089
	NAA	12.287	36	0.557	0.464	0.490	0.875	1.226	0.150
	NAAG	1.332	36	0.000	0.083	0.120	0.146	0.246	0.127
	tCho	1.233	36	0.051	0.097	0.059	0.125	0.216	0.042
	tCr	9.128	36	0.509	0.379	0.266	0.689	1.108	0.104
	Tau	1.457	34	0.394	0.218	0.210	0.497	0.519	0.195
PE	1.728	36	0.120	0.114	0.139	0.216	0.381	0.120	

Table 2.7: The MDCs for every metabolite, derived by the REML analysis and Equation (2.5), are depicted. The table is adapted from [26].

Metabolite	MDC / $\mu\text{mol g}^{-1}$
Asp	1.87
GABA	1.20
Gln	1.22
Glu	2.23
GSH	0.66
Ins	1.66
Lac	0.59
NAA	2.16
NAAG	0.92
PE	0.40
tCho	1.92
tCr	1.46
Tau	0.85

The correlation between σ^{REML} and σ^{BA} , between σ^{REML} and CRLBs, and between σ^{BA} and CRLBs, averaged over all pulses, can be found in Figure 2.10c-e. The highest $R^2 = 0.990$ was observed for the R_0 correlation between σ^{REML} and σ^{BA} , while the lowest $R^2 = 0.809$ was obtained for the $R_{1,Wc}$ correlation between σ^{BA} and CRLBs. The CRLBs account for 16% to 50% of $\sigma_{R1,Wc}^{\text{REML}}$ and 42% to 74% of σ_{R0}^{S} .

The utilized .npy files for the BA plots, the raw data, the results of the segmentation, as well as the metabolite concentrations that were utilized for the REML analysis can be found under [10.5281/zenodo.5500320](https://zenodo.org/record/5500320).

2.4 Discussion

The measurement precision of in vivo acquired metabolite concentrations for a given setup for both repeatability and reproducibility was assessed. To this end, REML and BA analyses were performed. The obtained results were then compared to the conventionally utilized CRLBs at 7 T for the SPECIAL sequence. Moreover, the influence of three different adiabatic inversion pulses within the SPECIAL sequence, namely, the commonly used HS pulse and two gradient-modulated ones, WURST and GOIA, on the reproducibility and repeatability were evaluated.

Compared to an HS pulse of the same inversion bandwidth, total pulse power, and duration [43], both gradient-modulated pulses require a substantially decreased peak RF amplitude in order to fulfill the adiabatic condition [45, 8], as shown in Table 2.4. This advantage can be useful, especially in applications where SAR or peak RF power are the limiting factor. Nonetheless, the slew rate and gradient strength limitations, as well as the increased sensitivity to gradient and ΔB_0 imperfections [69], need to be taken into account while planning an application study exploiting gradient-modulated pulses to avoid limitations on the nominal voxel size.

For all three different SPECIAL variants, the obtained in vivo concentrations of most quantified metabolites are very similar and well in line with literature values from that region [62] (see Figure 2.8). However, the concentrations of tCr and Glu, that were obtained with HS-SPECIAL, are significantly lower than the ones measured with the gradient-modulated versions, whereas the CRLBs are significantly higher for tCr, NAA, and Asp measured with HS-SPECIAL in comparison to both other versions. In contrast to the differences observed for in vivo acquisitions, the CRLBs, concentrations, and CVs are similar for all three sequence variants in the phantom measurements, as depicted in Figure 2.4. A possible explanation for these differences between phantom and in vivo acquisition might be the sharper pulse profiles and fundamentally decreased CSD of the gradient-modulated pulses in comparison to the HS pulse, in conjunction with spatial changes in tissue distribution in the brain. It can be assumed that the effect on other metabolites is similar but not identifiable as unambiguously, since several signals in their respective frequency range overlap. Both the smaller number of discarded, non-quantified metabolite concentrations, as well as the decreased intra-subject CVs of the measurements utilizing the gradient-modulated pulses suggest that the properties of the gradient-modulated pulses within SPECIAL exhibit a positive effect on LCModel’s quantification robustness compared to the HS adiabatic inversion pulse, in particular for low concentration metabolites. Similar effects on the fit-robustness are expected if the CSD of the refocusing and excitation pulse were also reduced.

To avoid over-interpretation of significance levels caused by the small sample size, the statistical significance was evaluated by a non-parametric statistical test, namely the Wilcoxon signed-rank test, since a normal distribution of the data could not be assumed [70]. This test results in more conservative estimates than its parametric pendant, the paired t-test.

The assessment of repeatability and reproducibility lately received increased attention in the MRS community, e.g., the evaluation of test-retest reproducibility with CVs [62] or the comparability of different sites or scanners [71, 72, 73]. However, the use of an unbalanced, nested study design extends the established concepts and thus

enables a realistic estimation of the SDs of in vivo metabolite concentrations via REML and BA analysis for the first time.

Conventionally, the metabolite concentrations that are obtained after acquisition, post-processing, and absolute quantification represent the clinically relevant results, and hence their precision is an integral part of clinical assessments. Nonetheless, the here introduced BA analysis of the spectral shape (Figure 2.6b) allows a complementary measure for the repeatability and reproducibility of in vivo MR spectroscopy as the points in the BA plots are not influenced by inaccuracies that might be an inherent part of the utilized quantification model. This approach thereby provides additional information on the repeatability and reproducibility independent of the quantification pipeline. Although no differences within the visually assessed spectral quality, SNR, and water linewidth were observed between the three SPECIAL versions, suggesting a similar performance of all three pulses, the BA analysis of the spectral shape exhibits small differences between the three pulse sequence variants in vivo. It was revealed that both gradient-modulated pulses used for the adiabatic inversion in SPECIAL lead to increased repeatability of the spectral shape. However, potential alterations in the calibration, inaccuracies in VOI positioning, and other effects between measurements performed after repositioning or on different days seem to outweigh this observed benefit.

The increased $\sigma_{RL,Wc}^S$ compared to $\sigma_{RL,Mc}^S$ might have various reasons: 1) some of the subjects were scanned by different operators in the first and second session, which might have affected the combined reproducibility of VOI positioning; 2) day-to-day alterations of the scanner's performance; and 3) intra-subject physiological changes within two sessions. Effects caused by the first two points should ideally be minimized. Especially effects that originate from the differences in voxel positioning might be attenuated by automated voxel positioning routines, as already described by Dou et al. [74]. In this work though, a manual voxel positioning based on anatomical landmarks was performed (Figure 2.2b and Figure 2.5) since it reflects the workflow used in many clinical studies [75]. Although all the operators within this work carefully aimed to place the VOI as reproducible as possible, only a mean VOI overlap of 85.2% could be accomplished (Table 2.5), which was lower than the one demonstrated to be feasible with automated VOI positioning routines [74]. Hence, this is expected to negatively impact the measurement precision obtained within this work. Nonetheless, this study introduces a framework that enables quantifying the impact of measures taken to increase the measurement precision, such as the aforementioned automated VOI positioning routines. Effects that are a result of actual physiological changes, however, may constitute the answer to the initial research question, e.g., in longitudinal studies. Moreover, as MRS is currently advancing into a broader clinical utilization, the need

to define “normal” ranges of these physiological changes arises, as well as deviations thereof, to make it feasible as a diagnostic tool on a single-subject basis.

Poor B_0 shimming would result in increased metabolite linewidths which would impede correct quantification as the adjacent peaks would exhibit a larger overlap. This would lead to larger CRLBs and might also result in larger SDs of the calculated metabolite concentrations. However, if poor B_0 shimming is reproducible, the BA analysis of the spectral shape would not be expected to change substantially. In contrast, in the case of non-reproducible B_0 shimming leading to vastly different linewidths in the compared measurements, the BA analysis of the spectral shape is expected to exhibit a larger variance, and the SDs of metabolite concentrations are likely to be substantially increased compared to the measurements presented in this work.

It should be mentioned when evaluating the BA analysis of the calculated metabolite concentrations for both the repeatability and reproducibility (Figure 2.7) that while $\sigma_{R0}^{BA} < \sigma_{R1,Wc}^{BA}$, the effect is smaller than in the analysis of the spectral shape, and no consistent trend can be determined between $\sigma_{R1,Mc}^{BA}$ and $\sigma_{R1,Wc}^{BA}$. Both of these findings indicate that inaccuracies in LCMoel’s fitting model and differences in its fit quality “mask” the real differences between the two investigated reproducibility scenarios.

The results obtained by the REML analysis show a similar trend, see Table 2.6. The REML analysis does not allow negative estimates, as negative variances would not make physical sense. Combining this with the relatively large within-group effects and the modest degrees of freedom led to various variance contributions of both investigated reproducibility scenarios to be either estimated as nominally zero or very close to. It is worth noting though that either $\sigma_{R1,Wc}^{REML}$ or $\sigma_{R1,Mc}^{REML}$ is estimated as zero, never both variances at the same time. However, it should be stressed that this does not mean that the group means from both reproducibility scenarios - either $R_{1,Mc}$ and R_0 if $\sigma_{R1,Mc}^{REML} = 0$, or $R_{1,Wc}$ and $R_{1,Mc}$ if $\sigma_{R1,Wc}^{REML} = 0$ - are completely identical; it only indicates that they are closer together than was expected from the within-group variance. Thus, the two investigated reproducibility scenarios, as well as the effect of their respective variance contribution on the overall measurement precision are not clearly separable for most of the metabolites which might be a consequence of the small sample size of only nine subjects.

Although the results obtained by the REML analysis display a slight tendency towards lower SDs for the data of the gradient-modulated pulse sequence variant, there is neither consistency nor a statistically significant trend (Figure 2.10a). It was thus possible to pool the SDs for the combined reproducibility $\sigma_{R1,Wc}^{REML}$, as well as the

repeatability $\sigma_{R0}^{\text{REML}}$ of the three investigated pulses to strengthen the investigation on the MDCs for all 13 quantified metabolites (Figure 2.10b and Table 2.7). The variances that were obtained as $\sigma_{R1,Wc}^{\text{REML}}$ enable the calculation of the MDCs for the given setup. Furthermore, it can be seen that the strong correlation between the two repeatability measurements for tCr, Glu, tCho, and NAA for every volunteer proves the general ability of the given MRS method to reliably quantify metabolite concentration differences on a single-subject basis (see Figure 2.9).

Since the REML analysis consists of a multi-parameter fit model with several contributions to the total variance, it accurately compensates for the unbalanced nested study design and is able to weight incomplete data sets without dismissing the information completely. Hence, the SDs derived by the REML analysis are considered to provide a more reliable estimate than the BA analysis, as depicted in Figure 2.10d. Nonetheless, the BA analysis offers a valuable consistency check exhibiting similar trends, which facilitates the interpretation of the more complex REML analysis results. Moreover, the observed differences might decrease or even disappear for a larger sample size. By comparing the results of the REML analysis with the CRLBs (Figure 2.10c), it was revealed that the CRLBs only account for a small part of the measurement variance. This is not a surprising result since the CRLBs are described as the “lowest possible standard deviations of all unbiased model parameter estimates obtained from the data” by Cavassila et al. [31], which are limited to variance contributions originating from the fitting procedure, like noise level or overlapping peaks [76]. Thus, they do not reflect any variance contributions due to imperfections or hidden unknowns that are not adequately modeled the fit functions, nor any contributions due to the limited reproducibility of the acquisition that can only be detected by repeated measurements [47]. It should be stressed that the introduced framework does not aim to replace the utilization of CRLBs, since this kind of repeated acquisition to obtain the metabolite concentration’s SDs is unfeasible in most clinical settings, but rather to provide additional information to allow an improved understanding of the precision of the concentrations that were obtained by MRS. Nevertheless, strong correlations were observed between the CRLBs and the SDs obtained either by REML or BA analysis which underpins and reinforces concepts utilizing the CRLBs as weights in statistical analysis, as already suggested by Miller et al. [77]. Still, it is worth noting that in Figure 2.10c-e only the curves for σ^{REML} vs. σ^{BA} converge for vanishing errors while either of these exhibits a certain offset if plotted against the CRLBs. This is particularly pronounced for the $R_{1,Wc}$ scenario, indicating, that CRLBs are not just underestimating the true uncertainties by a factor of about two, in the given case, but that, in addition (and unsurprisingly), something is really missed if only CLRBS are considered.

The here used SPECIAL sequence requires an add-subtract scheme in order to achieve full spatial localization. While this provides the advantage of obtaining very short TEs at the same time as retaining the maximum achievable echo amplitude at a given TE, the add-subtract scheme increases susceptibility to the appearance of motion artifacts [78] compared to other techniques, such as semi-LASER (sLASER) which accomplishes full localization for every transient. This might have a negative impact on the achievable precision compared to single-shot localization approaches, especially if patients instead of healthy subjects are considered. Moreover, there is an ongoing discussion within the MRS community considering the trade-offs in modern single-voxel MRS sequences between minimized TE and reduced CSD, and which one should be favorable. One side is arguing that the decreased CSD of semi-SPECIAL (sSPECIAL) [78] or sLASER is expected to lead to an increased reliability of the obtained metabolite concentrations despite the longer TE. The other group of experts argues that short TEs, as in SPECIAL, are particularly beneficial to reliably determine J-coupled metabolites [33]. While this work did not aim to depict which one of the aforementioned influences on the precision is stronger, it introduces a framework that will enable future studies to evaluate and compare the precision of metabolite concentrations achieved with different TEs, CSDs, and numbers of transients.

The applicability of the values obtained within this work is undoubtedly limited to the utilized specific setup and methodology. It can be expected that the numbers will be different for other MRS sequences, brain regions, MR scanners, sequence parameters, post-processing pipelines, B_0 and B_1^+ calibrations, as well as fitting models. Nevertheless, this study provides a generally applicable framework to distinguish between different contributions to the total measurement variance which allows to evaluate the efficiency of specific measures that aim to lower individual variance contributions systematically. Lastly, this part provides the groundwork for an extended implementation of high-precision MRS into clinical routine, as it is only possible to reliably distinguish intra-subject differences within longitudinal studies or inter-subject differences in the comparison of cohorts from statistical fluctuations if they are larger than the obtained MDCs.

3 Fourier-based technique to decompose two simultaneously acquired MRS voxels with 2SPECIAL

3.1 Introduction

SVS is a well-established technique for quantifying metabolite concentrations in tissue in vivo [16]. As the name implies, this technique can be used to examine only a *single* voxel at a given time point. However, there are clinical applications that would benefit from simultaneous quantification of metabolite concentrations in multiple regions, e.g., to study a lesion and its contralateral control region [79]. Conventional SVS acquisition with sufficient SNR requires multiple acquisition repetitions to reliably quantify metabolites at lower concentrations, which takes approximately ten minutes [16]. Thus, the consecutive acquisition of multiple voxels is practicable only to a limited extent. MRSI could be utilized as an alternative technique. While this technique solves the problem of limited spatial coverage, it also often requires long scan times. Moreover, as an imaging technique, it also has the disadvantages of signal ghosting, as well as a wider point spread function compared to SVS [80]. Detection of low concentration metabolites is also difficult with MRSI due to the lower SNR for the typically smaller voxels.

To overcome the abovementioned limitations, an interleaved SVS acquisition pattern was introduced that incorporates dynamic shim updating [81] and thus increases spatial coverage for a given acquisition time compared to conventional SVS techniques. However, some research questions, such as specific fMRS studies [82], benefit from an “actual” simultaneous acquisition of data from two voxels, which is not achievable with an interleaved acquisition scheme.

As an alternative approach, simultaneous multi-voxel spectroscopy (sMVS) techniques have been proposed in recent years [83, 79, 37], in which signals are simultaneously acquired from two spatially separated voxels, usually utilizing MB excitation pulses, similar to SMS acquisition in MR imaging [84, 85]. To date, this sMVS technique was successfully merged with modified sLASER [83], PRESS [79], and STEAM [83], using SENSE-based algorithms to decompose signals originating from individual voxels [79, 83]. While these techniques enabled reduced acquisition times for multiple voxel acquisitions, these approaches depend on accurate coil sensitivity information requiring additional imaging data. In addition, the proposed sequences themselves typically have either lower signal intensity or a long minimum TE, which can be detrimental to the precision of quantification of low concentration metabolites and J-compounds [16].

To solve the aforementioned issues, the SPECIAL sequence, as described in section 1.3.3, might be a viable alternative. Previous results showed that the SPECIAL sequence can be used for sMVS by combining an MB HS inversion pulse before the excitation with either a Hadamard- [37] or a SENSE-based decomposition [86].

In this work, the 2SPECIAL sequence for simultaneous acquisition of the spectra of two different voxels using an MB WURST [43] pulse for the inversion prior to the excitation is investigated. The advantage of using gradient-modulated pulses, such as the WURST one, is that they require a significantly lower transmit voltage whilst also exhibiting a reduced CSD compared to the HS pulse, as described in chapter 2. In addition, they provide the necessary amount of flexibility regarding the adjustable parameters which are important for dealing with non-linearities that naturally occur in MB adiabatic pulses [10]. Additionally, a Fourier-based vGRAPPA technique is introduced to retrospectively decompose the simultaneously obtained signal from the two 2SPECIAL voxels. This method is based on split-slice GRAPPA [25, 23, 24], which is known from imaging and was described in more detail in section 1.4.2. vGRAPPA requires only the acquisition of low SNR spectra, but no further imaging data. Therefore, it offers the potential to further reduce motion artifacts since the measurement of low SNR data is fast and closer to the actual spectroscopic acquisition. The suggested combination of the 2SPECIAL sequence and the vGRAPPA decomposition technique is validated in phantom and in in vivo acquisitions. The results are then quantitatively compared to the ones obtained by a SENSE-based decomposition approach and the corresponding SVS measurements. In addition, the limitations of simultaneous acquisition in terms of MB properties of the pulses and voxel-wise B_1^+ adjustments and B_0 shimming are investigated.

3.2 Methods

3.2.1 Pulse Design and Sequence Implementation

In contrast to the general equation for multi-banding (cf. Equation (1.10) in section 1.3.2), in the case of the used gradient-modulated WURST pulse, $k(t)$ is not linear, but [69]:

$$k(t) = -\gamma \int_0^t G_s(t') dt', \quad (3.1)$$

where $G_s(t)$ represents the slice-selective, time-varying gradient. After generating the MB WURST pulse, it was inserted into the SPECIAL sequence to substitute the initially implemented SB HS pulse [36, 11, 12] and to form the 2SPECIAL sequence. To compare the obtained 2SPECIAL measurements to SVS acquisitions, the SB version of the WURST pulse will be used in SPECIAL.

The 2SPECIAL sequence diagram including the MB WURST for inversion prior to excitation is depicted in Figure 3.1. Similar to section 2.2, Bloch simulations of B_1^+ and the off-resonances ΔB_0 were performed to enable an assessment of the excitation performance and a comparison to the MB HS pulse [49, 26].

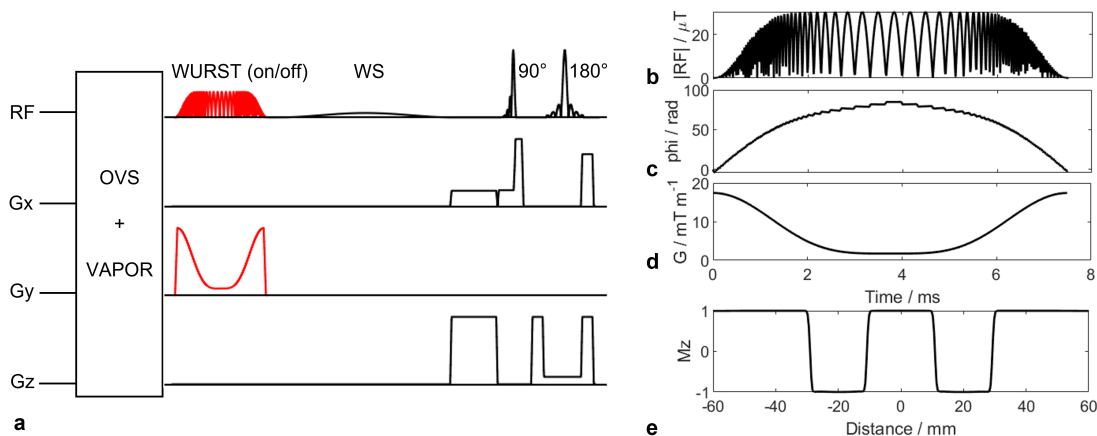


Figure 3.1: a) Pulse sequence diagram of the 2SPECIAL sequence containing an MB WURST inversion pulse (red) instead of the conventionally utilized SB HS pulse. Prior to the acquisition, OVS interleaved with VAPOR as water suppression is used. The inversion pulse was applied in alternating transients as an add-subtract scheme and followed by the 90° excitation pulse and the 180° refocusing pulse, as described in section 1.3.3, for complete spatial localization of the two voxels. b) B_1^+ amplitude, c) phase, d) modulated gradient, and e) Bloch-simulated magnetization profiles of the MB-WURST pulse with a B_1^+ scaling of 1 are shown. Reprinted from [27].

3.2.2 MR Protocol and Data Acquisition

To position the voxel and generate the sensitivity maps, which are necessary for the SENSE-based decomposition, MP2RAGE [51] images were acquired. Afterward, the B_1^+ calibration, i.e., the determination of the reference voltage for the VOI, was individually obtained for each voxel. Then, B_0 maps were acquired and utilized to obtain first- and second-order B_0 shim settings optimized for each individual VOI [52, 53]. The measured field distribution of each shim coil is approximated by a combination of spherical harmonic functions up 6th order as the shim basis, rather than by a single spherical harmonic function for every shim coil. Further details regarding calibration measurements, sequence, and pulse parameters can be found in section 2.2. After the calibration measurements, SVS acquisitions with the described individual calibration settings for each voxel were obtained and will be called SVS_{ind}. SVS measurements were then performed with B_0 and B_1^+ settings corresponding to the ones of the 2SPECIAL acquisition. In this case, the arithmetic mean of the reference voltages of each individual B_1^+ setting was used, as well as B_0 shim settings that were simultaneously optimized for both target regions. These acquisitions will be called SVS_{comb}. Lastly, sMVS data was obtained using 2SPECIAL and the combined-optimized B_0 shim parameters and B_1^+ settings. OVS and WS were performed as described in section 2.2 with the difference that an additional seventh OVS band was used for the sMVS acquisition to saturate the region in between the two voxels. To enable absolute quantification, additional reference acquisitions without WS were performed with four transients. The inter-voxel distances are given as center-to-center distances in the following sections if not stated otherwise.

3.2.3 vGRAPPA Decomposition

The vGRAPPA algorithm for decomposing sMVS spectra and reassigning the obtained signals to their respective spatial locations is built on the split-slice GRAPPA algorithm [85, 87, 25], which is described in section 1.4.2. The generation of the ACSs is modified to match the requirements for MRS. Conventionally, the fully sampled, k-space center is utilized as ACSs in GRAPPA or split-slice GRAPPA. These ACSs are then used to generate the GRAPPA kernels. However, since the sMVS and SVS acquisitions do not contain an equivalent to these reference lines, the required ACS for each individual voxel and channel is created using separate SVS measurements with low SNR. A flowchart to visualize the vGRAPPA decomposition algorithm is shown in Figure 3.2. First, the low-SNR FIDs of the individual transients are Fourier transformed to obtain the data in the frequency domain. Then, one ACS matrix for each individual voxel position is formed by stacking the complex

low-SNR spectra into two 2D matrices with dimensions 2048 bins ($= N_D$) \times 4 transients ($= N_A$). The acquisition of a low SNR spectrum took 58 seconds per voxel. Hence, the whole ACS acquisition took about two minutes in total. The ACS data are used to determine the (11×2) sized vGRAPPA kernels for each receive channel and voxel. The obtained kernel for each voxel is subsequently utilized to decompose the Fourier transformed sMVS data channelwise to their respective regions, i.e., each of the two calculated kernel matrices is convolved individually with the respective sMVS data. The resulting, individual channel data were then summed quadratically to obtain the final output. The vGRAPPA code is publicly available at <https://gitlab1.ptb.de/LRiemann/vgrappa-matlab-code>.

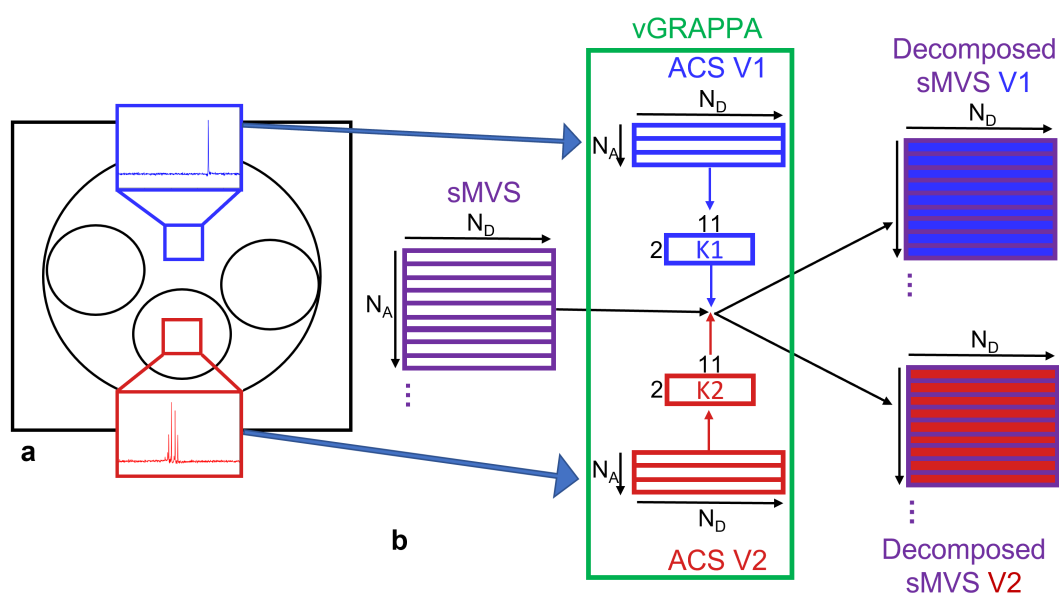


Figure 3.2: a) Schematic representation of the utilized phantom with the indicated voxel positioning in blue (glycine) and red (citrate) and the resulting post-processed low-SNR data. b) Schematic illustration of the vGRAPPA decomposition algorithm exemplary for one single channel: The acquired SVS data with low SNR (blue and red), where four transients (N_A) are measured for each voxel, are utilized to generate the channelwise ACS by 2D stacking of the transients with N_D data points. The kernel size is set to 11×2 . Subsequently, the obtained kernel is utilized to decompose the acquired sMVS data (purple) to their respective voxel areas (V1: purple/blue, V2: purple/red). In the end, the channelwise datasets were summed quadratically to obtain the final result. Reprinted from [27].

3.2.4 SENSE-based decomposition

The SENSE-based decomposition algorithm was utilized as previously described by Boer et al. [83]. The fundamentals of the SENSE algorithm are explained in section 1.4.1. To generate the required sensitivity maps for each receive channel, MP2RAGE

images were used: The image of one channel was divided by the sum of squares of all channels [19]. For the construction of the noise covariance matrix, the last 1000 FID points of each transient of the acquired sMVS spectra were employed.

3.2.5 Phantom Experiments

For the determination of the metabolite leakage, an in-house built multi-compartment phantom was utilized, consisting of a 210-mm diameter sphere, filled with four 50-mm diameter spheres each containing different metabolite solutions. The inner spheres were filled with 10 mmol solutions of citrate, choline, acetate, and alanine, respectively, and were surrounded by a 10 mmol glycine solution in the outer compartment. One voxel was placed inside the small citrate sphere, while the other one was positioned in the glycine-filled outer compartment at a distance of 55 mm.

3.2.6 In Vivo Acquisition

Data of twelve healthy volunteers (aged between 21 and 56 years, 7:4:1 female:male:nonbinary) were acquired after they gave written informed consent according to local ethical regulations. The order of spectroscopic measurements is depicted in Table 3.1, while the individual acquisition times for both sMVS methods and the consecutive SVS acquisition are stated in Table 3.2.

Table 3.1: *Spectral acquisition scheme for in vivo measurements. The application for each sequence includes four transients of metabolite spectra as a prior check or to generate the ACSs, 64 transients of metabolite spectra, as well as four transients of unsuppressed water signal to get absolute metabolite concentrations. Note that for the sMVS acquisition, the combined B_1^+ and B_0 shim settings were used. The table is adapted from [27].*

Acquisition	Voxel	Sequence
SVS _{ind}	V1	SPECIAL
SVS _{ind}	V2	SPECIAL
SVS _{comb}	V1	SPECIAL
SVS _{comb}	V2	SPECIAL
sMVS	V1+V2	2SPECIAL

Table 3.2: Acquisition time comparison between the consecutive acquisition of two voxels and both sMVS approaches with either vGRAPPA or SENSE-based decomposition. For the SENSE-based algorithm, the sensitivity maps must be calculated from MP2RAGE images or similar or acquired in an additional acquisition. For the consecutive two-voxel acquisition or the vGRAPPA-based algorithm, this is not mandatory if automatic positioning [74] is performed without the necessity of high-resolution image data. However, a spectrum with low SNR for each voxel is required for the vGRAPPA decomposition, but not for the SENSE-based approach. From these theoretical considerations, the minimum possible time was obtained. The realistic time considers that MP2RAGE images are required for positioning in standard in vivo protocols, as well as low SNR spectra for validation of all adjustment acquisitions. For both sMVS approaches, it should be possible to further reduce the time used for calibration, however, this was not investigated in this work. The table is adapted from [27].

Sequence	Time / min	Two Voxel SVS	vGRAPPA	SENSE
Calibration (localizer, B_0 shim, RF transmit voltage)	5	yes	yes ^a	yes ^a
MP2RAGE	12	no ^b	no ^b	yes
Low SNR spectra for ACS	2	no ^c	yes	no ^c
Voxel acquisition	10	2x	1x	1x
Σ Minimal possible Time / min		25	17	27
Σ Realistic Time / min		39	29	29

^acombined B_0 shim and B_1^+ adjustment

^bautomated positioning

^cconventionally acquired for validation of adjustment measurements

In ten subjects, the two voxels were placed between 46 mm and 60 mm apart due to individual anatomical differences in the left and right motor cortex. To investigate whether it is possible to separate the voxels from other non-lateral/contralateral brain regions, in the eleventh subject the voxels were positioned in GM-rich areas in the posterior and anterior cingulate cortex (PCC and ACC, respectively). For the twelfth subject, a GM-rich voxel in the ACC was selected along with a WM-rich one in the posterior hemisphere. Voxels in the non-lateral symmetric regions were placed 80 mm and 74 mm apart from each other for ACC/PCC and ACC-GM/occipital WM acquisition, respectively.

3.2.7 Spectral Post-Processing

The sMVS spectra decomposed with vGRAPPA, as well as the SVS acquisitions were post-processed with an in-house written MATLAB tool, which was described in section

2.2.5. In contrast to this description, a separate channel combining step was not necessary as it was already an inherent part of both decomposition approaches. The spectral quality was examined for both SVS acquisitions and both decomposed sMVS spectra for every volunteer by calculating the SNR and width of the unsuppressed water line.

3.2.8 Leakage Determination

To quantitatively assess the performance of both decomposition algorithms, the signal leakage between the two voxels was quantified. The term “leakage” is defined here and throughout this whole thesis as the integrated leakage signal, i.e., the metabolite signal of one voxel appearing in the spectrum of another voxel, normalized to the integrated spectrum of the original voxel.

In vivo leakage was also qualitatively evaluated by treating each of the individually acquired SVS_{comb} datasets as sMVS data and decomposing it to its respective regions. For this purpose, the data acquired from the first voxel was inserted into each of the decomposition algorithms as if they were sMVS data. In the ideal case, the decomposed spectrum of the first voxel should subsequently look like the SVS_{comb} data of that voxel, while the second spectrum should be random noise. For one subject, an evaluation was performed to determine whether the number of transients utilized as low SNR data for the vGRAPPA decomposition algorithm had an effect on the leakage. Moreover, the in vivo leakage depending on the distance over all subjects was evaluated, as well as the phantom leakage for the vGRAPPA algorithm depending on both the distance and the number of transients utilized to generate the ACSs.

3.2.9 Metabolite Quantification, Segmentation, and Concentration Correction

The metabolite quantification was performed as already described in section 2.2.6, whereas the segmentation and concentration correction was carried out as described in section 2.2.7.

3.2.10 Statistical Evaluation

Boxplots of the CRLBs and the corrected concentrations $c_{i,m,v}^*$ over all volunteers i and each voxel v for every metabolite m were calculated to assess the differences

between 1) vGRAPPA and SENSE-based decomposed spectra, 2) SVS_{comb} and both decomposed sMVS spectra, 3) SVS_{ind} and both decomposed sMVS spectra, and 4) SVS_{comb} and SVS_{ind} over all ten volunteers. Furthermore, BA plots [63] reflecting differences in the real parts of the spectral shapes, as described in more detail in section 2.2.8, were obtained for 2) to allow an evaluation of the spectral differences without any bias by the fit required for metabolite quantification.

To investigate the statistical differences in the CRLBs and metabolite concentrations, a non-parametric paired Wilcoxon signed-rank test [50] was performed. The following pairs of methods were compared: 1) vGRAPPA and SENSE-based decomposition, 2) SENSE-based decomposition and SVS_{ind}, 3) vGRAPPA decomposition and SVS_{ind}, 4) SENSE-based decomposition and SVS_{comb}, 5) vGRAPPA decomposition and SVS_{comb}, and 6) SVS_{comb} and SVS_{ind}. Bonferroni correction shifted the significance level from $p < 0.05$ to $p < 0.0038$ to account for the 13 quantified metabolites. Unlike conventional clinical trial designs, this study aims to demonstrate similarities rather than differences. Therefore, the p -value was not adjusted to $p < 0.00064$ by additionally considering the six measurement combinations, as this would result in a less conservative assessment. Note that neither the GM/WM nor the PCC/ACC spectra were included in the statistical analysis.

To obtain a quantitative performance measure for both SVS acquisition and both decomposition methods, the $\overline{\text{CRLBs}}$ is introduced, incorporating the CRLBs of the quantified metabolites as follows:

$$\overline{\text{CRLBs}} = \frac{\sum_{m=1}^{M(b)} \sum_{i=1}^I \sum_{v=1}^V \text{CRLB}_{m,i,v}}{N_{\text{CRLB}}}, \quad (3.2)$$

with b referring to the the CRLBs cutoff limit, which is varied between 5% and 60% in 5% steps, $M(b)$ depicting the 13 quantified metabolites depending on b , I being the ten subjects, V being the two voxels, and $N_{\text{CRLB}} = M(b) \times 2 \times 10$, i.e., the number of included data points. $N_{\text{CRLB,max}}$ is 260 (13 metabolites \times 10 subjects \times 2 voxels).

3.3 Results

3.3.1 Simulations

The modulated gradient, phase, amplitude, and pulse profile of the designed MB WURST adiabatic inversion pulse are depicted in Figure 3.1. The results of the Bloch simulation for three different between-voxel distances played out with the MB WURST pulse for varying B_1^+ and chemical shift are shown in Figure 3.3. The

inversion efficiency was reduced to 90% for edge-to-edge distances below 15 mm and a chemical shift of ± 2 ppm and above. For higher B_1^+ amplitudes, starting at about twice the applied value, the spatial definition of both voxels is blurred as an unintended partial inversion occurs outside the voxel, increasing with smaller distance. At smaller B_1^+ amplitudes, the performance of the MB WURST pulses was not impaired. The maximum required peak power for the here used MB WURST pulse was reduced by 23.75% compared to the MB HS pulse. Further details on the comparison between both MB pulses are shown in Figure 3.4. Figure 3.5 depicts just one example of how the multiple degrees of freedom of the WURST pulse can be exploited for different optimization goals.

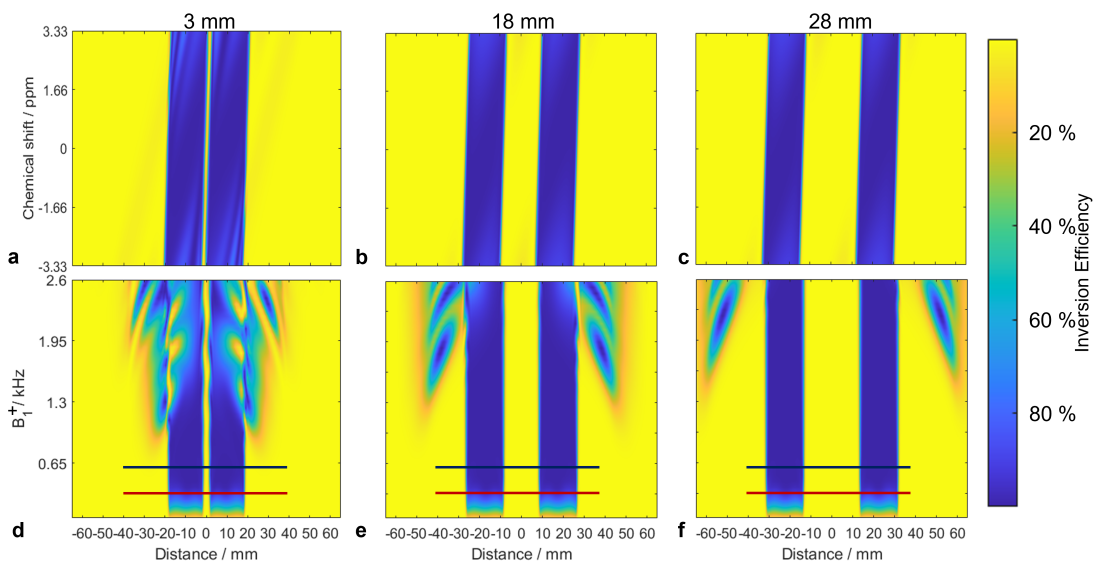


Figure 3.3: Results of Bloch simulations for varying CS (a-c), i.e., the positional shift of the voxel which is caused by varying the frequency, per ppm, and varying B_1^+ (d-f) for the MB WURST pulse at a between-voxel distance of 3 mm (a/d), 18 mm (b/e), and 28 mm (c/f, in vivo range). Inversion efficiency is depicted as a function of B_1^+ (d-f). The profiles of the inversion slices have an FWHM of 20 mm. The dark blue line refers to the applied amplitude of 0.65 kHz. The red line indicates an inversion efficiency of 100%, i.e., the adiabatic condition is satisfied across the whole voxel. For the MB adiabatic inversion pulse, the maximum B_1^+ was chosen such that about half of the applied amplitude would suffice to satisfy the adiabatic condition at resonance. The introduced safety margin ensures that the adiabatic condition is satisfied even in areas with high B_1^+ inhomogeneity and that the performance is not affected under off-resonance conditions. Reprinted from [27].

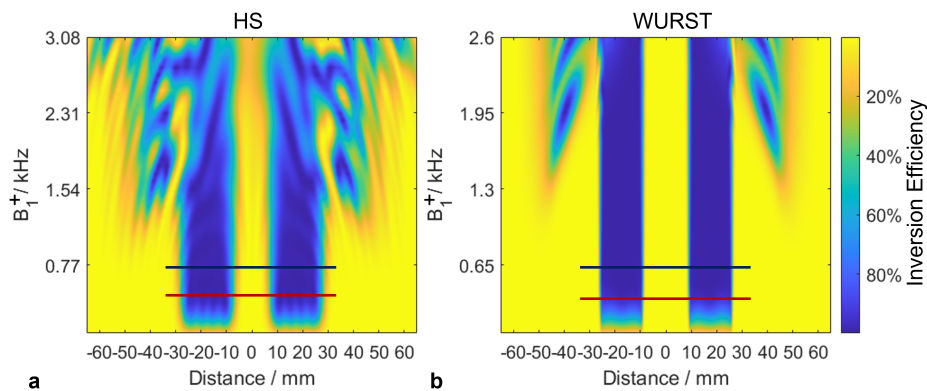


Figure 3.4: Comparison of the B_1^+ for a) an MB HS and b) the MB WURST pulse, as used within this study, at a between-voxel difference of 18 mm. The artifact, i.e., the unintended partial inversion, is larger for the HS pulse than for the WURST one. Moreover, the edge definition of the HS pulse is less sharp which makes it appear to have a smaller between-voxel distance. The blue line refers to the applied B_1^+ amplitude, the red line indicates the adiabaticity condition. Reprinted from [27].

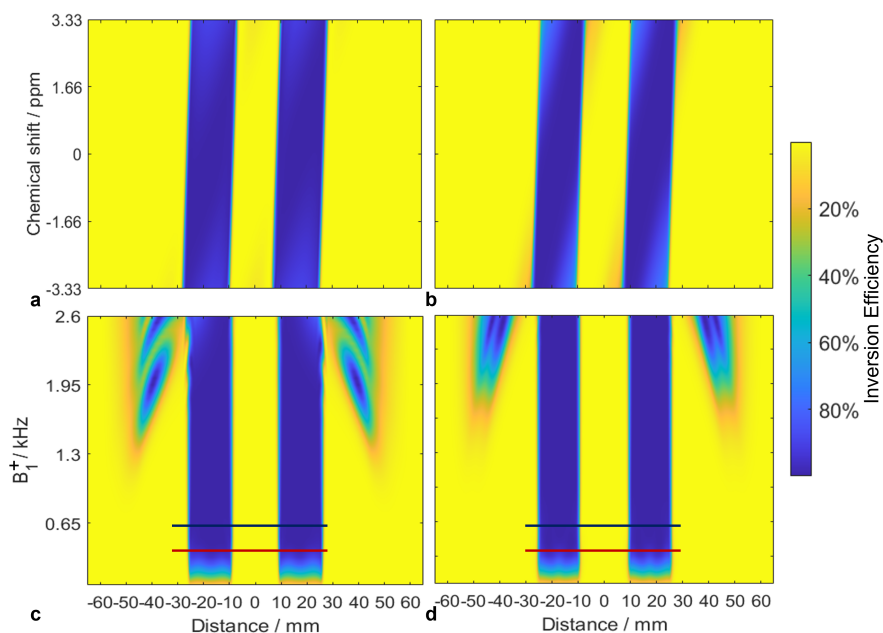


Figure 3.5: Comparison between two different optimizations of the MB WURST pulse at a distance of 18 mm from edge to edge. a-b) CS and c-d) B_1^+ for the pulse used for the *in vivo* measurements (a,c), or a second pulse optimized to reduce artifacts at high B_1^+ amplitudes (b, d). Note that in the latter case, the pulse becomes blurred at high off-resonances and was therefore not utilized. The pulse parameters for the pulse in a/c are: $B_{1,max}^+ = 0.65$ kHz, $G_{max} = 17.4$ mT m⁻¹, while for the pulse in b/d the following values apply: $B_{1,max}^+ = 0.62$ kHz, $G_{max} = 22.0$ mT m⁻¹. Reprinted from [27].

3.3.2 Phantom Acquisition

The performance of the 2SPECIAL decomposition with either of the two approaches was investigated with the two-compartment phantom described in section 3.2.5. The vGRAPPA algorithm resulted in a mean metabolite leakage of 3.4%, whereas SENSE-based decomposition resulted in a leakage of 5.1%, as depicted in Figure 3.6.

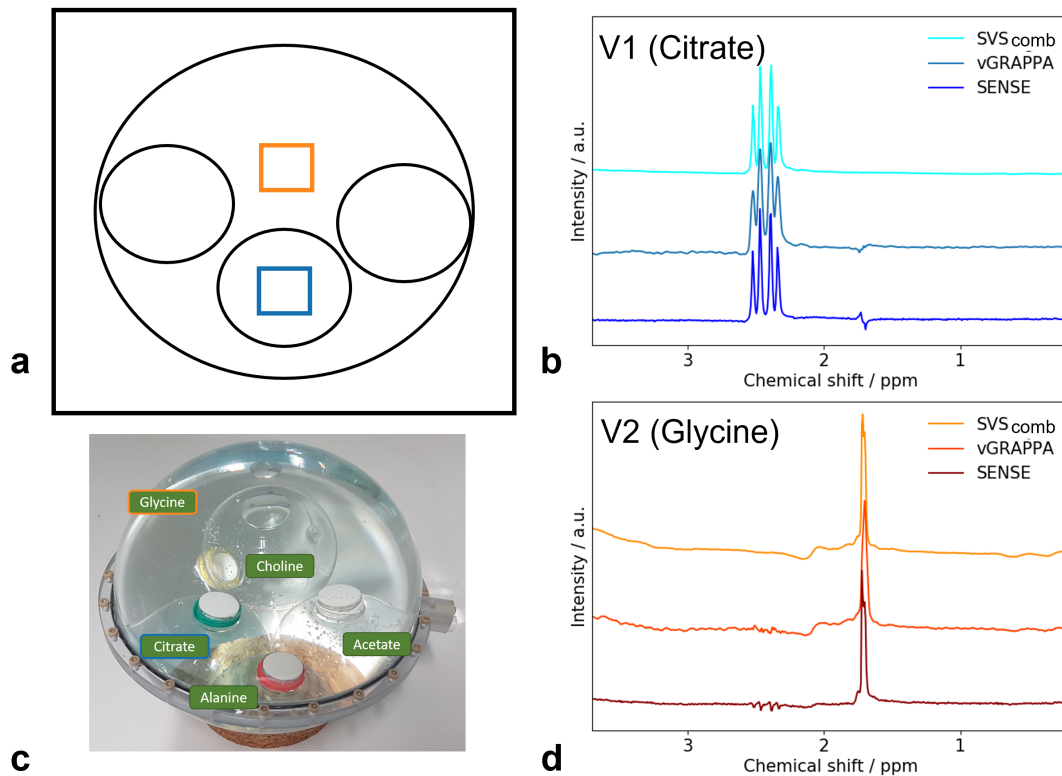


Figure 3.6: *Phantom experiments: a) Schematic and b) photo of the in-house built phantom consisting of multiple compartments: The signal from two voxels (position indicated in a)) was acquired first individually, and then simultaneously. The metabolite signal was obtained for 10 mmol glycine and 10 mmol citrate. b) and d) SVS_{comb} data (top) and sMVS signal after the decomposition with the vGRAPPA- (middle) and SENSE-based approaches (bottom) for the citrate (b; blue) and glycine (d; orange) voxel. Reprinted from [27].*

3.3.3 In Vivo Acquisition

The voxel positioning in the motor cortices of one volunteer, as well as the volumes for B_0 shimming, are depicted in Figure 3.7a. Compared to the consecutive measurement of two SVS voxels, the total scan time of sMVS acquisition was reduced by 25.6% for both of the presented decomposition algorithms, including all calibration measurements and the realistic timings (Table 3.2).

3.3.4 Influence of Shim Adjustments

There were no significant differences neither in CRLBs nor in metabolite concentrations between SVS_{ind} and SVS_{comb} , which is depicted in Figures 3.7 - 3.10. Although a slight tendency towards decreased SNR (196 ± 19 vs. 186 ± 17) and increased linewidth (12.4 ± 1.8 Hz vs. 13.0 ± 1.8 Hz) was observed, none of these differences was statistically significant. It can be seen in Figure 3.11a that the number of quantifiable metabolites remains constant for SVS_{ind} after CRLBs $> 20\%$, while a constant level for SVS_{comb} was only reached at CRLBs $> 50\%$. The \overline{CRLBs} differences between SVS_{ind} and SVS_{comb} , as depicted in Figure 3.11b, increase towards higher cutoff levels.

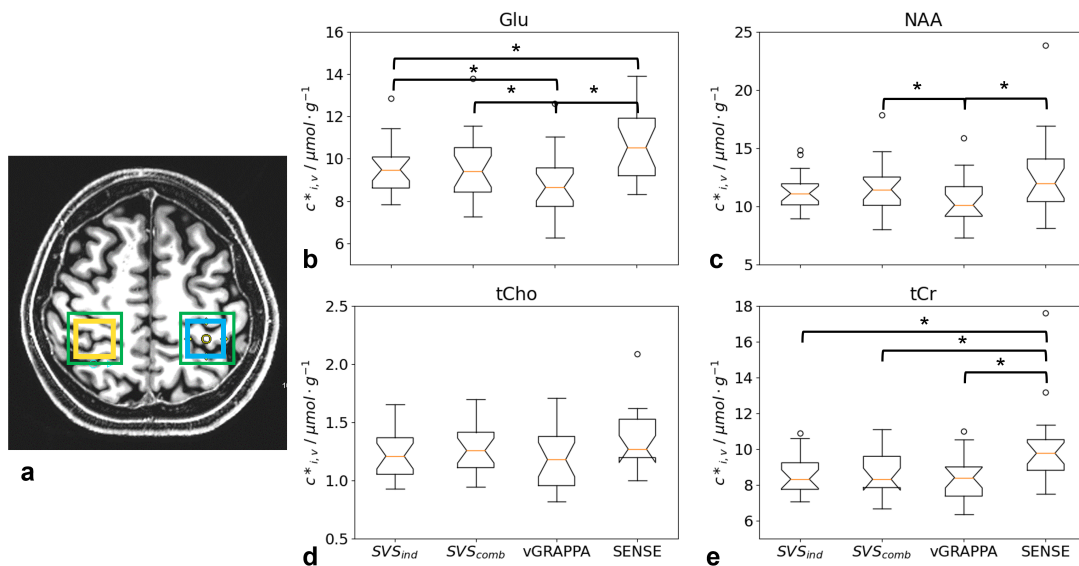


Figure 3.7: *In vivo* acquisition of the right and left motor cortex for 10 subjects: a) Example of the anatomical location of the two voxels in the right (yellow) and left (turquoise) motor cortex. Both B_0 shim volumes are indicated in green. b-e) Relaxation-corrected concentrations $c_{i,v}^*$ of b) Glu, c) NAA, d) tCho, and e) tCr obtained by SVS acquisitions using once the individually optimized settings (SVS_{ind}), once the combined-optimized settings for both voxels (SVS_{comb}), as well as measured by sMVS and decomposed once by vGRAPPA and once by the SENSE-based algorithm for the two voxels acquired in both motor cortices (left and right) of the ten subjects. The between-voxel distance was between 46 mm and 60 mm. Significant differences according to the Wilcoxon signed-rank test with a significance level of $p < 0.0038$ are marked with an asterisk. Reprinted from [27].

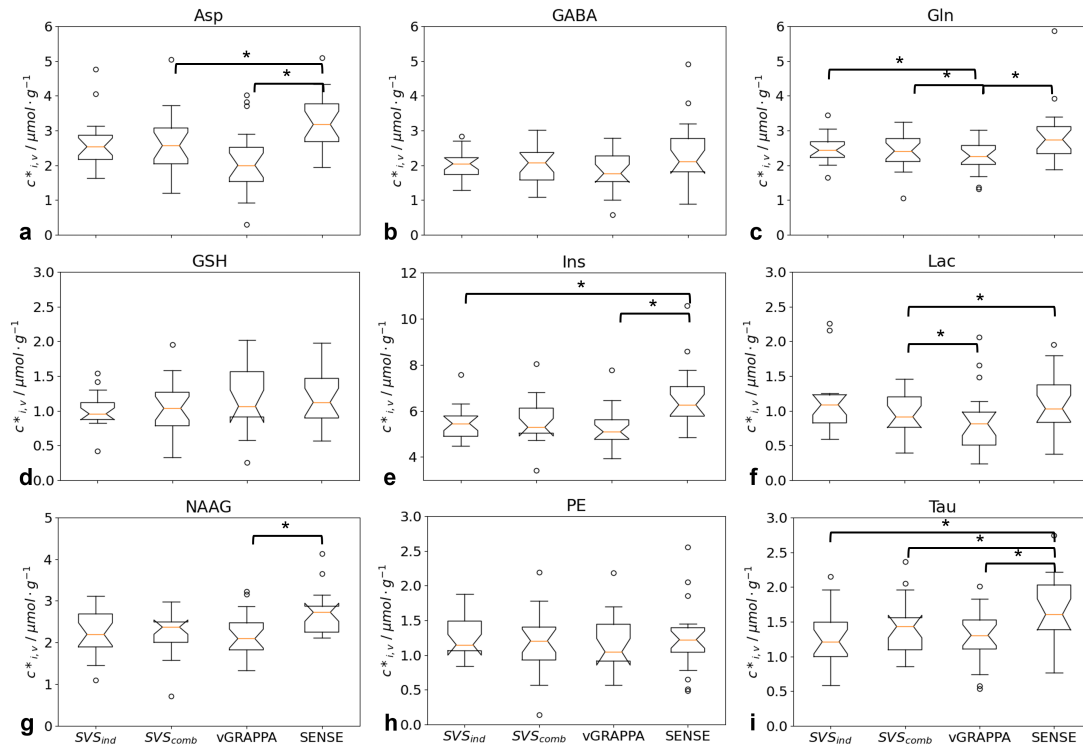


Figure 3.8: Boxplots of different metabolite concentrations obtained by different SVS and sMVS measurements: 1) SVS_{ind} , 2) SVS_{comb} , 3) vGRAPPA, and 4) SENSE-based decomposition for a) Asp, b) GABA, c) GSH, d) Gln, e) Ins, f) Lac, g) NAAG, h) PE, and i) Tau for the two voxels acquired in both motor cortices of the ten subjects. Reprinted from [27].

3.3.5 SVS_{comb} vs. sMVS

The SNR for the decomposition algorithms was 155 ± 18 and 164 ± 19 for the SENSE-based decomposition and the vGRAPPA approach, respectively. Assessment of the concentrations obtained from the SVS_{comb} and the sMVS data after decomposition resulted in a slightly higher concentration compared to SVS_{comb} for the SENSE-based decomposition, whereas the vGRAPPA decomposed spectra led to a lower one, except for PE and GSH (Figure 3.7 and Figure 3.8). Significant concentration differences between the SVS_{comb} acquisition and the decomposed sMVS datasets were observed for NAA, Gln, and Glu for vGRAPPA decomposition, as well as for Asp, tCr, and Tau for SENSE-based decomposition. Despite a trend towards higher CRLBs for both decomposition approaches compared to the SVS_{comb} acquisition, significant differences were only found for Asp for the SENSE-based decomposition (Figure 3.9 and Figure 3.10). The number of quantifiable metabolites for both decomposition algorithms is lower than for both consecutive SVS acquisitions and a constant level is only reached at CRLBs $> 50\%$ (Figure 3.11a). The performance measure for both

decomposition approaches is higher than the one for SVS_{comb} over the whole range of investigated cutoff levels (Figure 3.11b), but smaller than the difference between SVS_{ind} and SVS_{comb} (Figure 3.11b).

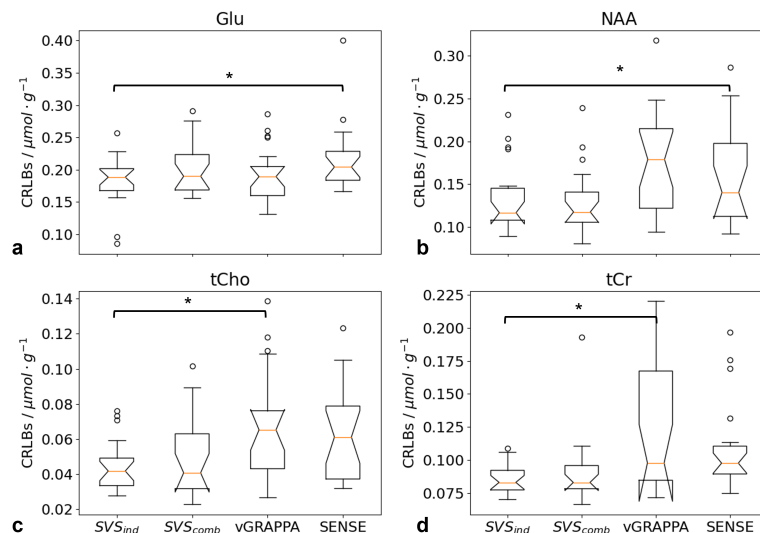


Figure 3.9: Boxplots for the CRLBs of SVS_{ind} , SVS_{comb} , as well as after the vGRAPPA- and SENSE-based decomposition approaches for the most prominent peaks: a) Glu, b) NAA, c) tCho, and d) tCr for the two voxels acquired from both motor cortices of the ten subjects. Reprinted from [27].

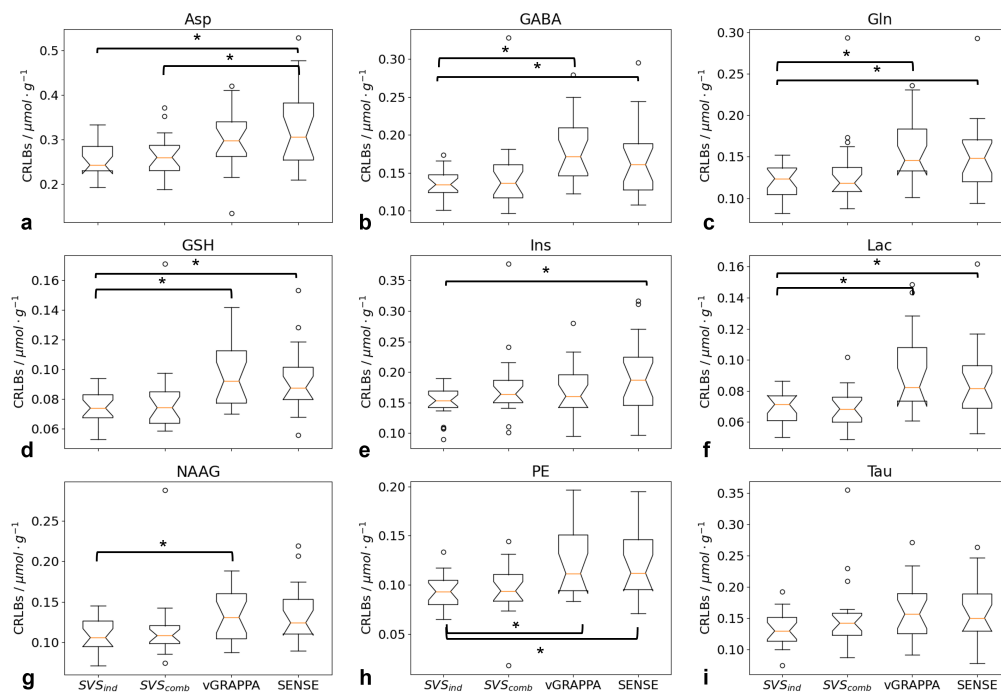


Figure 3.10: CRLBs for all measured cases: 1) SVS_{ind} , 2) SVS_{comb} , 3) vGRAPPA, and 4) SENSE-based decomposition for the lower-intensity metabolites: a) Asp, b) GABA, c) GSH, d) Gln, e) Ins, f) Lac, g) NAAG, h) PE, and i) Tau. Reprinted from [27].

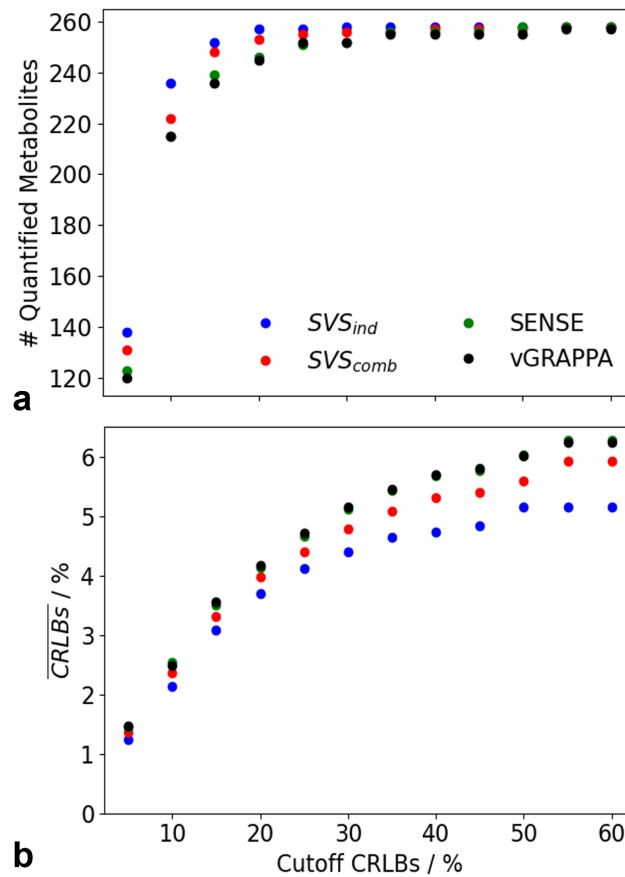


Figure 3.11: a) The number of metabolites over all 13 quantified metabolites, ten subjects, and two voxels that could be quantified, *i.e.*, were below the CRLB's cutoff. 260 (13 metabolites \times 10 subjects \times 2 voxels) is the maximum number of quantifiable data points. b) Performance measures, derived by Equation (3.2) and depending on the CRLB's cutoffs, are depicted for SVS_{ind} (blue), SVS_{comb} (red), SENSE-based decomposition (green), and vGRAPPA approach (black).

3.3.6 SVS_{ind} vs. sMVS

For the SVS_{ind} acquisition, the same trend in metabolite concentration as for the comparison between the decomposed sMVS data and SVS_{comb} was seen. Significant differences in concentration between the vGRAPPA-based approach and SVS_{ind} were observed for Glu and Gln, as well as for Ins, tCr, Tau, and Glu for the SENSE-based decomposition (Figure 3.7 and Figure 3.8). Compared to the SVS_{ind} acquisition, eight and nine out of 13 CRLBs are significantly different for vGRAPPA and the SENSE-based approach, respectively (Figure 3.9 and Figure 3.10). The difference in the number of quantifiable metabolites and $\overline{\text{CRLBs}}$ was most pronounced between SVS_{ind} and both decomposition approaches (Figure 3.11).

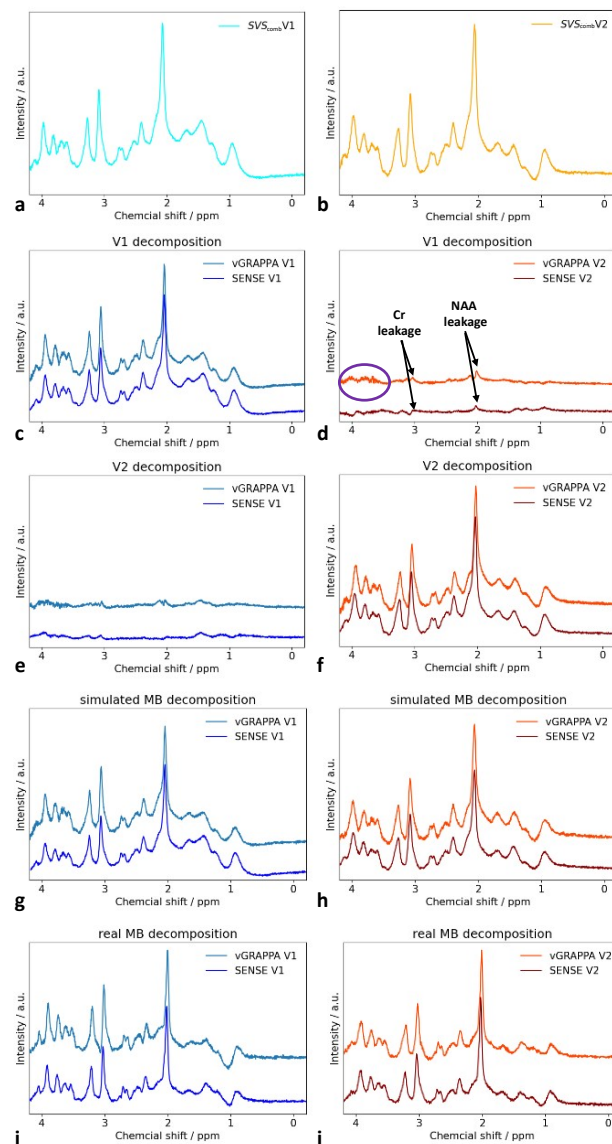


Figure 3.12: Real parts of the acquired spectra of the SVS_{comb} measurements for both voxels in the motor cortices: a) left (V1, cyan) and b) right (V2, orange). From c) to j) the decomposed spectra are depicted after applying the SENSE-based (bottom) and the vGRAPPA algorithm (top) of subject 1. c-f) Simulated decomposition for V1 and V2 based on SVS data; d) leakage of Cr and NAA is highlighted by arrows; the purple circle shows the leakage towards higher ppm values visible after applying the vGRAPPA decomposition approach. Both decomposition approaches were applied to every SVS_{comb} spectrum as if it was an sMVS acquisition to obtain the simulation. g-h) both depict the simulated sMVS acquisition, i.e., the summed SVS_{comb} acquisition of the right and left motor cortex, and i-j) show the actual decomposed MB spectra acquired with the 2SPECIAL sequence. All of the here shown spectra were normalized to the NAA peak. Reprinted from [27].

3.3.7 Comparison of Decomposition Algorithms

The spectral shapes of the vGRAPPA and SENSE-based simulated and measured sMVS in vivo acquired spectra for both voxels are shown in Figure 3.12c-j and compared with the SVS_{comb} spectra in Figure 3.12a-b. Regarding the leakage of both decomposition approaches, the signal of the respective other voxels showed small peaks, e.g., at creatine (Cr) and NAA frequencies, which slightly exceeded the noise level. Towards higher ppm values, an increased leakage was observed for the vGRAPPA decomposition. The quantitative leakage across all metabolite spectra averaged over all ten subjects was $(6.69 \pm 3.72)\%$ for SENSE and $(9.78 \pm 4.17)\%$ for vGRAPPA. Between the two algorithms, significant metabolite concentration differences were found for eight out of 13 metabolites, while no significantly different CRLBs were observed. An LCModel quantification was not possible for two (SENSE-based approach) and three (vGRAPPA decomposition) out of 260 measured concentrations (13 metabolites x 10 subjects x 2 voxels). Including all CRLBs up to 60%, both algorithms show almost similar performance measures, although the SENSE-based algorithm performs slightly better (see Figure 3.11).

Using eight instead of four transients to derive the vGRAPPA kernel decreased metabolite leakage from 5.97% to 4.90% and from 6.18% to 4.12% for the right and left motor cortex, respectively, in the subject with the lowest leakage. No substantial changes were observed for more than eight transients (see Table 3.3). Plots of leakage after vGRAPPA decomposition as a function of distance showed a weak linear trend ($R = -0.62$), suggesting that smaller between-voxel distances lead to an increased leakage (Figure 3.13). In phantom acquisitions, as depicted in Figure 3.14, the leakage levels are considerably lower and four ACS transients are already sufficient to reach saturation. Reduced leakage for larger voxel separation is confirmed for small inter-voxel distances but beyond about 20 mm no further improvement occurs.

Table 3.3: Leakage simulation for volunteer four (subject with the lowest leakage) as a function of the number of transients utilized as low SNR data for the vGRAPPA decomposition. Note that both fully sampled SVS_{comb} datasets were utilized with a reduced number of transients to generate the low SNR data. The table is reprinted from [27].

Transients	Leakage V2 to V1 / %	Leakage V1 to V2 / %
4	6.18	5.97
8	4.12	4.90
16	4.23	3.89
32	4.01	4.19

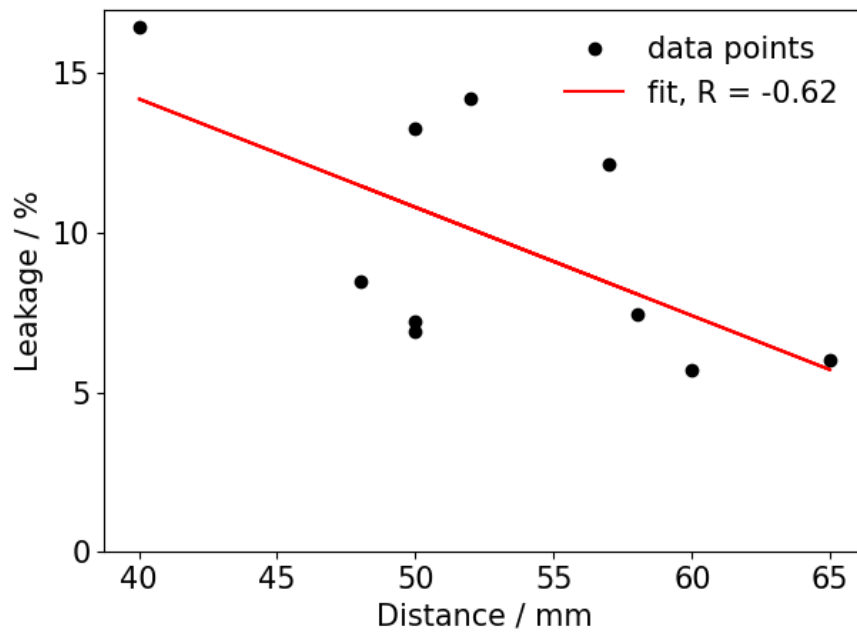


Figure 3.13: *In vivo* leakage depending on the between-voxel distance for all volunteers measured in motor cortices. The black dots represent the data, while the red line depicts the linear fit with an R -value of -0.62 . Reprinted from [27].

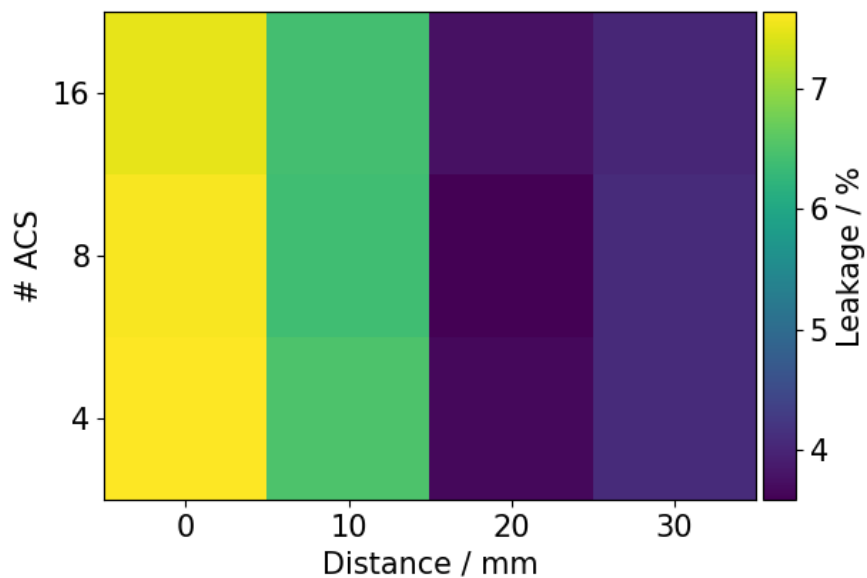


Figure 3.14: Leakage as a function of the number of ACS transients and the inter-voxel distance acquired in a homogeneous spherical SIEMENS phantom. The combined optimized settings were utilized. Reprinted from [27].

BA analyses of the spectral shapes show that the differences between SVS_{comb} and the individually decomposed sMVS data were similar in both mean difference and spread for SENSE and vGRAPPA, as shown in Figure 3.15. Nevertheless, the first voxel showed a bias in the SENSE-based decomposition, while the second one was biased in the mean of vGRAPPA.

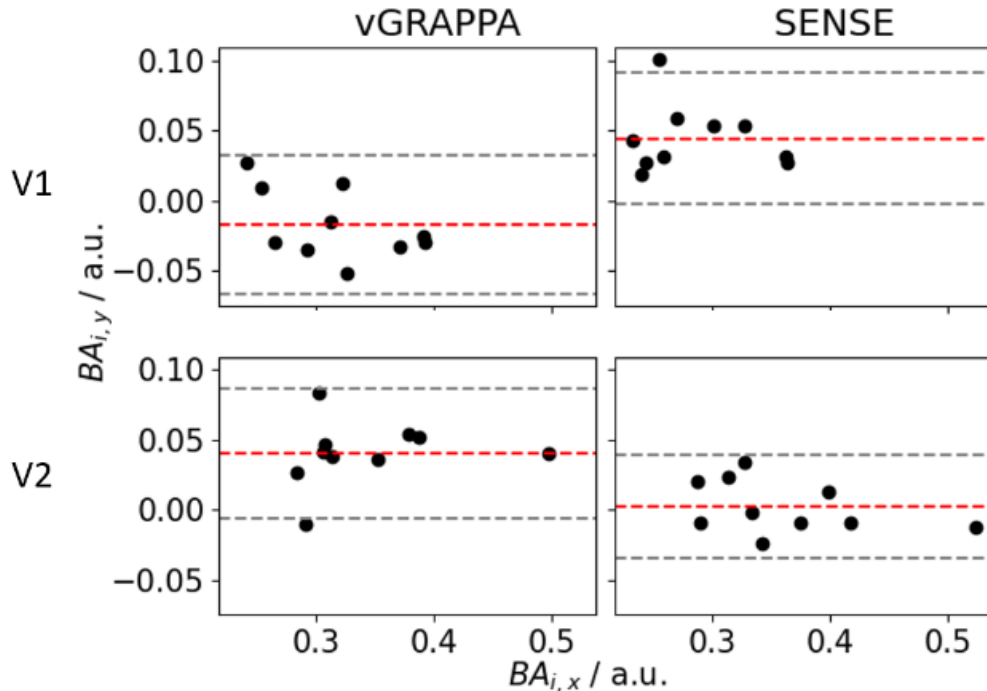


Figure 3.15: BA plots of spectral shape showing the difference between SVS_{comb} and both decomposition approaches for the left (V1) and right motor cortex (V2) in all ten volunteers. The generation of the data points in the BA plots is described in section 2.2.8. The red line refers to the arithmetic mean, whereas the two gray lines indicate $\pm (1.96 \times SD)$. Reprinted from [27].

The application of sMVS and the retrospective decomposition to the corresponding regions was also shown feasible for the non-lateral symmetric regions (Figure 3.16, Table 3.4). The effect of the combined-optimized B_1^+ and B_0 shim on the spectral shape in these two voxel regions seems to be larger for each of these regions than for the motor cortices (Figure 3.17): Using the combined-optimized adjustments (SVS_{comb}), substantially lower SNR from 170 and 123 to 145 and 113 and line broadening from 12.0 Hz and 12.5 Hz to both 16.5 Hz and could be observed compared to SVS_{ind} in the ACC/PCC and WM/GM regions, respectively.

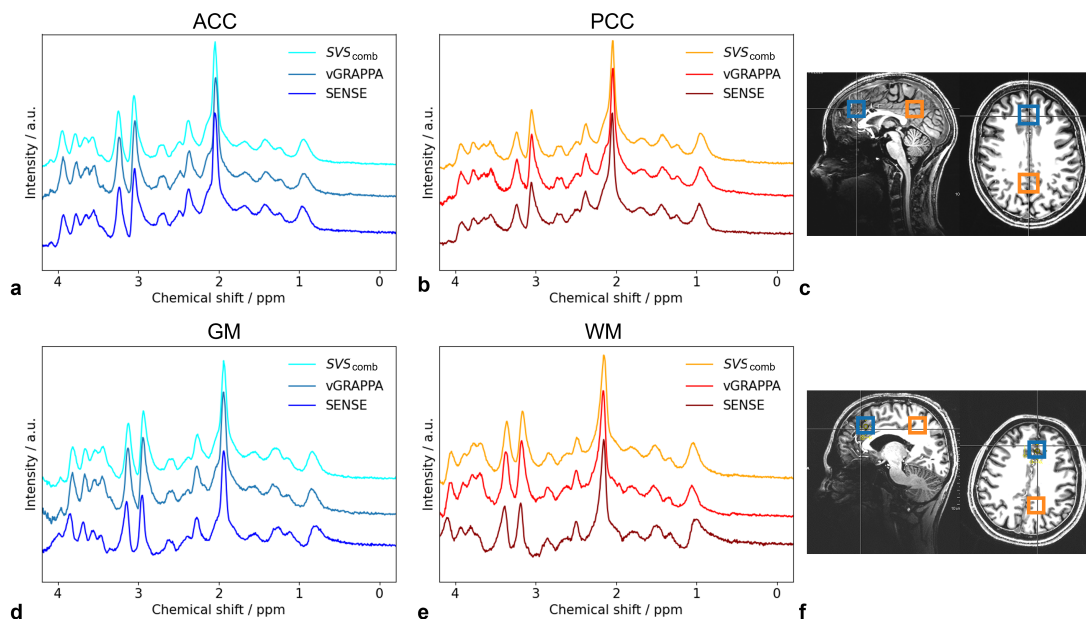


Figure 3.16: Real part of spectra for voxels acquired in the a) ACC and b) PCC of volunteer 11, and d) GM-rich ACC, and e) WM-rich voxel in the posterior left lobe of volunteer 12 for SVS_{comb} (top) and $sMVS$ decomposition using the vGRAPPA (middle) and SENSE-based approaches (bottom). c) depicts the voxel locations in the ACC/PCC at 80 mm distance, and f) shows the voxel location in the GM ACC/WM posterior at 74 mm distance. Both voxel locations are superimposed on MP2RAGE images. Reprinted from [27].

Table 3.4: Metabolite concentrations (Conc.) corrected for relaxation effects for single-subject acquisitions in the ACC and PCC for the optimized settings for one voxel (SVS_{ind}), the combined-optimized adjustments for two voxels (SVS_{comb}), and both decomposition approaches for both voxels. The table is adapted from [27].

Conc. / $\mu\text{mol g}^{-1}$	ACC				PCC			
	SVS_{ind}	SVS_{comb}	vGRAPPA	SENSE	SVS_{ind}	SVS_{comb}	vGRAPPA	SENSE
Glu	16.67	15.97	15.12	16.13	9.85	9.56	8.53	9.49
Ins	9.39	7.71	7.46	8.77	4.69	4.96	4.41	5.41
NAA	17.02	15.95	14.35	16.66	10.74	11.18	10.47	11.36
tCho	2.13	2.40	2.16	2.48	0.82	0.70	0.79	0.66
tCr	11.34	11.36	11.35	12.57	6.96	6.49	6.44	6.46
	GM				WM			
Glu	16.14	14.84	15.64	16.33	8.32	8.43	8.43	8.91
Ins	8.21	8.86	8.80	9.24	6.83	5.97	6.45	5.85
NAA	14.98	13.95	14.64	14.76	9.37	10.17	10.57	10.92
tCho	2.22	2.65	2.86	2.99	1.75	2.06	1.90	1.77
tCr	11.20	12.36	13.00	14.69	7.63	7.90	8.31	7.31

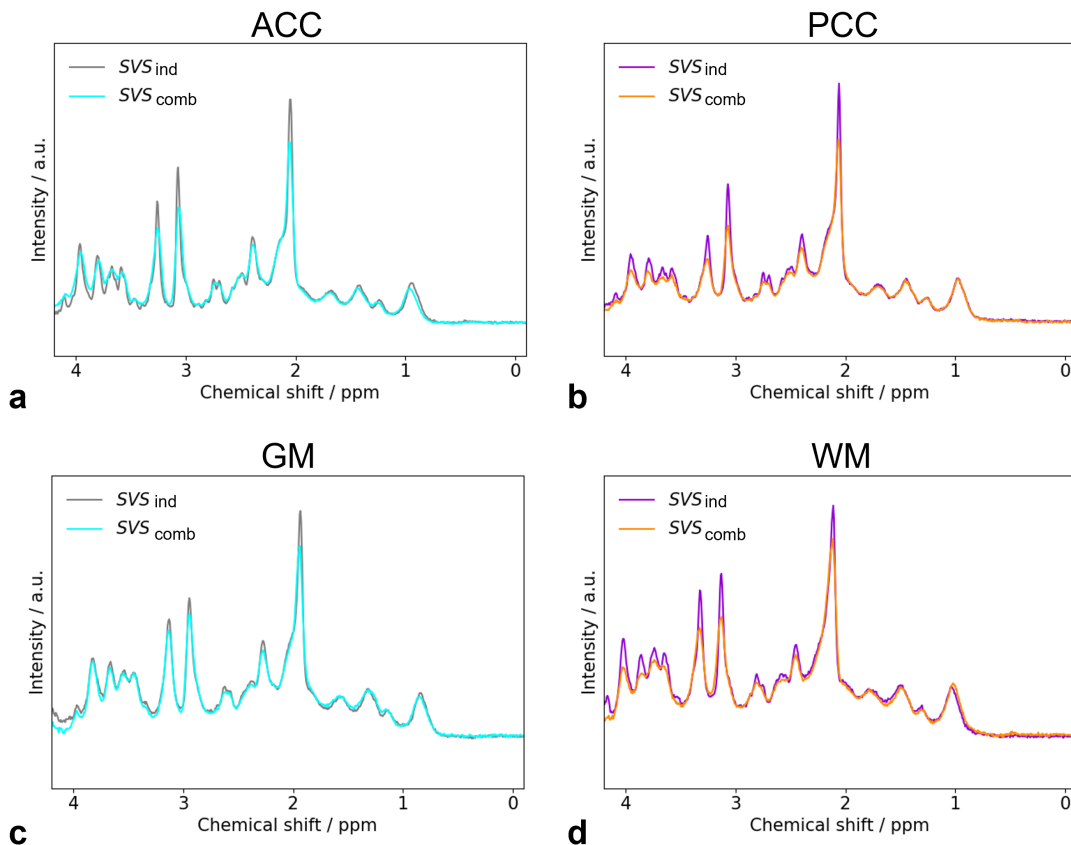


Figure 3.17: Spectral comparison between both SVS acquisitions: SVS_{ind} (gray and purple) and SVS_{comb} (cyan and orange), for the ACC (a), PCC (b) and the anterior GM of the ACC and the posterior WM region of the right lobe (GM, c; WM, d). Reprinted from [27].

3.4 Discussion

It was shown that 2SPECIAL combined with vGRAPPA allows the simultaneous acquisition of short TE spectra from two MRS voxels and the retrospective reassignment of the acquired signals to their respective origins. An MB gradient-modulated adiabatic WURST pulse was introduced to enable an accurate localization of two spatially distinct voxels by simultaneously inverting the magnetization of two spatially separated slices.

The SB WURST pulse has been successfully used in other MRS sequences [88, 89, 43]. However, it was never used as an MB pulse in either MR imaging or MRS. For SVS acquisitions, it was shown in chapter 2 that the SB WURST pulse has no significant differences in the repeatability or reproducibility of the resulting metabolite concentrations and spectral shape analysis but allows for both low peak power and small CSD [26]. This low peak power becomes even more important for MB pulses

since almost twice the nominal peak power is required in the most simple case to meet the adiabatic condition [44]. Using the WURST pulse allows simultaneous acquisition of two voxels in various regions, e.g., more distant ones or ones that require an increased B_1^+ , as the hardware limits are not easily exceeded, and thus the timing parameters can be kept similar to non-MB SVS acquisition [8].

The adiabatic inversion pulse before excitation was chosen for multi-banding since, e.g., an MB excitation pulse, as it was used in other studies [83, 79], would result in prolonged TE or other parameter changes. In any case, multi-banding the refocusing and/or excitation pulse or replacing them with another gradient-modulated pulse, such as variable-rate selective excitation (VERSE) [90, 91], within the 2SPECIAL sequence could be a viable option for future studies to obtain a further increase in the number of spatially separated voxels, from which signals can be acquired simultaneously. There are also other options to further increase the bandwidth of the gradient-modulated pulse or reduce the required peak power, such as phase scrambling or time-shifted/nonlinear phase patterns [69]. In addition, other gradient-modulated pulses, such as frequency offset corrected inversion (FOCI) or GOIA [8] could be viable options for use as MB inversion pulses. It would also be possible to utilize 2SPECIAL for oblique slices, which would require playing out the modulated gradient in two dimensions.

A common limitation of using adiabatic MB pulses is the non-linearity that occurs at high B_1^+ amplitudes due to the overlap of the two single bands (Figure 3.3), i.e., when the applied B_1^+ amplitude becomes comparable to the between-voxel distance, given that both are measured in frequency units [10]. This artifact shows a linear decrease with distance, as well as a quadratic increase with the applied amplitude. Since phase cycling is not possible with a two-banded pulse [10], the occurrence of this artifact cannot be eliminated. However, this effect can be reduced by changing the pulse parameters. Therefore, gradient-modulated pulses, such as the WURST pulse, are advantageous compared to “normal” slice-selection pulses like the HS for MB applications because they offer more degrees of freedom in setting their parameters (cf. Figure 3.4). Despite this general limitation concerning MB adiabatic pulses, the non-linearities did not hamper the acquisitions of this work, as they occur only 1) at smaller between-voxel distances than the used ones for conventional in vivo applications, and 2) at B_1^+ amplitudes that are a factor of two higher than those applied. The distances utilized here are well within the range of typical research questions of an sMVS application [92, 79, 83] and if smaller between-voxel distances at higher amplitudes are required, it could be more convenient to enlarge the voxel to cover the entire region or - if possible - to increase the bandwidth of the used RF pulse.

The decomposed sMVS spectra were compared with both SVS_{comb} and SVS_{ind} , as it allows a distinction between differences arising exclusively from the decomposition method used (SVS_{comb}) and differences which are a result of both the decomposition algorithm and trade-offs in the shim approaches for B_1^+ and B_0 (SVS_{ind}). However, the clinically relevant comparison is that with the gold standard SVS_{ind} .

The here used Wilcoxon signed-rank test (and many other statistical tests) results in p -values, quantifying differences or similarities between two different groups by determining whether the observed differences can be considered significant. However, these tests do not provide quantitative performance measures, i.e., one value describing the performance of the utilized method, which would allow a direct comparison to another method. Moreover, the interpretation of all obtained p -values can be cumbersome and might not give a visually intuitive result. To establish a quantitative performance measure - additionally to the results of the statistical tests - the $\overline{\text{CRLBs}}$ were introduced here, incorporating different cutoff levels of CRLBs and allowing a quantitative, visual value comparison between SVS_{ind} , SVS_{comb} , vGRAPPA, and the SENSE-based decomposition (cf. Figure 3.11). Note that this performance measure - even if quantitatively - does not aim to provide a full statistical analysis of the uncertainties of any kind, as it was shown in chapter 2 that CRLBs only reflect a fraction of the actual measurement uncertainty. However, this approach gives a valuable estimate of the magnitude of investigated influences on the quantification accuracy.

The newly introduced performance measure indicates that the differences between SVS_{ind} and both decomposition algorithms arise only partly from the inherent performance losses of the vGRAPPA and the SENSE-based approach. The other and even bigger contributing part originates from the differences in B_0 and B_1^+ shimming adjustments for the acquisitions in the motor cortices. These results are in line with the results of the statistical tests regarding the CRLBs (cf. Figure 3.9/3.10). Despite the differences in CRLBs, the results of the Wilcoxon signed-rank test for the concentrations (Figure 3.7/3.8) indicate that the overall quantification capability was not significantly degraded for both decomposed sMVS spectra compared to SVS_{ind} . Thus, depending on the research question, the proposed method provides a reasonable price to pay for the reduced acquisition time and actual simultaneity.

All measured concentration differences in the motor cortex region between SVS_{comb} and SVS_{ind} were less pronounced than the ones measured for each ventral/dorsal setting (cf. Figure 3.17), although this result may have limited validity because only one volunteer was measured. Given the asymmetric B_0 distribution between the posterior and frontal cortex, this result was expected, whilst the right-left symmetry of the brain is reflected in a symmetric B_0 distribution that is more easily compensated

by conventional B_0 shim hardware [93]. Additional non-spherical harmonic shim coils [94, 95] or higher degree shim coils [96, 97, 98] may be better suited to correct the distortions in B_0 of the frontal cortex that are caused by the tissue interfaces of the sinusoidal/nasal area. Therefore, the addition of more degrees of freedom to improve B_0 shimming should also reduce the differences between SVS_{comb} and SVS_{ind} in the motor cortices and thus also improve the metabolite concentration quantification of the decomposed sMVS data.

For in vivo measurements, it was expected and shown that the leakage increases with decreasing between-voxel distance (see Figure 3.13). However, this effect was less pronounced than expected as the between-volunteer differences due to differences in calibration and subject motion were larger than the correlation between leakage and distance. For a careful investigation, a single subject would have to be measured at multiple distances, which could not be realized due to time constraints in our ethical regulations. For both decomposition approaches, it was observed that the leakage of the sMVS acquisition slightly exceeds the noise level for metabolite peaks exhibiting a high intensity, such as tCr, NAA, and tCho (Figure 3.12), which was similar to previous studies [83]. The BA plots of the spectral shape (Figure 3.15) and the leakage analysis of the in vivo data suggest that the SENSE-based approach performs slightly better than vGRAPPA in this respect. This could be explained by the fact that the low SNR in vivo data of four transients, utilized for vGRAPPA, are obtained without phase cycling and therefore still have ghosting around the water signal due to inadequacies of the localization scheme, which may hinder the decomposition, especially in this frequency range [99]. Evaluations performed in this study showed that the leakage decreases with an increasing number of transients for the low SNR data (cf. Figure 3.14 and Table 3.3). At some point, however, the additional acquisition of more transients to generate the ACS signal will subvert the time saving of simultaneous acquisition. Optimizing the number of transients in combination with the kernel size used for the vGRAPPA decomposition algorithm should be pursued in future work.

The minor differences in obtained metabolite concentrations between SENSE-based and vGRAPPA decomposition (Figure 3.7/3.8) could also be due to the fact that the LCModel fitting algorithm utilizes known basis functions to estimate metabolite signal intensities, whereas water ghosting is treated as noise, which is more pronounced in the vGRAPPA decomposition data. Therefore, the metabolite concentrations in the ghosting region do not show substantial alterations with the vGRAPPA decomposition even with the noise signal present, resulting in differences in the BA plots. To ensure that both investigated decomposition approaches did not suffer from systematic errors, i.e., that the algorithms showed an improved decomposition for one voxel over

the other, the order in which both voxels were included was changed without affecting the resulting spectra. The differences in the BA plot between the two decomposition approaches might be caused by the well-known B_1^+/B_1^- asymmetry at UHF. It is likely that the distortions caused by these asymmetries are different for the sensitivity maps utilized in the SENSE-based decomposition approach and the ACS which is utilized in the vGRAPPA decomposition.

The extent of leakage observed in the phantom measurements agrees well with the literature on SENSE-based decomposition [83]. However, much less ghosting was observed than in in vivo experiments. In addition, the sensitivity maps utilized for the SENSE-based algorithm are assumed to exhibit a smooth sensitivity progression, although the phantom showed large B_1^+ and B_0 differences. Both of these circumstances might explain why the vGRAPPA decomposition performs slightly better than the SENSE-based approach for phantom experiments, but not for in vivo acquisitions. To further reduce leakage, simultaneous selective excitation [97] of both voxels in combination with alternating phases should be explored in future studies.

Up to now, only the SENSE-based approach for retrospective decomposition of signals acquired simultaneously from two voxels had been utilized. In this work, an alternative algorithm - vGRAPPA - is introduced, leading to comparable results and the same reduction in acquisition time. The decision on which of the two decomposition approaches should be used depends strongly on the protocol and application: The SENSE-based decomposition approach requires sensitivity maps - measured or computed - that are usually obtained with a larger time gap from the actual spectroscopic acquisition than the low SNR data necessary for the vGRAPPA decomposition. This could have a negative impact on the performance of the SENSE-based decomposition due to the higher probability of subject motion. Therefore, vGRAPPA could be advantageous if the volunteer is not compliant for the entire scan duration. On the other hand, the advantage of the SENSE-based algorithm is that the coil sensitivity maps are available for free if the imaging data is acquired in the same session anyway, which is often the case.

The proposed sequence in combination with the introduced decomposition technique allows not only for a significant reduction in scan time but also makes true simultaneous measurements feasible. This is particularly important when small differences between both voxels are of interest, e.g. in fMRS paradigms. It is possible to accelerate MRS without a substantial loss in quality compared to the corresponding SVS measurements. The newly introduced vGRAPPA decomposition presents a presumably less motion-sensitive alternative to the already known SENSE-based approach at otherwise very comparable performance levels.

4 Conclusion & Outlook

This work consists of two main parts. In the first one, a nested, unbalanced study design, as well as a REML statistical analysis framework is introduced. This introduced framework enables a systematic evaluation of the individual components of the measurement uncertainty and a comparison with the CRLBs that are conventionally used for this estimation. It is shown that the CRLBs reflect only a fraction of the actual measurement uncertainty but, as they correlate very well with the results from the REML analysis, their use as a measurement weight can still be justified. Moreover, the introduced study design and framework allow for the first time to determine both the repeatability and a reproducibility measure of the spectral shape and to estimate MDCs of metabolite concentrations *in vivo* for the given setup. These MDCs allow to define a threshold above which the difference between two measurements is more likely to be real and below which it is more likely to reflect measurement uncertainties. A reliable estimate of such a threshold is important, especially for longitudinal studies with repeated acquisitions. As this analysis tool is publicly available, it introduces the possibility to investigate the impact of other sequence parameters or different experimental setups, i.e., rerunning the experiments at a different time, in a different laboratory, using different equipment, or executed by different operators, on the repeatability, reproducibility, and uncertainty of an MRS measurement. It will thus allow a more profound understanding of the origin of measurement uncertainties in *in vivo* MRI and MRS and can become a valuable tool to answer important spectroscopic questions, e.g., about the respective importance of shorter TE vs. minimized CSD for improved metabolite quantification. To further increase reproducibility, automated voxel positioning should be considered.

Both the study design, as well as the statistical framework are applied to investigate whether the choice of adiabatic inversion pulse in SPECIAL has an impact on the repeatability and the reproducibility. It is shown that the gradient-modulated pulses, used as inversion pulses before the excitation, do not result in a significantly improved repeatability or reproducibility compared to the originally implemented HS pulse. Nevertheless, the gradient-modulated pulses allow for a substantially decreased peak voltage, as well as for a reduced CSD.

These advantageous properties of the gradient-modulated pulses compared to the HS pulse are also used in the second part. An MB WURST pulse is introduced to simultaneously acquire two voxels and applied for in vivo application for the first time. This allows a significant acceleration of MRS which opens the field to a wider range of applications, e.g., for fMRS questions or to obtain the signal of a lesion and its contra-lateral region for intra-subject comparison. The use of gradient-modulated pulses instead of the HS pulse also enlarges the range of applications, especially in regions, where peak voltage is a limiting factor. The introduction of the vGRAPPA decomposition for the retrospective allocation of the signal represents a new and arguably less motion-sensitive alternative to the well-established SENSE-based algorithm. Nonetheless, the application of this technique is limited by the available calibration possibilities. This can be seen in asymmetrical regions with an enlarged distance, as the combined-optimized B_0 and B_1^+ adjustments worsen the spectral quality. To improve this, further investigations on more sophisticated B_0 shim should be done, or the use of 2D arbitrary-shaped voxel excitation should be considered. The latter would also circumvent the general limitation of MB adiabatic pulses, namely the unintended partial inversion at high B_1^+ amplitudes and small between-voxel distances that were also explored in this work.

Both parts of this work tackle the introduced challenges concerning 1) the necessity of accurate uncertainty measures to enable a clear distinction between differences reflecting pathological changes and differences caused by statistical fluctuations in repeated measurements, and 2) the acceleration of MRS by actual simultaneous acquisition without substantial quality loss. The results of this work may be helpful, therefore, to establish MRS as a diagnostic method and, ultimately, integrate it into clinical routine.

Bibliography

- [1] Robin A. de Graaf. *In Vivo NMR Spectroscopy: Principles and Techniques: 2nd Edition*. 2007.
- [2] Anke Henning. Proton and multinuclear magnetic resonance spectroscopy in the human brain at ultra-high field strength: A review. *NeuroImage*, 168:181–198, 3 2018.
- [3] Christian Hundshammer, Miriam Braeuer, Christoph A. Müller, Adam E. Hansen, Mathias Schillmaier, Stephan Düwel, Benedikt Feurecker, Steffen J. Glaser, Axel Haase, Wilko Weichert, Katja Steiger, Jorge Cabello, Franz Schilling, Jan Bernd Hövener, Andreas Kjær, Stephan G. Nekolla, and Markus Schwaiger. Simultaneous characterization of tumor cellularity and the Warburg effect with PET, MRI and hyperpolarized ^{13}C -MRSI. *Theranostics*, 8(17):4765–4780, 2018.
- [4] Robert Bok, Jessie Lee, Renuka Sriram, Kayvan Keshari, Subramaniam Sukumar, Saeed Daneshmandi, David E. Korenchan, Robert R. Flavell, Daniel B. Vigneron, John Kurhanewicz, and Pankaj Seth. The role of lactate metabolism in prostate cancer progression and metastases revealed by dual-agent hyperpolarized ^{13}C MRSI. *Cancers*, 11(2), 2019.
- [5] Brian J. Soher, P. Murali Doraiswamy, and H. Cecil Charles. A review of ^1H MR spectroscopy findings in Alzheimer’s disease. *Neuroimaging Clinics of North America*, 15(4):847–852, 2005.
- [6] Anouk Marsman, René C.W. Mandl, Dennis W.J. Klomp, Marc M. Bohlken, Vincent O. Boer, Anna Andreychenko, Wiepke Cahn, René S. Kahn, Peter R. Luijten, and Hilleke E. Hulshoff Pol. GABA and glutamate in schizophrenia: A 7 T ^1H -MRS study. *NeuroImage: Clinical*, 6:398–407, 2014.
- [7] Lars G. Hanson. Is quantum mechanics necessary for understanding magnetic resonance? *Concepts in Magnetic Resonance Part A: Bridging Education and Research*, 32(5):329–340, 2008.
- [8] Alberto Tannús and Michael Garwood. Adiabatic Pulses. *NMR in Biomedicine*, 10(2):423–434, 1997.

- [9] Markus Barth, Felix Breuer, Peter J. Koopmans, David G. Norris, and Benedikt A. Poser. Simultaneous multislice (SMS) imaging techniques. *Magnetic Resonance in Medicine*, 75(1):63–81, 2016.
- [10] Gadi Goelman and John S. Leigh. Multiband Adiabatic Inversion Pulses. *Journal of Magnetic Resonance, Series A*, 101(2):136–146, 2 1993.
- [11] Vladimír Mlynárik, Giulio Gambarota, Hanne Frenkel, and Rolf Gruetter. Localized short-echo-time proton MR spectroscopy with full signal-intensity acquisition. *Magnetic Resonance in Medicine*, 56(5):965–970, 2006.
- [12] Ralf Mekte, Vladimír Mlynárik, Giulio Gambarota, Martin Hergt, Gunnar Krueger, and Rolf Gruetter. MR spectroscopy of the human brain with enhanced signal intensity at ultrashort echo times on a clinical platform at 3T and 7T. *Magnetic Resonance in Medicine*, 61(6):1279–1285, 2009.
- [13] R.J. Ordidge, A. Connelly, and J.A.B. Lohman. Image-selected in Vivo spectroscopy (ISIS). A new technique for spatially selective nmr spectroscopy. *Journal of Magnetic Resonance*, 66(2):283–294, 1986.
- [14] I. Tkáč, Z. Starčuk, I.Y. Choi, and R. Gruetter. In vivo ^1H NMR spectroscopy of rat brain at 1 ms echo time. *Magnetic Resonance in Medicine*, 41(4):649–656, 1999.
- [15] Jintong Mao, Hong Yan, and J.R. Fitzsimmons. Slice profile improvement for a clinical MRI system. *Magnetic Resonance Imaging*, 8(6):767–770, 1990.
- [16] Gülin Öz, Dinesh K. Deelchand, Jannie P. Wijnen, Vladimír Mlynárik, Lijing Xin, Ralf Mekte, Ralph Noeske, Tom W.J. Scheenen, Ivan Tkáč, Ovidiu Andronesi, Peter B. Barker, Robert Bartha, Adam Berrington, Vincent Boer, Christina Cudalbu, Uzay E. Emir, Thomas Ernst, Ariane Fillmer, Arend Heerschap, Pierre-Gilles Henry, Ralph E. Hurd, James M. Joers, Christoph Juchem, Hermien E. Kan, Dennis W.J. Klomp, Roland Kreis, Karl Landheer, Silvia Mangia, Małgorzata Marjańska, Jamie Near, Eva M. Ratai, Itamar Ronen, Johannes Slotboom, Brian J. Soher, Melissa Terpstra, Julien Valette, Marinette Van der Graaf, and Martin Wilson. Advanced single voxel ^1H magnetic resonance spectroscopy techniques in humans: Experts’ consensus recommendations. *NMR in Biomedicine*, e4236, 2020.
- [17] Karl Landheer, Rolf F. Schulte, Michael S. Treacy, Kelley M. Swanberg, and Christoph Juchem. Theoretical description of modern ^1H in Vivo magnetic resonance spectroscopic pulse sequences. *Journal of Magnetic Resonance Imaging*, 51(4):1008–1029, 2020.

- [18] Anagha Deshmane, Vikas Gulani, Mark A. Griswold, and Nicole Seiberlich. Parallel MR imaging. *Journal of Magnetic Resonance Imaging*, 36(1):55–72, 2012.
- [19] Klaas P. Pruessmann, Markus Weiger, Markus B. Scheidegger, and Peter Boesiger. SENSE: Sensitivity encoding for fast MRI. *Magnetic Resonance in Medicine*, 42(5):952–962, 1999.
- [20] Mark A. Griswold, Peter M. Jakob, Robin M. Heidemann, Mathias Nittka, Vladimir Jellus, Jianmin Wang, Berthold Kiefer, and Axel Haase. Generalized Autocalibrating Partially Parallel Acquisitions (GRAPPA). *Magnetic Resonance in Medicine*, 47(6):1202–1210, 2002.
- [21] Martin Blaimer, Felix Breuer, Matthias Mueller, Robin M. Heidemann, Mark A. Griswold, and Peter M. Jakob. Smash, sense, pils, grappa. *Top Magn Reson Imaging*, 15(4):223–236, 2004.
- [22] Kawin Setsompop, Borjan A. Gagoski, Jonathan R. Polimeni, Thomas Witzel, Van J. Wedeen, and Lawrence L. Wald. Blipped-controlled aliasing in parallel imaging for simultaneous multislice echo planar imaging with reduced g-factor penalty. *Magnetic Resonance in Medicine*, 67(5):1210–1224, 2012.
- [23] Stephen F. Cauley, Jonathan R. Polimeni, Himanshu Bhat, Lawrence L. Wald, and Kawin Setsompop. Interslice leakage artifact reduction technique for simultaneous multislice acquisitions. *Magnetic Resonance in Medicine*, 72(1):93–102, 2014.
- [24] Alan Chu and Douglas C. Noll. Coil compression in simultaneous multislice functional MRI with concentric ring slice-GRAPPA and SENSE. *Magnetic Resonance in Medicine*, 76(4):1196–1209, 2016.
- [25] Sebastian Schmitter, Gregor Adriany, Matt Waks, Steen Moeller, Maria Aristova, Alireza Vali, Edward J. Auerbach, Pierre François Van de Moortele, Kamil Ugurbil, and Susanne Schnell. Bilateral Multiband 4D Flow MRI of the Carotid Arteries at 7T. *Magnetic Resonance in Medicine*, 84(4):1947–1960, 2020.
- [26] Layla Tabea Riemann, Christoph Stefan Aigner, Stephen L.R. Ellison, Rüdiger Brühl, Ralf Mekte, Sebastian Schmitter, Oliver Speck, Georg Rose, Bernd Ittermann, and Ariane Fillmer. Assessment of measurement precision in single-voxel spectroscopy at 7 T: Toward minimal detectable changes of metabolite concentrations in the human brain in vivo. *Magnetic Resonance in Medicine*, 87(3):1119–1135, 2022.

- [27] Layla Tabea Riemann, Christoph Stefan Aigner, Ralf Mekle, Oliver Speck, Georg Rose, Bernd Ittermann, Sebastian Schmitter, and Ariane Fillmer. Fourier-based decomposition for simultaneous 2-voxel MRS acquisition with 2SPECIAL. *Magnetic Resonance in Medicine*, 88(5):1978–1993, 2022.
- [28] Kejal Kantarci, Stephen D. Weigand, Ronald C. Petersen, Bradley F. Boeve, David S. Knopman, Jeffrey Gunter, Denise Reyes, Maria Shiung, Peter C. O’Brien, Glenn E. Smith, Robert J. Ivnik, Eric G. Tangalos, and Clifford R. Jack. Longitudinal 1H MRS changes in mild cognitive impairment and Alzheimer’s disease. *Neurobiology of Aging*, 28(9):1330–1339, 2007.
- [29] Jyothika Kumar, Elizabeth B. Liddle, Carolina C. Fernandes, Lena Palaniyappan, Emma L. Hall, Siân E. Robson, Molly Simmonite, Jan Fiesal, Mohammad Z. Katshu, Ayaz Qureshi, Michael Skelton, Nikolaos G. Christodoulou, Matthew J. Brookes, Peter G. Morris, and Peter F. Liddle. Glutathione and glutamate in schizophrenia: a 7T MRS study. *Molecular Psychiatry*, 25(4):873–882, 2020.
- [30] S. Cavassila, S. Deval, C. Huegen, D. Van Ormondt, and D. Graveron-Demilly. Cramer-Rao Bound Expressions for Parametric Estimation of Overlapping Peaks: Influence of Prior Knowledge. *Journal of Magnetic Resonance*, 143(2):311–320, 2000.
- [31] S. Cavassila, S. Deval, C. Huegen, D. Van Ormondt, and D. Graveron-Demilly. Cramér-Rao bounds: An evaluation tool for quantitation. *NMR in Biomedicine*, 14(4):278–283, 2001.
- [32] International Vocabulary of Metrology Fourth edition – Committee Draft (VIM4 CD). Technical Report January, Joint Committee for Guides in Metrology, 2021.
- [33] Karl Landheer, Ralph Noeske, Michael Garwood, and Christoph Juchem. UTE-SPECIAL for 3D localization at an echo time of 4 ms on a clinical 3 T scanner. *Journal of Magnetic Resonance*, 311, 2020.
- [34] Martin Wilson, Ovidiu Andronesi, Peter B. Barker, Robert Bartha, Alberto Bizzi, Patrick J. Bolan, Kevin M. Brindle, In Young Choi, Cristina Cudalbu, Ulrike Dydak, Uzay E. Emir, Ramon G. Gonzalez, Stephan Gruber, Rolf Gruetter, Rakesh K. Gupta, Arend Heerschap, Anke Henning, Hoby P. Hetherington, Petra S. Huppi, Ralph E. Hurd, Kejal Kantarci, Risto A. Kauppinen, Dennis W.J. Klomp, Roland Kreis, Marijn J. Kruiskamp, Martin O. Leach, Alexander P. Lin, Peter R. Luijten, Małgorzata Marjańska, Andrew A. Maudsley, Dieter J. Meyerhoff, Carolyn E. Mountford, Paul G. Mullins, James B. Murdoch, Sarah J. Nelson, Ralph Noeske, Gülin Öz, Julie W. Pan, Andrew C. Peet, Harish Poptani, Stefan Posse, Eva Maria Ratai, Nouha Salibi, Tom W.J. Scheenen, Ian C.P.

- Smith, Brian J. Soher, Ivan Tkáč, Daniel B. Vigneron, and Franklyn A. Howe. Methodological consensus on clinical proton MRS of the brain: Review and recommendations. *Magnetic Resonance in Medicine*, 82(2):527–550, 2019.
- [35] Kai Zhong and Thomas Ernst. Localized in vivo human ^1H MRS at very short echo times. *Magnetic Resonance in Medicine*, 52(4):898–901, 2004.
- [36] Matt A. Bernstein, Kevin F. King, and Xiaohong Joe Zhou. *Handbook of MRI Pulse Sequences*. Elsevier, 2004.
- [37] Masoumeh Dehghani, Richard Edden, and Jamie Near. Simultaneous ultra-short TE-MRS in two voxels using a SPECIAL sequence with Hadamard encoding. *Proc Int Soc Magn Reson Med*, 2020.
- [38] Elvisha Dhamala, Ines Abdelkefi, Mavesa Nguyen, T. Jay Hennessy, H el ene Nadeau, and Jamie Near. Validation of in vivo MRS measures of metabolite concentrations in the human brain. *NMR in Biomedicine*, 32(3):1–15, 2019.
- [39] Giulio Gambarota, Ralf M ekle, Lijing Xin, Martin Hergt, Wietske Van Der Zwaag, Gunnar Krueger, and Rolf Gruetter. In vivo measurement of glycine with short echo-time ^1H MRS in human brain at 7 T. *Magnetic Resonance Materials in Physics, Biology and Medicine*, 22(1):1–4, 2009.
- [40] Hwon Heo, Sungjin Kim, Hyeong Hun Lee, Hye Rim Cho, Wen Jun Xu, Hoon Lee, Chul Kee Park, Sunghyouk Park, Seung Hong Choi, and Hyeonjin Kim. On the utility of short echo time (TE) single voxel ^1H -MRS in non-invasive detection of 2-hydroxyglutarate (2HG); challenges and potential improvement illustrated with animal models using MRUI and LCMoDel. *PLoS ONE*, 11(1):1–18, 2016.
- [41] Ralf M ekle, Simone K uhn, Harald Pfeiffer, Semiha Aydin, Florian Schubert, and Bernd Ittermann. Detection of metabolite changes in response to a varying visual stimulation paradigm using short-TE ^1H MRS at 7 T. *NMR in Biomedicine*, 30(2):1–9, 2017.
- [42] Lijing Xin, Beno t Schaller, Vladimir Mlynarik, Huanxiang Lu, and Rolf Gruetter. Proton T1 relaxation times of metabolites in human occipital white and gray matter at 7 T. *Magnetic Resonance in Medicine*, 69(4):931–936, 2013.
- [43] Ovidiu C. Andronesi, Saadallah Ramadan, Eva-Maria Ratai, Dominique Jennings, Carolyn E. Mountford, and A. Gregory Sorensen. Spectroscopic Imaging with Improved Gradient Modulated Constant Adiabaticity Pulses on High-Field Clinical Scanners. *J Magn Reson.*, 23(1):1–7, 2011.

- [44] Alberto Tannús and Michael Garwood. Improved performance of frequency-swept pulses using offset-independent adiabaticity. *Journal of Magnetic Resonance - Series A*, 120(1):133–137, 1996.
- [45] Dinesh K. Deelchand, Adam Berrington, Ralph Noeske, James M. Joers, Arvin Arani, Joseph Gillen, Michael Schär, Jon-Fredrik Nielsen, Scott Peltier, Navid Seraji-Bozorgzad, Karl Landheer, Christoph Juchem, Brian J. Soher, Douglas C. Noll, Kejal Kantarci, Eva M. Ratai, Thomas H. Mareci, Peter B. Barker, and Gülin Öz. Across-vendor standardization of semi-LASER for single-voxel MRS at 3T. *NMR in Biomedicine*, e4218, 2021.
- [46] M. Chmelík, I. Just Kukurová, S. Gruber, M. Krššák, L. Valkovič, S. Trattinig, and W. Bogner. Fully adiabatic 31P 2D-CSI with reduced chemical shift displacement error at 7 T - GOIA-1D-ISIS/2D-CSI. *Magnetic Resonance in Medicine*, 69(5):1233–1244, 2013.
- [47] Roland Kreis, Vincent Boer, In-Young Choi, Cristina Cudalbu, Robin A. Graaf, Charles Gasparovic, Arend Heerschap, Martin Krššák, Bernard Lanz, Andrew A. Maudsley, Martin Meyerspeer, Jamie Near, Gülin Öz, Stefan Posse, Johannes Slotboom, Melissa Terpstra, Ivan Tkáč, Martin Wilson, and Wolfgang Bogner. Terminology and concepts for the characterization of in vivo MR spectroscopy methods and MR spectra: Background and experts' consensus recommendations. *NMR in Biomedicine*, e4347, 2021.
- [48] Stephen M. Haley and Maria A. Fragala-Pinkham. Interpreting change scores of tests and measures used in physical therapy. *Physical Therapy*, 86(5):735–743, 2006.
- [49] Armin Rund, Christoph Stefan Aigner, Karl Kunisch, and Rudolf Stollberger. Simultaneous multislice refocusing via time optimal control. *Magnetic Resonance in Medicine*, 80(4):1416–1428, 2018.
- [50] Frank Wilcoxon. Individual comparisons of grouped data by ranking methods. *Journal of economic entomology*, 39(6):269, 1946.
- [51] José P. Marques, Tobias Kober, Gunnar Krueger, Wietske van der Zwaag, Pierre François Van de Moortele, and Rolf Gruetter. MP2RAGE, a self bias-field corrected sequence for improved segmentation and T1-mapping at high field. *NeuroImage*, 49(2):1271–1281, 2010.
- [52] Ariane Fillmer, Thomas Kirchner, Donnie Cameron, and Anke Henning. Constrained image-based B0 shimming accounting for "local minimum traps" in the

- optimization and field inhomogeneities outside the region of interest. *Magnetic Resonance in Medicine*, 73(4):1370–1380, 2015.
- [53] Sahar Nassirpour, Paul Chang, Ariane Fillmer, and Anke Henning. A comparison of optimization algorithms for localized in vivo B₀ shimming. *Magnetic Resonance in Medicine*, 79(2):1145–1156, 2018.
- [54] Maarten J. Versluis, Hermien E. Kan, Mark A. Van Buchem, and Andrew G. Webb. Improved signal to noise in proton spectroscopy of the human calf muscle at 7 T using localized B₁ calibration. *Magnetic Resonance in Medicine*, 63(1):207–211, 2010.
- [55] Mark A. Brown. Time-domain combination of MR spectroscopy data acquired using phased-array coils. *Magnetic Resonance in Medicine*, 52(5):1207–1213, 2004.
- [56] Stephen W. Provencher. Estimation of metabolite concentrations from localized in vivo proton NMR spectra. *Magnetic Resonance in Medicine*, 30(6):672–679, 1993.
- [57] B.J. Soher, P. Semanchuk, D. Todd, J. Steinberg, and K. Young. VeSPA: Integrated applications for RF pulse design, spectral simulation and MRS data analysis. *Proc Int Soc Magn Reson Med*, 2011.
- [58] Cristina Cudalbu, Kevin L. Behar, Pallab K. Bhattacharyya, Wolfgang Bogner, Tamas Borbath, Robin A. Graaf, Rolf Gruetter, Anke Henning, Christoph Juchem, Roland Kreis, Phil Lee, Hongxia Lei, Małgorzata Marjańska, Ralf Mekte, Saipavitra Murali-Manohar, Michal Považan, Veronika Rackayová, Dunja Simicic, Johannes Slotboom, Brian J. Soher, Zenon Starčuk, Jana Starčuková, Ivan Tkáč, Stephen Williams, Martin Wilson, Andrew Martin Wright, Lijing Xin, and Vladimír Mlynárik. Contribution of macromolecules to brain 1 H MR spectra: Experts’ consensus recommendations. *NMR in Biomedicine*, e4393, 2021.
- [59] K. Friston, J. Ashburner, S. Kiebel, T. Nichols, and W. Penny, editors. *Statistical Parametric Mapping*. Elsevier, 1st edition, 2007.
- [60] Yan Li. T₁ and T₂ Metabolite Relaxation Times in Normal Brain at 3T and 7T. *Journal of Molecular Imaging & Dynamics*, 2:1–5, 2013.
- [61] Michael Wyss, Thomas Kirchner, Alex Ringenbach, Klaas Prüssmann, and Anke Henning. Relaxation Parameter Mapping Adapted for 7T and Validation against Optimized Single Voxel MRS. *Proc Int Soc Magn Reson Med*, 2013.

- [62] Melissa Terpstra, Ian Cheong, Tianmeng Lyu, Dinesh K. Deelchand, Uzay E. Emir, Petr Bednařík, Lynn E. Eberly, and Gülin Öz. Test-retest reproducibility of neurochemical profiles with short-echo, single-voxel MR spectroscopy at 3T and 7T. *Magnetic Resonance in Medicine*, 76(4):1083–1091, 2016.
- [63] J. Martin Bland and Douglas G. Altman. Statistical methods for assessing agreement between two methods of clinical measurement. *The Lancet*, 327(8476):307–310, 1986.
- [64] David A. Harville. Maximum likelihood approaches to variance component estimation and to related problems. *Journal of the American Statistical Association*, 72(358):320–338, 1977.
- [65] R Core Team. R: A language and environment for statistical computing, 2020.
- [66] J. Pinheiro, D. Bates, and R Core. nlme: Linear and nonlinear mixed effects models, R package version 3.1-147.
- [67] H. Beckerman, M.E. Roebroek, G.J. Lankhorst, J.G. Becher, P.D. Bezemer, and A.L.M. Verbeek. Smallest real difference, a link between reproducibility and responsiveness. *Quality of Life Research*, 10(7):571–578, 2001.
- [68] ISO. Evaluation of measurement data — Guide to the expression of uncertainty in measurement. *International Organization for Standardization Geneva ISBN*, 50, 2008.
- [69] Christoph Stefan Aigner and Sebastian Schmitter. Designing B0 robust adiabatic multi-band inversion pulses with high time-bandwidth products and smooth slice selective gradients. *Proc Int Soc Magn Reson Med*, 2020.
- [70] M.J. Campbell and T.D.V. Swinscow. Statistics at square one. *British Medical Journal*, 1976.
- [71] Dinesh K. Deelchand, Isaac M. Adanyeguh, Uzay E. Emir, Tra My Nguyen, Romain Valabregue, Pierre Gilles Henry, Fanny Mochel, and Gülin Öz. Two-site reproducibility of cerebellar and brainstem neurochemical profiles with short-echo, single-voxel MRS at 3T. *Magnetic Resonance in Medicine*, 73(5):1718–1725, 2015.
- [72] S. Andrea Wijtenburg, Laura M. Rowland, Georg Oeltzschner, Peter B. Barker, Clifford I. Workman, and Gwenn S. Smith. Reproducibility of brain MRS in older healthy adults at 7T. *NMR in Biomedicine*, 32(2):1–8, 2019.

- [73] Jessica M. Duda, Amelia D. Moser, Chun S. Zuo, Fei Du, Xi Chen, Sarah Perlo, Christine E. Richards, Nara Nascimento, Maria Ironside, David J. Crowley, Laura M. Holsen, Madhusmita Misra, James I. Hudson, Jill M. Goldstein, and Diego A. Pizzagalli. Repeatability and reliability of GABA measurements with magnetic resonance spectroscopy in healthy young adults. *Magnetic Resonance in Medicine*, 85(5):2359–2369, 2021.
- [74] Weiqiang Dou, Oliver Speck, Thomas Benner, Jörn Kaufmann, Meng Li, Kai Zhong, and Martin Walter. Automatic voxel positioning for MRS at 7 T. *Magnetic Resonance Materials in Physics, Biology and Medicine*, 28(3):259–270, 2015.
- [75] Xue Bai, Ashley D. Harris, Tao Gong, Nicolaas A.J. Puts, Guangbin Wang, Michael Schär, Peter B. Barker, and Richard A.E. Edden. Voxel Placement Precision for GABA-Edited Magnetic Resonance Spectroscopy. *Open Journal of Radiology*, 07(01):35–44, 2017.
- [76] Jamie Near, Ashley D. Harris, Christoph Juchem, Roland Kreis, Małgorzata Marjańska, Gülin Öz, Johannes Slotboom, Martin Wilson, and Charles Gasparovic. Preprocessing, analysis and quantification in single-voxel magnetic resonance spectroscopy: experts’ consensus recommendations. *NMR in Biomedicine*, e4257, 2020.
- [77] Jack J. Miller, Lowri Cochlin, Kieran Clarke, and Damian J. Tyler. Weighted averaging in spectroscopic studies improves statistical power. *Magnetic Resonance in Medicine*, 78(6):2082–2094, 2017.
- [78] Alexander Fuchs, Mariska Luttje, Peter Boesiger, and Anke Henning. SPECIAL semi-LASER with lipid artifact compensation for 1H MRS at 7 T. *Magnetic Resonance in Medicine*, 69(3):603–612, 2013.
- [79] K. Landheer, A. Sahgal, S. Das, and S.J. Graham. Constrained source space MR spectroscopy: Multiple voxels, no gradient readout. *American Journal of Neuroradiology*, 36(8):1436–1443, 2015.
- [80] Mark E. Ladd, Peter Bachert, Martin Meyerspeer, Ewald Moser, Armin M. Nagel, David G. Norris, Sebastian Schmitter, Oliver Speck, Sina Straub, and Moritz Zaiss. Pros and cons of ultra-high-field MRI/MRS for human application. *Progress in Nuclear Magnetic Resonance Spectroscopy*, 109:1–50, 2018.
- [81] Th. Ernst and J. Hennig. Double-volume 1H spectroscopy with interleaved acquisitions using tilted gradients. *Magnetic Resonance in Medicine*, 20(1):27–35, 1991.

- [82] Jeffrey A. Stanley and Naftali Raz. Functional magnetic resonance spectroscopy: The "new" MRS for cognitive neuroscience and psychiatry research. *Frontiers in Psychiatry*, 9, 2018.
- [83] V.O. Boer, D.W.J. Klomp, J. Laterra, and P.B. Barker. Parallel reconstruction in accelerated multivoxel MR spectroscopy. *Magnetic Resonance in Medicine*, 74(3):599–606, 2015.
- [84] David J. Larkman, Joseph V. Hajnal, Amy H. Herlihy, Glyn A. Coutts, Ian R. Young, and Gösta Ehnholm. Use of multicoil arrays for separation of signal from multiple slices simultaneously excited. *Journal of Magnetic Resonance Imaging*, 13(2):313–317, 2001.
- [85] Steen Moeller, Essa Yacoub, Cheryl A. Olman, Edward Auerbach, John Strupp, Noam Harel, and Kâmil Uğurbil. Multiband multislice GE-EPI at 7 tesla, with 16-fold acceleration using partial parallel imaging with application to high spatial and temporal whole-brain fMRI. *Magnetic Resonance in Medicine*, 63(5):1144–1153, 2010.
- [86] Layla Tabea Riemann, Christoph Stefan Aigner, Rüdiger Brühl, Semiha Aydin, Ralf Mekte, Sebastian Schmitter, Bernd Ittermann, and Ariane Fillmer. Adiabatic multiband inversion for simultaneous acquisition of 1 H MR spectra from two voxels in-vivo at very short echo times. *Proc Int Soc Magn Reson Med*, 2020.
- [87] Huihui Ye, Stephen F. Cauley, Borjan Gagoski, Berkin Bilgic, Dan Ma, Yun Jiang, Yiping P. Du, Mark A. Griswold, Lawrence L. Wald, and Kawin Setsompop. Simultaneous multislice magnetic resonance fingerprinting (SMS-MRF) with direct-spiral slice-GRAPPA (ds-SG) reconstruction. *Magnetic Resonance in Medicine*, 77(5):1966–1974, 2017.
- [88] Isabell K. Steinseifer, Ralf Mekte, Rolf Gruetter, Tom Scheenen, and Arend Heerschap. Implementation of GOIA-Wurst pulse in a SPECIAL localization sequence at 7T. *Proc Int Soc Magn Reson Med*, 2011.
- [89] W. Bogner, M. Chmelik, O.C. Andronesi, S. Gruber, and S. Trattnig. In vivo 31P-MRS at 7T by single voxel E-ISIS with GOIA selection pulses. *Proc Int Soc Magn Reson Med*, 2010.
- [90] Brian A. Hargreaves, Charles H. Cunningham, Dwight G. Nishimura, and Steven M. Conolly. Variable-rate selective excitation for rapid MRI sequences. *Magnetic Resonance in Medicine*, 52(3):590–597, 2004.

-
- [91] Samy Abo Seada, Anthony N. Price, Torben Schneider, Joseph V. Hajnal, and Shaihan J. Malik. Multiband RF pulse design for realistic gradient performance. *Magnetic Resonance in Medicine*, 81(1):362–376, 2019.
- [92] Clark Lemke, Aaron Hess, Stuart Clare, Velicia Bachtiar, Charlotte Stagg, Peter Jezzard, and Uzay Emir. Two-voxel spectroscopy with dynamic B₀ shimming and flip angle adjustment at 7 T in the human motor cortex. *NMR in Biomedicine*, 28(7):852–860, 2015.
- [93] Jason P. Stockmann and Lawrence L. Wald. In vivo B₀ field shimming methods for MRI at 7 T. *NeuroImage*, 168:71–87, 2018.
- [94] Christoph Juchem, S. Umesh Rudrapatna, Terence W. Nixon, and Robin A. de Graaf. Dynamic multi-coil technique (DYNAMITE) shimming for echo-planar imaging of the human brain at 7 Tesla. *NeuroImage*, 105:462–472, 2015.
- [95] Chad T. Harris, William B. Handler, and Blaine A. Chronik. A New Approach to Shimming : The Dynamically Controlled Adaptive Current Network. *Magnetic Resonance in Medicine*, 71:859–869, 2014.
- [96] Jullie W. Pan, Kai Ming Lo, and Hoby P. Hetherington. Role of very high order and degree B₀ shimming for spectroscopic imaging of the human brain at 7 tesla. *Magnetic Resonance in Medicine*, 68(4):1007–1017, 2012.
- [97] Patrick Waxmann, Ralf Mekte, Florian Schubert, Rüdiger Brühl, Andre Kuehne, Tomasz D. Lindel, Frank Seifert, Oliver Speck, and Bernd Ittermann. A new sequence for shaped voxel spectroscopy in the human brain using 2D spatially selective excitation and parallel transmission. *NMR in Biomedicine*, 29(8):1028–1037, 2016.
- [98] Paul Chang, Sahar Nassirpour, and Anke Henning. Modeling Real Shim Fields for Very High Degree (and Order) B₀ Shimming of the Human Brain at 9.4 T. *Magnetic Resonance in Medicine*, 79:529–540, 2018.
- [99] Adam Berrington, Michal Považan, and Peter B. Barker. Estimation and removal of spurious echo artifacts in single-voxel MRS using sensitivity encoding. *Magnetic Resonance in Medicine*, 86(5):2339–2352, 2021.